

---

# Ground-State-Depletion Fluorescence Microscopy

---

**Dissertation**  
zur Erlangung des  
mathematisch-naturwissenschaftlichen  
Doktorgrades  
"Dr. rerum naturalium"  
an der Georg-August-Universität Göttingen

vorgelegt von  
Stefan Bretschneider  
aus Rotenburg/Wümme  
Göttingen 2007



GEORG-AUGUST-UNIVERSITÄT  
GÖTTINGEN

D7

Referent: Prof. Dr. S.W. Hell

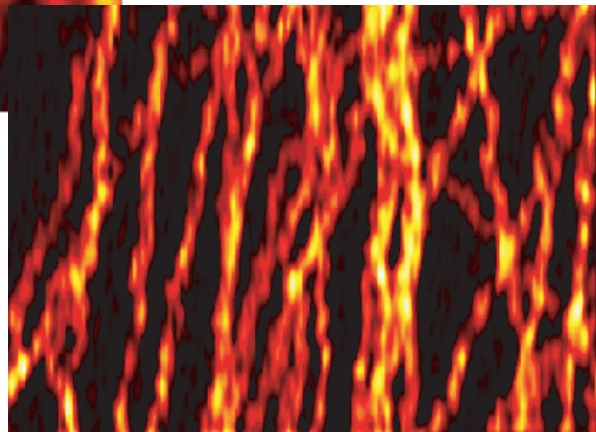
Koreferent: Prof. Dr. R.G. Ulbrich

Tag der mündlichen Prüfung:

---

# Ground-State-Depletion Fluorescence Microscopy

---



# Contents

<b>1</b>	<b>Introduction</b>	<b>5</b>
<b>2</b>	<b>Theory</b>	<b>7</b>
2.1	Fluorescence . . . . .	7
2.2	Resolution Limit of a Far-Field Light Microscope . . . . .	8
2.3	Breaking the Resolution Barrier Using the RESOLFT Concept . . . . .	12
2.4	Ground State Depletion Fluorescence Microscopy . . . . .	16
2.4.1	Engineering the Saturation Intensity . . . . .	21
2.4.2	Photobleaching in GSD Microscopy . . . . .	22
2.4.3	Engineering the Depletion PSF for GSD Microscopy . . . . .	26
<b>3</b>	<b>Experiments</b>	<b>28</b>
3.1	Experimental Realization of a GSD-Microscope . . . . .	28
3.2	Experimental Setup . . . . .	38
3.3	Generality of the Depletion Concept . . . . .	41
3.3.1	Ground State Depletion in Polymer Matrices . . . . .	41
3.3.2	Ground State Depletion in Vectashield . . . . .	43
3.3.3	Ground State Depletion in Aqueous Solution . . . . .	44
3.3.4	Ground State Depletion Using the Heavy Atom Effect . . . . .	48
3.3.5	Summarization of All Tested Dyes . . . . .	50
3.4	GSD Imaging . . . . .	52
3.4.1	GSD Imaging in PVA . . . . .	52
3.4.2	GSD Imaging in Vectashield . . . . .	58
3.4.3	GSD Imaging in Aqueous Solution . . . . .	64
3.5	Problems and Improvements . . . . .	66
<b>4</b>	<b>Summary and Outlook</b>	<b>72</b>
<b>A</b>	<b>Appendix</b>	<b>74</b>
A.1	Pump Probe Simulations . . . . .	74
A.2	Dye Spectra and Structures . . . . .	76
A.3	Sample Preparation . . . . .	79
A.4	List of Scientific Contributions . . . . .	81
	<b>Bibliography</b>	<b>82</b>

# 1 Introduction

Microscopy is one of the most important analysis tools of modern science. One defining attribute of a microscope is its resolution as it specifies the minimum distance at which one can distinguish two alike objects within an image. Therefore, if the resolution is not sufficient to resolve structures within the sample, important information will be lost and prevents the gaining of new insights. Today, the best microscopes can resolve single atoms like, for example, the transmission electron microscope (TEM) [1] or the scanning tunneling microscope (STM) [2].

In the life sciences, far-field light microscopy remained the most popular microscopy mode with fluorescence being its most important readout. The reason for this is that far field light microscopy is non-invasive, applicable to living cells, and the fluorescence labeling is specific and very sensitive.

However, one drawback of far-field light microscopy is that the resolution is limited by diffraction. The discovery of the diffraction barrier of resolution by Abbe in 1873 [3] has led to the widely accepted notion that the resolution of a far-field light microscope is limited to about half of the wavelength of light,  $\lambda/2$ . Therefore, the scanning nearfield optical microscope (SNOM) [4] was invented which images the sample through a small subwavelength aperture placed in close proximity to the sample so that the resolution is not limited by diffraction but the size of the aperture. But due to the fact that all scanning probe techniques like SNOM, STM, atomic force microscopy (AFM) [5] as well as high resolution techniques like scanning or transmission electron microscopy<sup>1</sup> are bound to the surface, their use in life sciences is limited to special applications. Also, the samples usually have to be fixed for these techniques or even have to be embedded in epoxy or frozen or imaged under vacuum conditions. Therefore it is desirable to have a far-field microscope whose resolution is much below the diffraction limit so that one can obtain high resolution non-invasive three dimensional images of living cells.

Fortunately, the fluorescence contrast mode is favorable to overcome Abbes barrier, since changing the parameters of fluorescence emission allows one to surmount the limiting role of diffraction. The first general idea to fundamentally break the diffraction barrier and promise unlimited resolution in far-field light microscopy was the RESOLFT (Reversible Saturable Optical (Fluorescence) Transitions) concept [7, 8, 9], which uses reversible saturable optical transitions to bypass the restrictions of diffraction. For example, stimulated emission depletion (STED) microscopy breaks the diffraction barrier by inhibiting fluorescence emission of the fluorescent marker [10, 11, 12]. By depleting the fluorescence, for example, with a donut shaped beam with an intensity zero in the center, the fluorescence spot can be effectively reduced in size below the diffraction limit. The

---

<sup>1</sup>Three dimensional images from biological samples are possible in electron tomography, but need extensive computational reconstruction and imaging of several subsequently prepared slices of the sample [6].

advantage of STED microscopy is that stimulated emission is possible with almost every dye molecule but there is also a disadvantage - high resolution in STED microscopy necessitates depletion intensities as high as  $GW/cm^2$ .

RESOLFT and other new sub-diffraction methods such as photoactivated localization microscopy (PALM) [13] also make use of the possibility that dye molecules [14, 15] or fluorescent proteins [16, 17, 13] can be switched between a bright and a dark state. Here, the big advantage is that one needs only very low intensities which can be in the range of  $W/cm^2$  for switching the molecules to their dark state. However, the available switchable fluorescent proteins and dyes are limited.

In this thesis the concept of ground state depletion (GSD) [18] is pursued, which aims to shelve the fluorophores in a metastable dark state (for example the triplet state), thereby effectively depleting the fluorophores ground state  $S_0$ . Since the lifetime of these dark states is usually very long compared to the fluorescence lifetime, the necessary intensities are much smaller than those for STED microscopy. Further, nearly every dye molecule has a metastable dark state and therefore GSD microscopy promises to break the diffraction barrier by combining the advantage of generality and low intensities. For this reason GSD microscopy has a good chance to become a powerful tool for biological research for new scientific insights.

## 2 Theory

### 2.1 Fluorescence

A fluorescent molecule is mainly characterized by a  $\pi$ -conjugated electron system. The absorption of a photon of appropriate energy can lift an electron from a binding  $\pi$  orbital to an antibonding  $\pi^*$  orbital. When the electron falls back to the ground state, the energy difference between the transition states can be emitted as a photon, the fluorescence light.

The photophysical processes succeeding excitation can be best described in terms of the Jablonski diagram shown in figure 2.1. It gives a simplified picture of the energy levels and the transitions among them. Usually the spins of the electrons in an organic molecule are paired in the ground state and therefore the ground state is a singlet state denoted as  $S_0$ .

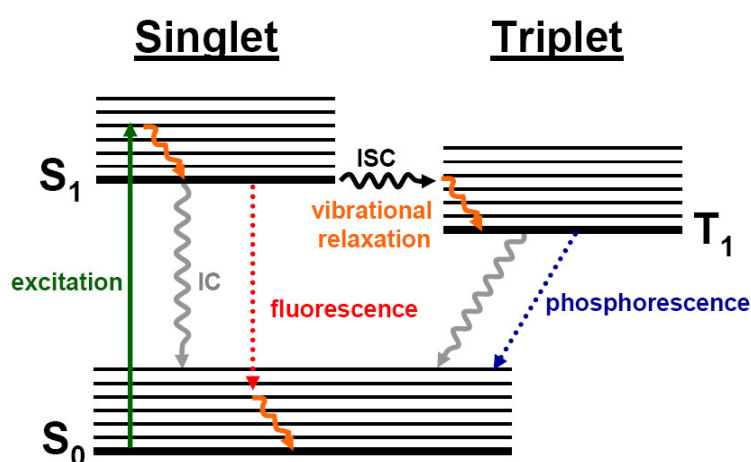


Figure 2.1: Main electronic energy levels in a fluorophore.  $S_0$  = singlet ground state,  $S_1$  = first excited singlet state,  $T_1$  = triplet state, IC = internal conversion, ISC = intersystem crossing, dotted lines = radiative transitions

The absorption of a photon with high enough energy leads to an excitation from the ground state  $S_0$  to the first excited singlet state  $S_1$ . According to the Franck-Condon principle [19], the molecules are mostly excited to higher vibrational states from which they relax fast ( $\sim 10^{-12}$ s, [20]) to the lowest vibrational state of  $S_1$ . The return to the ground state can either be radiative (fluorescence) or vibrational (denoted internal conversion). The time during which the fluorescence photons are emitted after excitation is called the fluorescence lifetime ( $\sim$ ns). After relaxation to the ground state, vibrational relaxation may occur again to the vibrational ground state of the  $S_0$ . The conversion of energy into vibrational energy during the absorption and emission process leads to a red-shift of the emitted fluorescence light compared to the exciting light, the so called Stokes-shift. This Stokes-shift can be exploited to spectrally separate the excitation light from the emitted

fluorescence light which is applied in fluorescence imaging.

Another important property of a fluorophore shown in the Jablonski diagram in figure 2.1 is the existence of two basic electronic states of the molecule, the singlet and the triplet state. In the singlet state (= usually the ground state) the spins of the electrons are paired so that the total angular spin momentum is zero. In the triplet state the spin of one electron is flipped resulting in two unpaired electron spins and a total angular spin momentum of one. Optical transitions between singlet and triplet states require a spin flip and hence are optically suppressed [21]. Nevertheless, populating the triplet state  $T_1$  is possible by exciting the dye to the first excited singlet state  $S_1$ . This is because on every excitation event from the singlet ground state  $S_0$  to the  $S_1$ , there is a finite probability of a nonradiative intersystem crossing  $S_1 \rightarrow T_1$ .

Since the transition back from the triplet  $T_1$  to the singlet state  $S_0$  is also spin-forbidden, it is usually very slow ( $\sim \mu s$  to  $ms$  [22]) compared to the fluorescence lifetime ( $\sim ns$ ). Also, the relaxation from the triplet to the singlet state is mostly non-radiative (vibrationally), because the rate for radiative transitions  $T_1 \rightarrow S_0$  (phosphorescence) is very small compared to the rate for radiationless transitions. In general phosphorescence occurs only at very low temperatures where the rate for radiationless deactivation of the triplet state gets into the range of the phosphorescence rate so that they can compete.

Anyway, the spin conservation rule has to be softened for the intersystem crossing process which is due to spin-orbit-coupling. In that way the perturbing effect of the spin-orbit coupling leads to the situation that the total angular momentum  $J$  has to be conserved now instead of the total spin angular momentum ( $J = L + S$ , with  $J$  denoting the total angular momentum which is the sum of the total orbital angular momentum  $L$  and the total spin angular momentum  $S$ ). For weak spin-orbit-coupling, a simple model can be used in that one assumes that due to the spin-orbit-coupling, the singlet wave function has a small admixture of a triplet wavefunction and the triplet wavefunction has a small admixture of a singlet wavefunction [23]. In that case, the transitions between the triplet and singlet states are arranged from these small admixtures of the extra wavefunctions resulting in a possible but unlikely transition between the singlet and the triplet.

Since the spin-orbit coupling arises from the coupling of the electron spin with the magnetic field generated by the relative motion of the nuclear charge, it is plausible that the spin-orbit coupling increases for heavier atoms (having a higher charge and thereby generating a stronger magnetic field). This effect is known as the heavy-atom effect which increases the probability of intersystem crossing. Doping a dye molecule with heavy atoms therefore enhances the intersystem crossing rate [24].

## 2.2 Resolution Limit of a Far-Field Light Microscope

Being noninvasive, far-field light microscopy has developed to a very popular microscopy mode in the life sciences. However, in far-field light microscopy, the resolution is limited by diffraction. The resolution defines the minimal distance at which two alike objects

can be discerned. Having recognized this, Ernst Abbe published the first detailed analysis of the resolution ability of a far field light microscope [3]. He stated that the lateral diffraction-limited resolution  $\Delta r$  of an optical far field microscope is given by the following formula:

$$\Delta r = 0.61 \frac{\lambda}{n \sin \alpha} = 0.61 \frac{\lambda}{NA} \quad (2.1)$$

$\lambda$  is the wavelength of the light used in the image formation process,  $n$  the refractive index,  $\alpha$  the semi-aperture angle and  $NA$  the numerical aperture of the objective lens. More precisely, the resolution is determined by the point spread function (PSF) which is the spatial intensity distribution of a point-like source imaged by an optical system. The resulting image  $I(x,y)$  in a far field fluorescence microscope is the convolution of the dye distribution of the imaged objects  $O(x,y)$  with the spatial intensity distribution  $h(x,y)$  of the PSF:

$$I(x,y) = h(x,y) \otimes O(x,y) \quad (2.2)$$

Following the convolution theory, an image identical to the object can only be obtained for a PSF being a delta function. The PSFs of a light microscope can be described by first order Bessel functions and their extension can be measured by the distance between the first two minima (due to its radial symmetry in the focal plane this is also called the Airy disc). For the lateral and axial direction, the distance between the first two minima is given by [25]:

$$\Delta r = 1.22 \frac{\lambda}{NA} \quad (2.3)$$

$$\Delta z = 4.00 \frac{n\lambda}{NA^2} \quad (2.4)$$

Usually the PSFs can be well approximated by a Gaussian function and therefore the full width half maximum (FWHM) can serve as the resolution criterion. In that case, a reasonable definition of the resolution would be that two adjacent objects can still be separated in the microscope image if the FWHM of the imaging PSF is smaller than the distance between the two objects. To illustrate the importance of the extent of the PSF, figure 2.2 shows the image formation process for two PSFs of different FWHM (one with FWHM of 200nm and one with FWHM of 50nm) for objects with an extent of 40nm. The FWHM of 200nm for the PSF was chosen because this is the resolution one can typically achieve with visible light in a diffraction-limited far-field light microscope. The other PSF with a FWHM of 50nm illustrates the potential of a subdiffraction imaging system. Due to equation (2.2), the 40nm sized randomly distributed beads (the imaged objects) have to be convolved with the PSFs to receive the particular images. Having a FWHM of 50nm, the small PSF manages to resolve all the single beads. In contrast, the 200nm PSF fails to distinguish all single beads. The result for the larger PSF is that one loses information of the imaged object which cannot be reconstructed.

In a far-field microscope, the light is propagating through the focus and thereby also signal is generated not originating from the focal plane leading to constant background signal (in fluorescence microscopy this means for example that molecules out of the focal plane are excited and their fluorescence is detected). For that reason, a confocal microscope can be used to suppress this signal [26]. This is achieved by inserting a pinhole into the

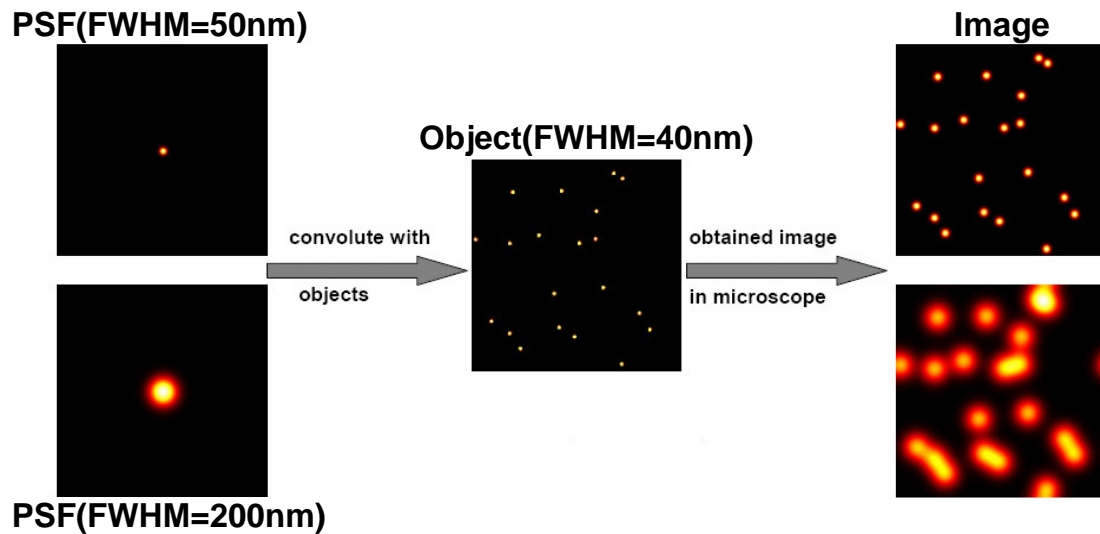


Figure 2.2: Illustrated imaging process in an optical microscope. To obtain the image, the PSF has to be convolved with the objects. If the imaging PSF is too large, adjacent objects cannot be resolved anymore.

imaging plane of the microscope for suppressing the signal not formed in the focal plane. This reduction of out of the focal plane signal enables a confocal microscope to image 3D objects which is of great interest for biological imaging. A basic confocal setup is shown in figure 2.3. One disadvantage of the confocal microscope is that the sample

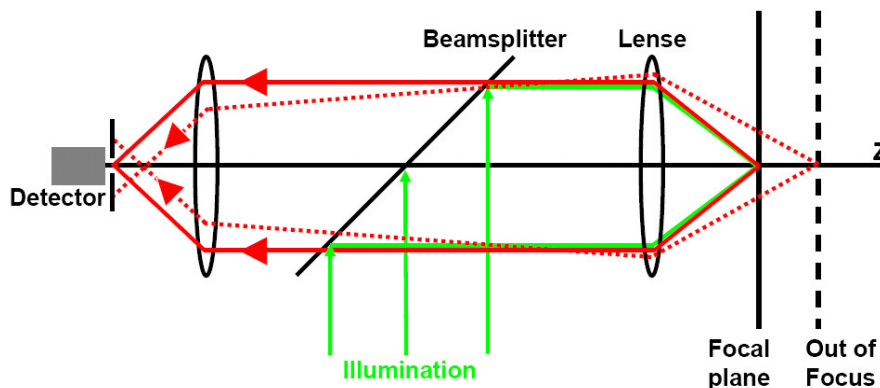


Figure 2.3: Working principle of a confocal microscope. Light not emerging from the focal plane (dotted red line) is blocked by the pinhole in front of the detector.

has to be scanned through the focus which slows down the imaging speed. But with the invention of the Confocal Laser Scanning Microscope (CLSM) [27], in which the focal spot is scanned through the sample instead of the sample itself, the acquisition times could be significantly decreased for  $\mu\text{m}^2$  areas.

Another approach for 3D optical imaging in fluorescence microscopy exploits the non-linearity of multi photon absorption [28, 29]. In such a multi photon microscope, the fluorophores are excited with photons having only a fraction of the necessary energy for excitation. Hence multiple photons have to be simultaneously absorbed to excite the molecule and therefore the required photon density has to be very high to excite the

molecules. Hence the absorption process is highly nonlinear and therefore the excitation of the fluorophores mainly takes place in the center of the focus, making the use of a pinhole like in a confocal microscope unnecessary. Also, the extent of the PSF is reduced in a multiphoton microscope but this effect is cancelled out by the larger wavelengths one has to use for the excitation.

During the last years, several methods for improving the resolution of a light microscope came up. One of them, the 4Pi-microscope [30] enhances the resolution in the axial direction, which is usually in the range of 500nm to 800nm compared to the lateral resolution of about 200nm. This is achieved by using two opposing lenses for excitation and/or detection whereby the improvement of the numerical aperture reduces the axial resolution down to 80nm [31]. Of course this method is still limited by diffraction and cannot reach arbitrarily small resolutions - it only puts diffraction to its utmost limit.

Reducing the wavelength according to equation (2.1) would also scale down the size of the PSF. However, wavelengths below 350nm are often phototoxic to living cells and are therefore not useful in biological imaging [32]. Another problem arising from the use of smaller wavelength is that commonly used optics from visible light microscopy cannot be used anymore (common optics absorb light below  $\sim 350$ nm). Further increasing of the numerical aperture is presently limited to the largest technical achievable semi-aperture angle of about  $70^\circ$ .

As mentioned before, another approach to enhance the resolution, the scanning near field optical microscope (SNOM), uses a small sub-diffraction aperture or small tip to illuminate the object. By scanning this small aperture or tip over the sample, the subdiffraction image is recorded. Although this technique has been advanced in the last years (driving the resolution to  $< 10$ nm, [33]), this method is still limited to surfaces, making it impracticable for most biological applications.

The first idea able to fundamentally break the diffraction barrier and promising real unlimited resolution in far-field light microscopy was the RESOLFT concept, which uses reversible saturable optical transitions to bypass the restrictions put by diffraction [7, 8, 34, 9]. RESOLFT and other new sub-diffraction methods make use of the possibility that dye molecules [10, 11, 14, 15] or fluorescent proteins [16, 17, 13] can be switched between a bright and a dark state.

## 2.3 Breaking the Resolution Barrier Using the RESOLFT Concept

As already mentioned in the last section, one way to overcome the diffraction limit is to use reversible saturable optical (fluorescence) transitions (RESOLFT). This concept was introduced by Hell et al. and is described, for example, in [8]. The aim of this method is to bring the molecules everywhere except at a small subdiffraction spot into a non-fluorescent or non-detectable state. Thereby the volume where the fluorescence is emitted is sized down below the diffraction limit. Scanning this subdiffraction fluorescence spot or spots (in a parallelized setup) over the sample results in a subdiffraction image.

RESOLFT relies on two states of a dye molecule, a bright one A emitting fluorescence and a dark one B which is non-fluorescent<sup>1</sup> (figure 2.4a). The molecules can be driven by light from the bright state A to the dark state B with the rate  $k_{AB} = \sigma_{AB} \frac{\lambda}{hc} I = \sigma_{AB} \gamma I$  (with  $\sigma_{AB}$  denoting the absorption cross section,  $\lambda$  the used wavelength,  $h$  Planck's constant,  $c$  speed of light,  $I$  the intensity and  $\gamma = \frac{\lambda}{hc}$ ). The transition from the bright state to the dark state has to be reversible so that the molecules can return to the bright state A with the rate  $k_{BA}$ , for example thermally on their own or also driven by light of a different wavelength. This simple two state model can be described by the following rate equations for the population numbers  $n_A$  and  $n_B$  for the states A and B.

$$\dot{n}_A(t) = -\dot{n}_B(t) = k_{BA}n_B - k_{AB}n_A = k_{BA}n_B - \sigma_{AB}\gamma I n_A \quad (2.5)$$

Assuming that all molecules are in state A at the beginning and considering continuous-wave (cw)-laser illumination leads to an equilibrium of the populations of the two states after a time period  $t \gg (k_{AB} + k_{BA})^{-1}$ . The population of the two states now only depends on the rates  $k_{AB}$  and  $k_{BA}$  and thereby on the applied intensity  $I$ .

$$n_A^\infty = \frac{k_{BA}}{k_{AB} + k_{BA}} = \frac{k_{BA}}{\sigma_{AB}\gamma I + k_{BA}} \quad (2.6)$$

$$n_B^\infty = \frac{k_{AB}}{k_{AB} + k_{BA}} = \frac{\sigma_{AB}\gamma I}{\sigma_{AB}\gamma I + k_{BA}} \quad (2.7)$$

At the saturation intensity  $I_{sat} = k_{BA}/(\sigma_{AB}\gamma)$ , half the molecules have been shifted to the state B. Further increasing the intensity  $I \gg I_{sat}$ , which means  $k_{AB} \gg k_{BA}$ , drives nearly all molecules to the state B:  $n_A^\infty \rightarrow 0$ . This behaviour is shown in figure 2.4b where the normalized population numbers are plotted against the applied intensity  $I/I_{sat}$ . At the saturation intensity  $I_{sat}$ , half the molecules have been driven to the dark state B. Further increasing the intensity leads to a strong population of the state B and depopulation of the state A until all molecules are in the dark state B.

How one can exploit this to enhance the resolution beyond the diffraction barrier is illustrated in figure 2.4c. It shows the spatial distribution of dye molecules along the  $x$ -direction in the state A under illumination of a standing wave with a local zero at  $x_i$ . The

<sup>1</sup>in principle RESOLFT is not limited to fluorescence, A and B can also be absorbing and non-absorbing, or any other optical distinguishable two states of the molecule

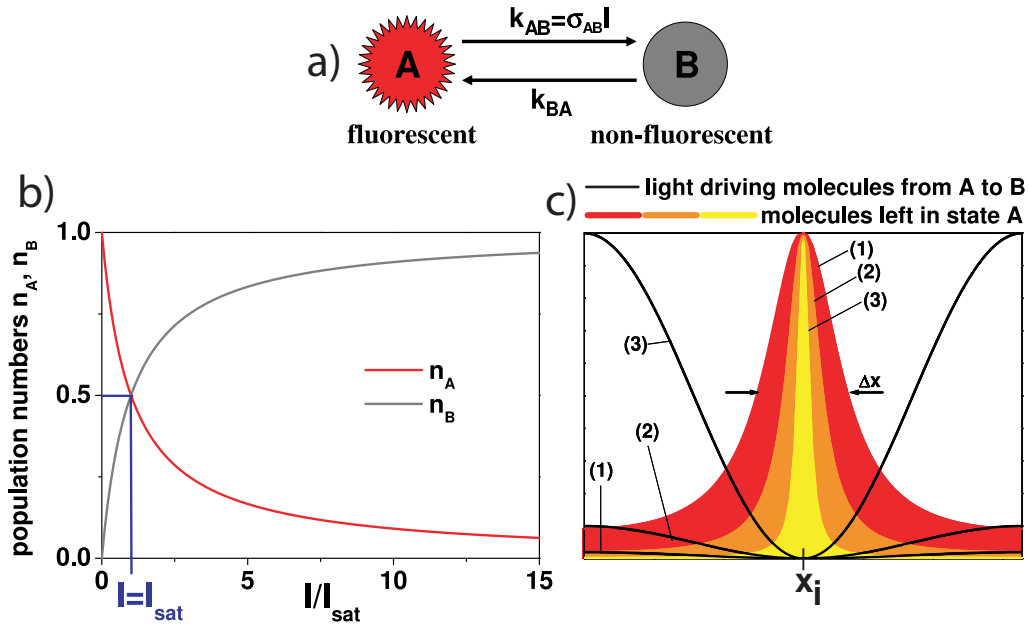


Figure 2.4: a) Principle of RESOLFT: a fluorophore can be reversibly driven from the fluorescent state A to the non-fluorescent state B. b) Population numbers  $n_A$  and  $n_B$  of A and B for different depletion intensities  $I/I_{sat}$ . At  $I_{sat}$  half the molecules have been driven into the state B. c) Following illumination with a standing wave with local zero at  $x_i$ : spatial distribution of fluorophores remaining in the bright state A for different peak depletion intensities: 1)  $I_{max} = 10I_{sat}$ , 2)  $I_{max} = 50I_{sat}$  and 3)  $I_{max} = 500I_{sat}$ . The black curves are the depletion intensity distributions with the local intensity zero at  $x_i$ .

light shifts the molecules from the bright state A to the dark state B everywhere except at the intensity zero  $x_i$ . In figure 2.4c the areas with remaining molecules in the bright state A are plotted for different peak depletion intensities up to  $I_{max}/I_{sat} = 500$ . It is demonstrated that for increasing  $I_{max}/I_{sat}$ , the fluorescent area becomes smaller and smaller and the size of the fluorescent spot can, in principle, be shrunk down to the scale of one dye molecule. This means that the size of the spot where the fluorescence is emitted is not limited anymore by the diffraction but is confined to subdiffraction extent by the applied intensities. The spatial distribution of the dye molecules in the bright state A can be calculated for an arbitrary intensity distribution  $I(r)$  of the depletion light from equation (2.6)

$$n_A^\infty(r) = \frac{k_{BA}}{k_{AB} + k_{BA}} = \frac{k_{BA}}{\sigma_{AB}\gamma I(r) + k_{BA}} \quad (2.8)$$

It can be seen from figure 2.4 that the resolution in RESOLFT microscopy scales with the applied maximum depletion intensity  $I_{max}$ . To calculate the resolution of a RESOLFT microscope, the Abbe resolution equation (2.1) can be extended by a simple factor depending on the depletion intensity  $I_{max}$  [9].

$$\Delta x = 0.61 \frac{\lambda}{n \sin(\alpha)} \cdot \frac{1}{\sqrt{1 + I_{max}/I_{sat}}} \quad (2.9)$$

where  $\Delta x$  is the FWHM of the confined fluorescence spot,  $n$  the refractive index,  $\alpha$  the half aperture angle,  $I_{max}$  is the maximum of the applied depletion intensity and  $I_{sat}$  the intensity

at which the fluorescence is reduced by 50 percent, meaning that half the molecules are in the dark state B.

To summarize, for RESOLFT applied in fluorescence microscopy, one needs the following conditions:

- a dye molecule with at least one bright state A and a dark (or non-detectable) state B whose transitions are reversible
- one of the transitions from A to B or B to A is required to be light driven
- the light driven transition has to be saturable so that after increasing the depletion intensity over a certain threshold, the state populations stay constant

The first realization of RESOLFT was the STED microscope [10, 11] which utilizes stimulated emission depletion (STED) to deactivate the fluorescence from the first excited singlet state  $S_1$ . In this case the ground state  $S_0$  of the dye molecule would be the dark state B and the bright state would be the first excited singlet state  $S_1$ . After excitation, the molecules are deexcited by stimulated emission everywhere but at the local intensity minimum of the depletion focus of the STED light. Following the RESOLFT principle, the fluorescence emission spot is sized down to a small region of the intensity zero and is no longer dependent on the diffraction-limited excitation focus. Up to now STED has achieved macromolecular resolution of 15-20nm [35] and an axial resolution of 33nm [36]. Furthermore STED microscopy as the first realized RESOLFT concept has already proved its applicability in biological and physical applications [37, 38, 39, 40].

The advantage of STED microscopy is that stimulated emission is realizable with every dye molecule but it also has a disadvantage. For the deexcitation of the dye molecules by stimulated emission, one needs very high intensities in the range of  $GW/cm^2$ . This stems from the short fluorescence lifetime ( $\sim ns$ ) which results in a fast fluorescence rate  $k_{fl} \sim 10^9/s$  (the rates can be calculated by the inverse of the lifetimes). In order to reach a strong depletion, the rate for STED  $k_{STED}$  has to be much larger than the rate for fluorescence. For example, for  $k_{STED} \approx 100k_{fl} = 10^{11}/s$ , depletion intensities of  $GW/cm^2$  are necessary ( $k_{STED} = \sigma\gamma I$  with  $\sigma \approx 10^{-16}cm^2$ ,  $\gamma \approx 10^{18}/(Ws)$ ).

Another realization of RESOLFT uses switchable proteins [16] or dyes [41] which can be turned forth and back between a fluorescent and non-fluorescent state with two different wavelengths. Here, the big advantage is that one needs only very low intensities which can be in the range of  $W/cm^2$  for switching the molecules to their dark state. Nevertheless, the available switchable fluorescent proteins and dyes are limited.

Yet another concept which promises both a general effect for deexcitation and smaller intensities compared to STED is the ground state depletion (GSD) concept [18]. Here the molecules are pumped into the dark and metastable triplet state (or any other dark state) for deexcitation of the fluorescence. Since every dye molecule usually has a triplet state (or other dark state), GSD is a general concept like STED. Also the lifetime of the triplet state (or another dark states) is longer than the fluorescence lifetime (usually the triplet lifetime is in the range of  $\mu s$  to  $ms$ ) so that the depletion intensities are smaller than those for STED. Therefore GSD could combine the advantages of generality and small

depletion intensities.

## 2.4 Ground State Depletion Fluorescence Microscopy

Ground state depletion (GSD) is based on the shelving into a long-lived (compared to the lifetime of  $S_1$ ) dark state<sup>1</sup> (for example the triplet state).

Figure 2.5 shows the energy states of a typical fluorophore. The fluorophores are excited from the electronic ground state  $S_0$  to the first excited electronic singlet state  $S_1$  with an excitation rate  $k_{exc} = \sigma\gamma I \sim I$  (with  $\sigma$  denoting the absorption cross section,  $I$  the intensity,  $\gamma = \frac{\lambda}{hc}$ ,  $\lambda$  the used wavelength,  $h$  Planck's constant and  $c$  speed of light). The most probable relaxation from the  $S_1$  state is the return to the ground state  $S_0$  by internal conversion or spontaneous emission of a photon which occurs in the range of several nanoseconds.

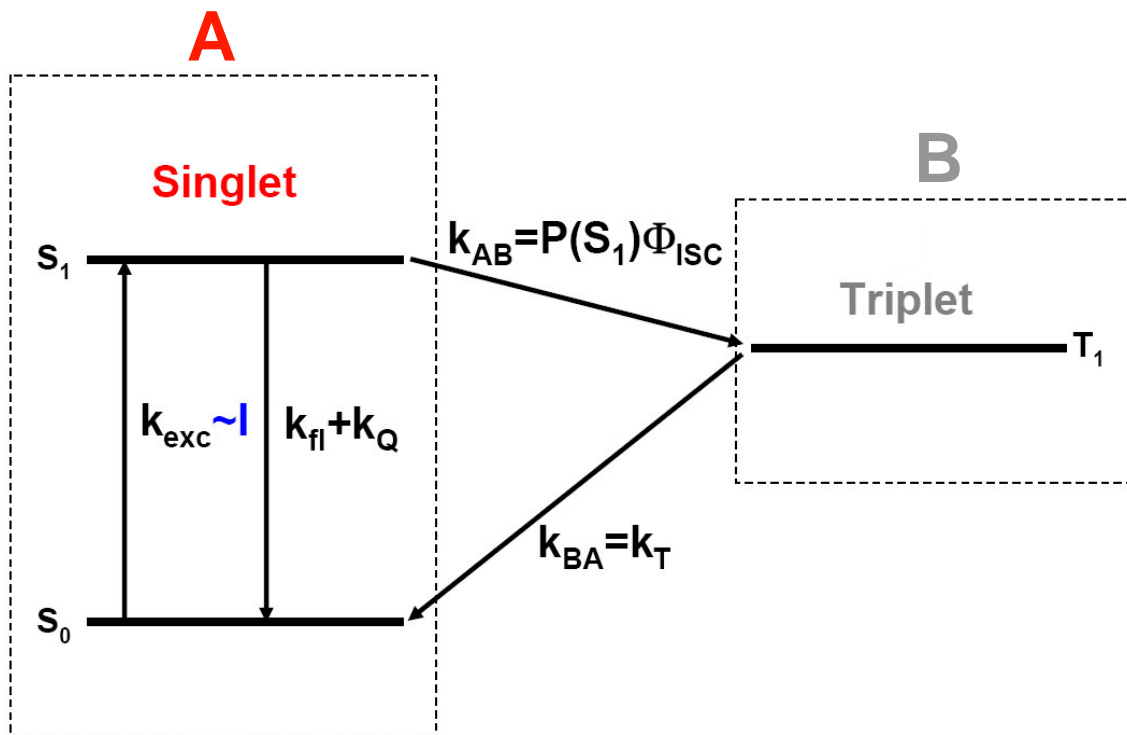


Figure 2.5: Jablonski diagram for GSD: A denotes the bright singlet system and B the dark triplet system according to the RESOLFT concept.  $k_{exc}$  = excitation rate,  $k_{fl}$  = fluorescence emission rate,  $k_Q$  = fluorescence quenching rate,  $k_{isc}$  = intersystem crossing rate,  $k_T$  = triplet decay rate,  $P(S_1)$  = probability that molecule is in  $S_1$ ,  $\Phi_{isc}$  = triplet yield

Another much less probable way for the dye to return to the  $S_0$  state is that the molecule undergoes an intersystem crossing process from the  $S_1$  state to the triplet state  $T_1$  by turning around one electron spin. From that intermediate state the fluorophore returns back to the  $S_0$  state with a much slower rate  $k_T$  than the  $S_1 \rightarrow S_0$  transition. Usually  $1/k_T = \tau_T$  is in the range of  $\mu s$  in solution and  $ms$  to  $s$  in solid media which is much longer than the fluorescence lifetime of several nanoseconds. The other property of the

<sup>1</sup>In the following text, for simplicity, only the triplet state is referred to as the dark state because the discussion applying another dark state would be similar.

triplet state is that it is a dark state, which means it is not emitting fluorescence (usually phosphorescence can be neglected at room temperature). If one now applies a cw-laser illumination on an ensemble of dye molecules with a high enough excitation rate  $k_{exc}$  ( $k_{exc} \sim I$ ), it is possible to shelve the majority of molecules into the dark and longliving triplet state, although the probability of intersystem crossing is much smaller than the probability of fluorescence emission. This is possible because of the longer lifetime of the triplet state. During the illumination process the molecules cycle around between the  $S_0$  and  $S_1$  state but with every cycle a small fraction of molecules ( $\sim 0.1\%$  -  $1\%$  -  $10\%$ , depending on the intersystem crossing rate  $k_{isc}$ ) is trapped in the metastable triplet state. With a high enough excitation intensity, and thus rate  $k_{exc}$ , it is now possible to produce a nearly complete population of the triplet state and thereby effectively switch off the ability to excite the fluorescence, at least for the lifetime of the triplet state. Again it has to be stated that this concept can be transferred to any other long-lived dark state and the triplet is only used for simplicity.

In the RESOLFT concept the singlet system is the bright state A and the triplet system corresponds to the dark state B. The rate  $k_{AB}$  is given by the probability  $P(S_1) = \frac{k_{exc}}{k_{exc} + k_{fl} + k_Q}$  that the molecules are in the  $S_1$  state multiplied with the intersystem crossing probability  $\Phi_{isc} = k_{isc} / (k_{isc} + k_{fl} + k_Q)$  (see figure 2.5). Therefore the rate  $k_{AB}$  from the bright singlet system A to dark triplet system B is the rate for the light driven transition ( $k_{exc} \sim I$ ). The rate  $k_{BA}$  back to the singlet system is the inverse triplet lifetime  $k_T = 1/\tau_T$ .

To calculate the population probabilities for the model in figure 2.5, one can set up a simple rate equations model. The relaxation rates of the higher vibrational states to the vibrational ground state are fast compared to the other rates so that they can be neglected in this simple model (usually the vibrational relaxations are in the range of picoseconds).

$$\begin{aligned}
\dot{S}_0(t) &= -k_{exc}S_0(t) + (k_{fl} + k_Q)S_1(t) + k_T T_1(t) \\
\dot{S}_1(t) &= k_{exc}S_0(t) - (k_{fl} + k_Q)S_1(t) - k_{isc}S_1(t) \\
\dot{T}_1(t) &= k_{isc}S_1(t) - k_T T_1(t)
\end{aligned} \tag{2.10}$$

with

$$S_0 + S_1 + T_1 = 1 \tag{2.11}$$

$k_{exc}$  is the excitation rate,  $k_{fl}$  the fluorescence rate,  $k_Q$  the fluorescence quenching rate,  $k_{isc}$  the intersystem crossing rate,  $k_T$  the triplet relaxation rate and  $S_0$ ,  $S_1$  and  $T_1$  the relative population numbers of the states. After switching on the excitation, the system is equilibrated on a time scale similar to the time scale of the slowest decay rate  $k_T$ . Having reached a stationary state, the relative population numbers do not change anymore, which means that the time derivatives  $\dot{n}_i$  vanish in equation (2.10). Together with equation (2.11) one gets a system of linear equations for the stationary population numbers

with the solution:

$$\begin{aligned}
 S_0 &= 1 - \frac{k_{exc}k_{isc}}{\alpha} \left( 1 + \frac{k_T}{k_{isc}} \right) \\
 S_1 &= \frac{k_T k_{exc}}{\alpha} \\
 T_1 &= \frac{k_{isc} k_{exc}}{\alpha} \\
 \alpha &= k_T(k_{exc} + k_{fl} + k_Q + k_{isc}) + k_{exc}k_{isc}
 \end{aligned} \tag{2.12}$$

From equation (2.12) the equilibrium population numbers of the  $S_0$ ,  $S_1$  and  $T_1$  states can be plotted against the excitation intensity  $I = P/A_{Focus}$  in figure 2.6 ( $P$  is the power and  $A_{Focus}$  the area of the focus). The excitation rate  $k_{exc} = \frac{P\sigma\lambda}{A_{Focus}hc}$  can directly be calculated from the intensity  $I = \frac{P}{A_{Focus}}$ . The plot in figure 2.6 was calculated for typical dye parameters  $k_{fl} + k_Q = 3.33 \cdot 10^8 \text{s}^{-1}$ ,  $k_{isc} = 5 \cdot 10^6 \text{s}^{-1}$ ,  $k_T = 0.5 \cdot 10^6 \text{s}^{-1}$  and  $\sigma = 2 \cdot 10^{-16} \text{cm}^2$ . The excitation wavelength was assumed to be  $\lambda = 532 \text{nm}$ . The plot in figure 2.6 shows that

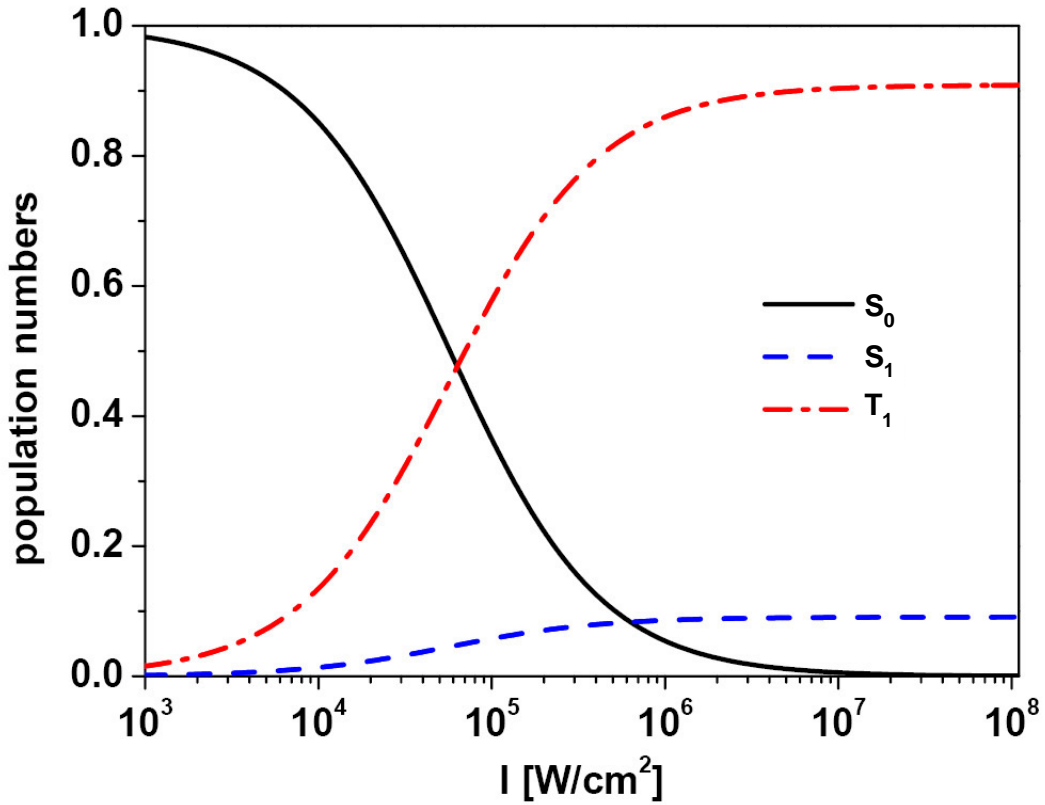


Figure 2.6: Relative steady state populations of the ground state  $S_0$ , the first excited singlet state  $S_1$  and the lowest triplet state  $T_1$  at different excitation intensities  $I$  (see text for used dye parameters for calculation).

the ground state population can be depleted at average intensities in the range of  $MW/cm^2$  (in section 2.4.1 it will be shown how the saturation intensity  $I_{sat}$  can be reduced down to  $kW/cm^2$  and even  $W/cm^2$  if one reduces  $k_T$  or increases  $k_{isc}$ ). At these intensities the

ground state population is almost non-existent,  $\sim 10\%$  of the molecules are in the  $S_1$  state and 90% in the triplet state. The plot in figure 2.6 also illustrates that further increasing of the intensities does not change the population numbers anymore and they are saturated. Altogether the simulation shows that pumping the molecules into the dark triplet state satisfies all requirements for the RESOLFT concept.

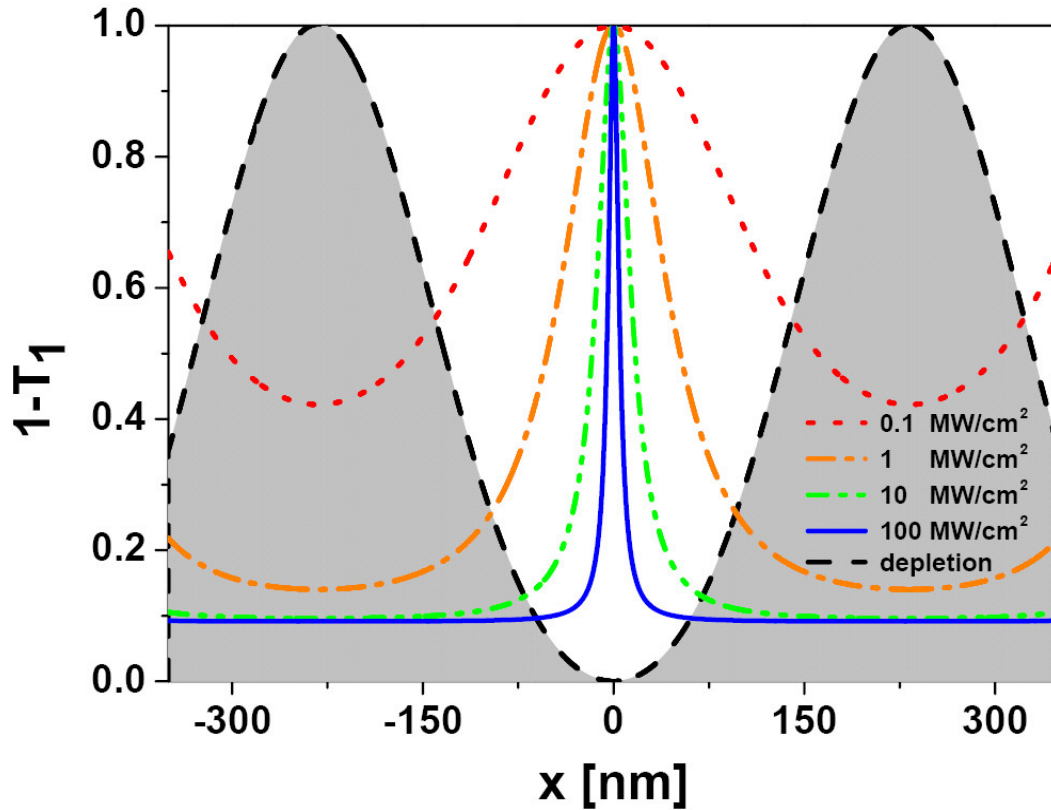


Figure 2.7: Spatial singlet population for different depletion intensities. The region with molecules left in the singlet system is more and more confined to the intensity zero at  $x = 0$  of the depletion pattern where no triplet pumping occurs.

To apply this effect of GSD in a RESOLFT microscope, one has to deplete the fluorescence so that the fluorophores can only be excited in a subdiffraction sized spot. As an example a simple depletion pattern featuring two intensity maxima surrounding an intensity zero at  $x = 0$  is shown in figure 2.7. The intensity zero at  $x = 0$  ensures that the molecules are not pumped into the triplet state at this point but everywhere else. Figure 2.7 also shows the distribution of the dye molecules left in the singlet state for different peak depletion intensities. The spatial singlet population  $S(x)$  distribution along  $x$  can be calculated by:

$$S(x) = 1 - T_1(I(x)) \quad (2.13)$$

$I(x)$  is the intensity distribution of the depletion pattern from which the triplet population is calculated at every point using equation (2.12). For increasing depletion intensities figure 2.7 shows that the singlet population is decreasing everywhere but not at the intensity minimum  $x = 0$ . In that way the area with molecules left in the singlet system is more and more confined to the region at  $x = 0$  where the intensity of the depletion beams is zero and thereby no pumping into the triplet state occurs.

After switching off the depletion the molecules in the  $S_1$  state will rapidly relax to the ground state  $S_0$  in the typical lifetime of several  $ns$  but the molecules in the triplet state will still be trapped for the much longer lifetime  $\tau_T = 1/k_T$  in the range of several  $\mu s$  to  $ms$ . This means, that if one switches on an excitation beam directly after switching off the depletion, the singlet state distribution in figure 2.7 gives the distribution of excitable molecules. Therefore the fluorescence is mainly excited at the intensity zero of the depletion beam resulting in a subdiffraction fluorescence spot whose size is dependent on the depletion intensity.

For example, following the depletion (triplet pumping) pattern of figure 2.7 with a local zero at  $x = 0$  in a confocal microscope setup one would switch on a diffraction-limited excitation beam centered at  $x = 0$  directly after the depletion beam. The effective subdiffraction PSF can then be calculated by multiplying the singlet state dye distribution in equation (2.13) with the excitation PSF (giving the excitation probability) centered at  $x = 0$ :

$$PSF_{eff}(x) = PSF_{exc}(x) (1 - T_1(I(x))) \quad (2.14)$$

The result of this calculation of the effective PSF is depicted in figure 2.8. It is shown that the FWHM of the effective focal spot is more and more reduced with increasing peak depletion intensities up to a FWHM of about  $12nm$  for a peak depletion intensity of  $100MW/cm^2$ .

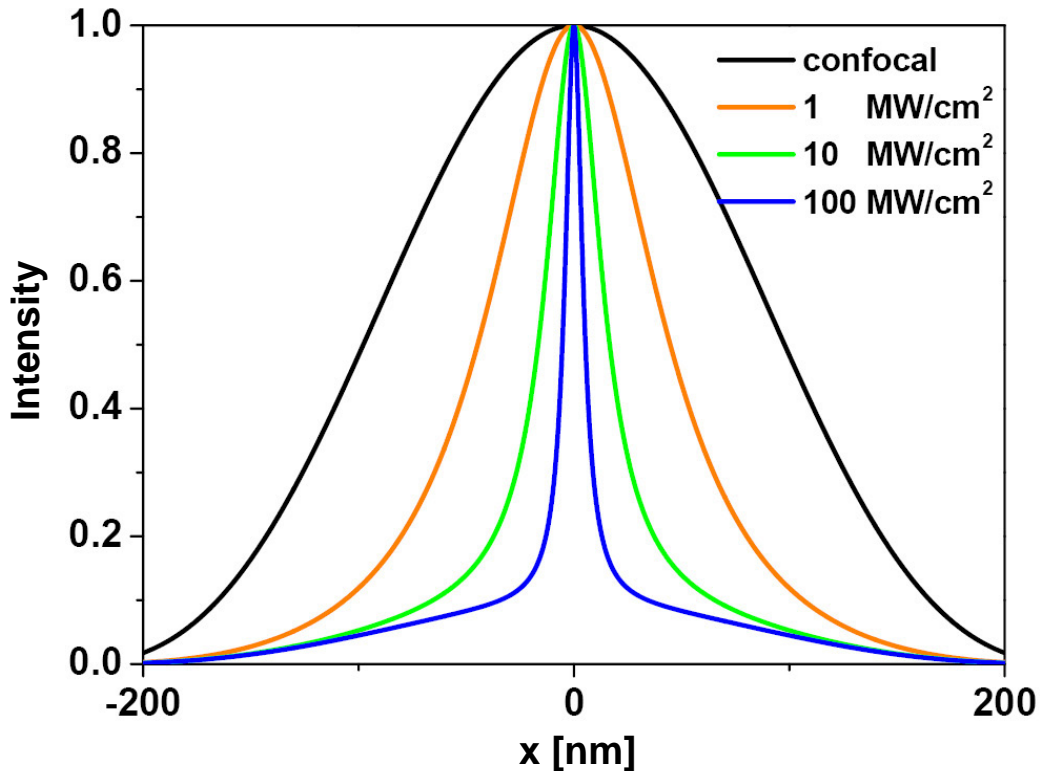


Figure 2.8: Effective PSFs for increasing peak depletion intensities in a confocal microscope: FWHM= $12nm$  for  $100MW/cm^2$ , FWHM= $33nm$  for  $10MW/cm^2$ , FWHM= $90nm$  for  $1MW/cm^2$  compared to the diffraction-limited excitation spot size with a FWHM= $195nm$ .

In figure 2.8 one can also notice that the width of subdiffraction peak is not significantly

reduced at the bottom. The reason for this is that the ground state is not fully depleted in this example thus leaving a residual singlet population of  $\sim 10\%$ .

The maximum possible triplet population for a dye can be calculated using equation (2.12) for  $k_{exc} \rightarrow \infty$ :

$$T_1(k_{exc} \rightarrow \infty) = \frac{k_{isc}}{k_{isc} + k_T} = \frac{1}{1 + k_T/k_{isc}} \quad (2.15)$$

Therefore the triplet population for high depletion powers is determined by the relation of the intersystem crossing rate and the triplet relaxation rate  $k_T/k_{isc}$ . Using dyes with higher  $k_{isc}$  or smaller  $k_T$  rates would decrease the minimum singlet population compared to the shown example. Therefore the resolution would be even higher for such dyes with increased  $k_{isc}$  or reduced  $k_T$ .

## 2.4.1 Engineering the Saturation Intensity

An important parameter for GSD and RESOLFT in general is the saturation intensity  $I_{sat}$  at which half of the molecules have been driven into the triplet state. For useful applications this saturation intensity is favoured to be as small as possible so that as low depletion intensities as possible can be applied to reach highest resolution (compare equation (2.9)). There are two ways to decrease the saturation intensity. Both of them bring their own problems.

One way is to increase the triplet lifetime  $\tau_T = 1/k_T$ , for example, by using rigid environments like polymer matrices. The reason for that is the absence of oxygen or reduced oxygen concentrations because oxygen is a well known triplet quencher. The problem with increasing the triplet lifetime is that in a scanning microscope the focus has to be scanned over the sample. But before scanning to the next point, one has to wait until all molecules have relaxed from the triplet to the singlet state. Consequently high triplet lifetimes would strongly decrease the scanning speed of the microscope. Nevertheless this problem could be avoided by parallelizing the depletion and readout processes using multiple foci and thereby speeding up the scanning process [42, 43].

The other way to decrease the saturation intensity is to increase the intersystem crossing rate  $k_{isc}$ , for example by introducing heavy atom ligands into the dye molecule (thereby the intersystem crossing rate is increased due to the enhanced spin-orbit-coupling). The problem with this case is that by increasing  $k_{isc}$  also the fluorescence quantum yield can be strongly reduced because the intersystem crossing probability is increased.

In general, taking these effects for increasing  $\tau_T$  or  $k_{isc}$  into account, one has to optimize the parameters for  $k_{isc}$  and  $k_T$  carefully to get high enough quantum yield and high depletion efficiency at small depletion intensities. The effect of different rates for  $k_{isc}$  and  $k_T$  is plotted in figure 2.9 where the saturation intensity is plotted against the triplet relaxation time for 3 different intersystem crossing rates. It is shown that either reducing  $k_T = 1/\tau_T$  or increasing  $k_{isc}$  leads to a decrease of the saturation intensity.

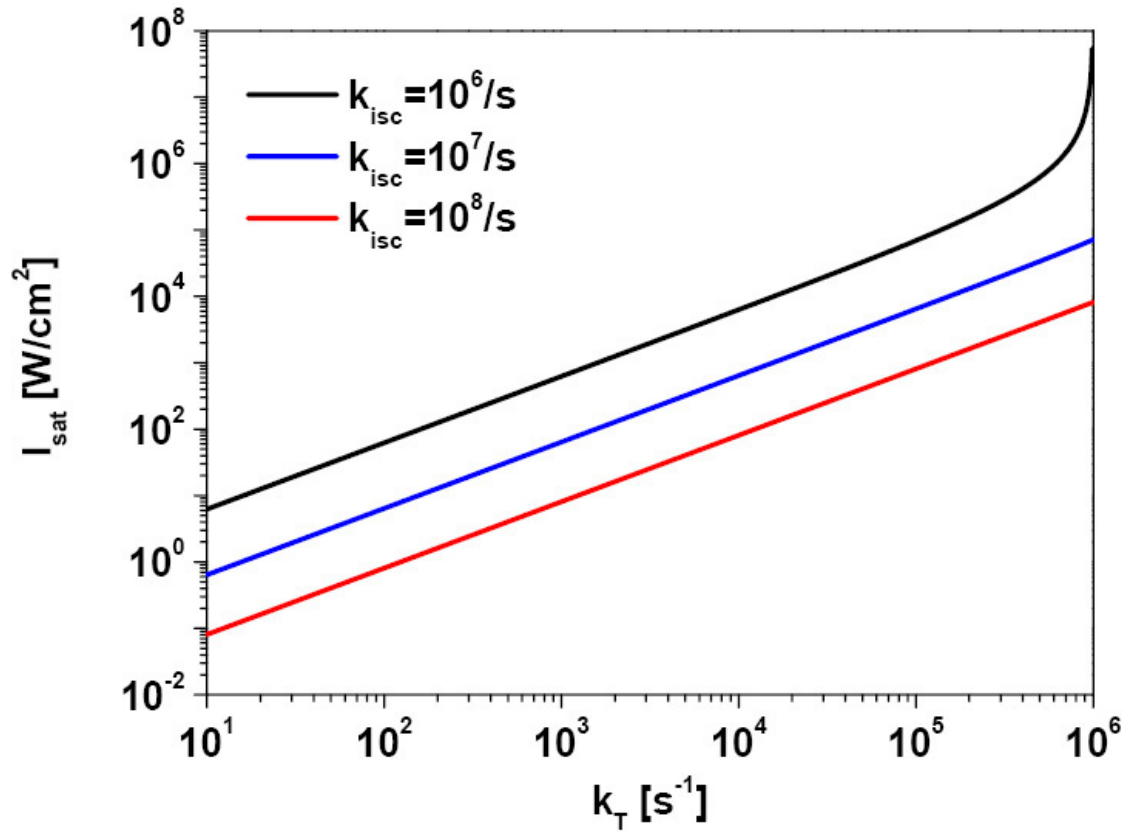


Figure 2.9: Saturation intensity  $I_{sat}$  plotted against the triplet relaxation rate  $k_T$  for 3 different  $k_{isc}$  values, simulation parameters as before.

## 2.4.2 Photobleaching in GSD Microscopy

Since it is well known that bleaching of dye molecules often occurs from the triplet state, it should be discussed in more detail [44, 45]. For better understanding of this issue, a simple 5-state bleaching model is introduced (see figure 2.10). The Jablonski diagram in figure 2.10 additionally contains higher singlet and triplet states. The red arrows mark the major bleaching paths.

A constant bleaching rate  $k_b$  is assumed from the first excited singlet state  $S_1$  and the lowest triplet state  $T_1$ . The bleaching rate from the electronically higher excited states  $S_n$  and  $T_n$  is intensity dependent because the molecules first have to be excited from the  $S_1$  or  $T_1$  to  $S_n$  or  $T_n$  with the excitation rate  $\sigma_x I \frac{\lambda}{hc}$  ( $\sigma_x$  is the excitation cross section for higher states absorption). From these higher singlet states  $S_n$  or higher triplet states  $T_n$  bleaching occurs with a probability  $\Phi_x$ .

Because the dye molecules are pumped into the triplet state in the GSD concept, we can assume that most bleaching will occur from the triplet system. The bleaching probability for molecules in the triplet state can be calculated from the rate constants:

$$p_b^{\text{Triplet}} = \frac{k_b + \sigma_x I \frac{\lambda}{hc} \Phi_x}{k_b + \sigma_x I \frac{\lambda}{hc} \Phi_x + k_T} \quad (2.16)$$

The constant bleaching rate is given by  $k_b$  and the intensity dependent bleaching rate from  $T_n$  is given by  $\sigma_x I \frac{\lambda}{hc} \Phi_x$ ,  $\sigma_x$  is the cross section for higher states excitation and  $\Phi_x$  the bleaching yield from the higher states.

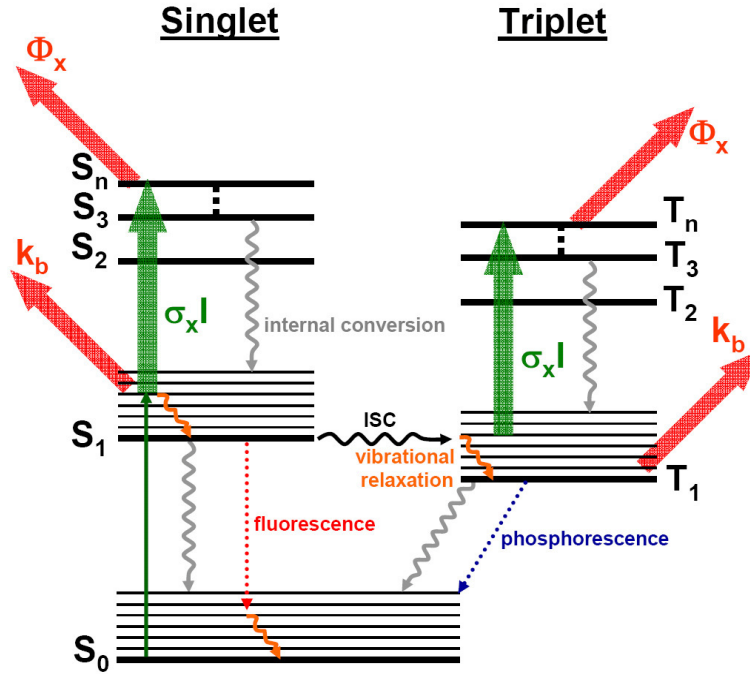


Figure 2.10: 5-state bleaching model. The red arrows mark the bleaching paths. From the  $S_1$  and  $T_1$  states a constant bleaching rate  $k_b$  is assumed. For the bleaching from the higher states  $S_n$  or  $T_n$  the molecules first have to be excited from the  $S_1$  or  $T_1$  where they bleach with a probability  $\Phi_x$ . Hence the bleaching from the higher states is extremely dependent on the excitation intensity.

The bleaching probability  $p_b^{\text{Triplet}}$  from the triplet is plotted against the intensity in figure 2.11a (dye parameters as before) for typical bleaching values taken from [46] ( $\sigma_x = 0.77 \cdot 10^{-16} \text{cm}^2$ ,  $\Phi_x = 5.6 \cdot 10^{-5}$ ,  $k_b = 100 \text{s}^{-1}$ ). The right plot in figure 2.11a shows the triplet population against the intensity. Since the intensity applied in GSD should be much higher than the saturation intensity  $I_{sat}$ , the dotted lines mark  $I = 100 \cdot I_{sat}$  which would be a possible operation intensity for a GSD microscope. The bleaching probability  $p_b$  in figure 2.11a increases at  $\sim 10^4 \text{W/cm}^2$  because at this point the intensity dependent bleaching from higher excited triplet states starts. At  $I = 100 \cdot I_{sat}$ , the bleaching probability already reaches a value of 0.14 which is impracticable for microscopy.

One way to decrease the bleaching probability could be to shift the saturation intensities to smaller values so that the bleaching from higher states would not contribute so strong toward the bleaching rates. As previously shown, the saturation intensity can be decreased by reducing the triplet relaxation rate. In figure 2.11b the bleaching probability for a three orders of magnitude reduced triplet relaxation rate of  $k_T = 10^3/\text{s}$  is plotted against the intensity. The plot on the right shows the triplet population for this smaller  $k_T$  and the intensity of  $I = 100 \cdot I_{sat}$  is also reduced around three orders of magnitude. But if one now compares the bleaching probabilities at  $I = 100 \cdot I_{sat}$  in figure 2.11a ( $p_b = 0.14$ ) and 2.11b ( $p_b = 0.19$ ), it comes out that only upon reducing  $k_T$  the bleaching probability does not change strongly and is even slightly increased. The reason for this is the long

triplet lifetime, because in that case, the small constant bleaching rate  $k_b$  already starts to contribute more to the bleaching probability although the bleaching from higher triplet states does not contribute as strongly as before.

Figure 2.11c shows the bleaching probability for a reduced triplet relaxation rate of  $k_T = 10^3/s$  but also a 10-times smaller bleaching rate  $k_b$  and a 10-times smaller bleaching yield  $\Phi_x$ . In this case  $I = 100 \cdot I_{sat}$  is still smaller than in figure 2.11a but additionally to figure 2.11b also the bleaching probability  $p_b$  is reduced at  $I = 100 \cdot I_{sat}$  to  $p_b = 0.023$ . Therefore, if one can decrease the bleaching probability, one can simultaneously also decrease the intensities necessary for depletion by reducing the triplet relaxation rate  $k_T$ .

The results for the bleaching probabilities at  $I = 100 \cdot I_{sat}$  for the different conditions are summarized in table 2.1.

$k_T [1/s]$	$p_b$ at $I = 100 \cdot I_{sat}$		
	parameters as above	$k_b \cdot 1/10, \Phi_x \cdot 1/10$	$\Phi_x \cdot 1/10$
$10^3$	0.19	0.023	0.1
$10^4$	0.13	0.016	0.023
$10^5$	0.13	0.016	0.016
$0.5 \cdot 10^6$	0.14	0.016	0.016

Table 2.1: Bleaching probabilities for different conditions at intensities of  $I = 100 \cdot I_{sat}$

The bleaching probability cannot be reduced by just going to small triplet relaxation rates. The reason for that is that the smaller triplet relaxation rate leads to a stronger contribution of the constant bleaching rate  $k_b$  from the  $T_1$  state. Of course the smaller depletion intensities resulting from a larger  $k_T$  are favourable for GSD microscopy. If one can secondarily also decrease the bleaching rate  $k_b$  and also the bleaching yield  $\Phi_x$ , it is possible to generate conditions resulting in both small depletion intensities and less bleaching. Reducing the bleaching yield  $\Phi_x$  from higher states only reduces the bleaching probability for large  $k_T$  values and therefore high depletion intensities.

Long triplet lifetimes can be generated by using environments with low oxygen concentrations because oxygen is a well known triplet quencher. Environments free of oxygen also exhibit less bleaching because oxygen also plays a major role as bleaching reagent. Further reduction of bleaching rates can be attained by using anti-bleaching reagents to reduce the bleaching rate  $k_b$  and also the bleaching yield for higher states bleaching  $\Phi_x$ . Therefore, it has been shown that it should be possible to find feasible conditions for GSD microscopy whose practical implementation will be demonstrated in the next chapter.

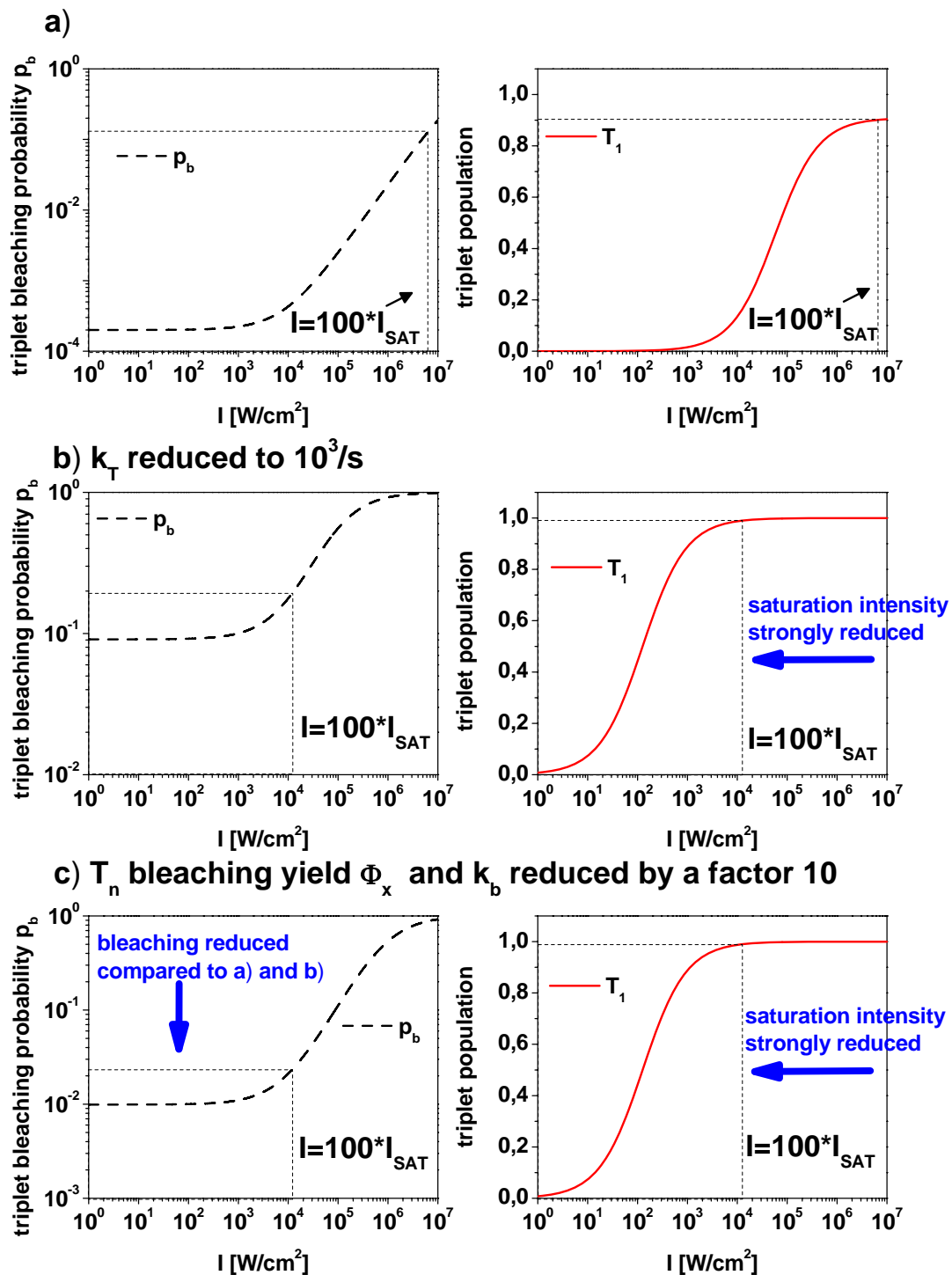


Figure 2.11: Bleaching probabilities from the triplet state plotted against intensity for different conditions and the associated triplet populations. Bleaching parameters from [46] a) Bleaching probabilities and triplet population with unchanged dye parameters. b) The same parameters as in a) but with a reduced triplet relaxation rate  $k_T = 10^3/\text{s}$ . c) Same parameters as in b) but with bleaching yield  $\Phi_x$  and rate  $k_b$  reduced by a factor of 10

### 2.4.3 Engineering the Depletion PSF for GSD Microscopy

Every RESOLFT concept relies on a depletion focus with a central intensity zero where, in the case of fluorescence microscopy, the bright state of the dye molecule is not quenched. Overlapping the depletion PSF with the excitation PSF generates the subdiffraction fluorescence spot (or effective PSF). It is therefore necessary to describe the generation of the local intensity zero in more detail.

A convenient depletion focus should feature an intensity minimum in the center and should be surrounded by strong maxima. The regular focus in a microscope is generated by illuminating the objective lens with a plane wave. The overlapping two beams with a phaseshift of  $\pi$  radians in one beam leads to destructive interference and thereby creates an intensity zero. This effect can be exploited in a microscope by introducing a phase pattern into the illuminating plane wave so that destructive interference is generated in the center of the focus.

One possible phase pattern is shown in figure 2.12a which shifts the phase on one half of the illuminating beam (the polarization has to be parallel to the phase changing plane) by a factor of  $\pi$  (halfmoon phase pattern). Thereby a section of destructive interference

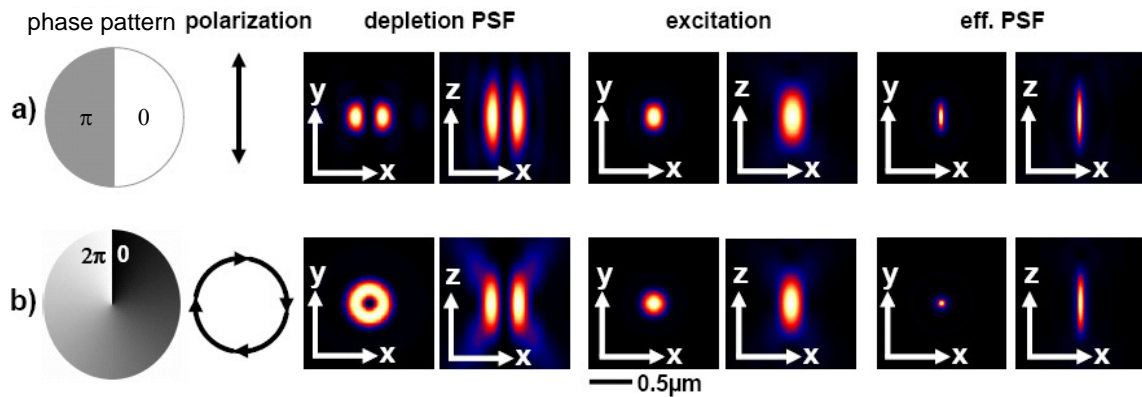


Figure 2.12: Different phase patterns and their resulting PSFs. Depletion was calculated with equation (2.8) ( $k_{BA} = 1$ ,  $\sigma_{AB}\gamma = 1$ ) for  $I_{max} = 10 \cdot I_{sat}$ , other parameters:  $NA = 1.4$ ,  $\lambda = 532nm$ . a) The halfmoon phasemask depletes the fluorescence in one direction, hence resolution enhancement is obtained in one direction. b) The helical phase ramp produces a donut shaped depletion PSF depleting the fluorescence in all lateral directions, hence the resolution is increased in all lateral directions.

is generated along the y-z plane. The resulting depletion PSF is shown in figure 2.12a together with the excitation PSF<sup>1</sup> and the effective PSF. The effective PSF was derived by applying equation (2.8) on the depletion PSF. The resulting residual fluorescence distribution was multiplied with the excitation PSF to obtain the effective PSF. Figure 2.12a demonstrates that this depletion pattern would increase the resolution in one lateral direc-

<sup>1</sup>PSF Calculation tools for calculating the depletion and excitation PSFs were provided by Dr. Jan Keller, Department of NanoBiophotonics, Max-Planck-Institute for Biophysical Chemistry, Göttingen

tion. It is also possible to overlap two of these depletion PSF's, one turned by an angle of  $90^\circ$ , and thereby deplete the fluorescence in all lateral directions [47].

A phase pattern capable of generating a depletion PSF which depletes the fluorescence in all lateral directions is shown in figure 2.12b. The shown helical phase ramp [48] introduces a continuous phase shift from 0 to  $2\pi$  radians. Applying a circular polarized beam with this phase pattern results in destructive interference along the center of the axial direction conducting a donut shaped PSF in the x-y plane (see figure 2.12b). This donut shaped depletion PSF can therefore enhance the resolution in all lateral directions simultaneously.

One way to create the shown phase patterns is to introduce fabricated phase masks into the depletion beam. These phase masks can be produced, for example, by evaporating a thin  $\text{MgF}_2$ -layer with an aluminium mask on a smooth glass substrate or by formed polymer masks. The thickness of the layers the beam passes through have to match the phase retardation condition of the particular phase pattern.

Yet another way to generate a phase pattern in the depletion beam used in this thesis was the application of a spatial light modulator which can produce arbitrary phase patterns from  $0 - 2\pi$  (Hamamatsu, Hamamatsu City, Japan) [49] over a broad range of wavelengths. The feature of generating arbitrary phase patterns also offers the possibility to correct aberrations introduced by imperfect optical elements like lenses or mirrors.

# 3 Experiments

## 3.1 Experimental Realization of a GSD-Microscope

### Pump-Probe Approach

The imaging in GSD microscopy is realized in a pulsed pump-probe mode which is shown in figure 3.1. For image acquisition, the sample is scanned through the focus (green arrow) and the illustrated pulse sequence showing the power of the depletion and the probe pulses and their temporal duration is performed on every pixel. The pulse sequence shown in figure 3.1 is performed on every pixel as follows:

- First, the diffraction-limited confocal excitation beam is switched on to obtain the confocal diffraction-limited image.
- After switching off the confocal beam, the molecules have to relax from the triplet state in time  $t \gg \tau_T$ .
- After triplet relaxation, the donut shaped depletion spot is switched on to pump the dye molecules into the triplet state everywhere but not in its local intensity zero. The power of the depletion spot is higher (see figure 3.1) than that of the probe because it has to be strong enough to shelve the molecules into their triplet state.
- Directly after switching off the depletion beam, the confocal beam is switched on again (with same power as before) to probe the fluorescence left over in the center of the donut (where the fluorescence has not been depleted). Thereby a sub-diffraction fluorescence spot is created with its size depending on the power of the preceding depletion beam.
- After triplet relaxation, the sample is scanned to the next pixel where the complete pulse sequence is repeated.

Both the confocal and the GSD image are acquired simultaneously by scanning the sample through the focus and repeating the pulse sequence on every pixel.

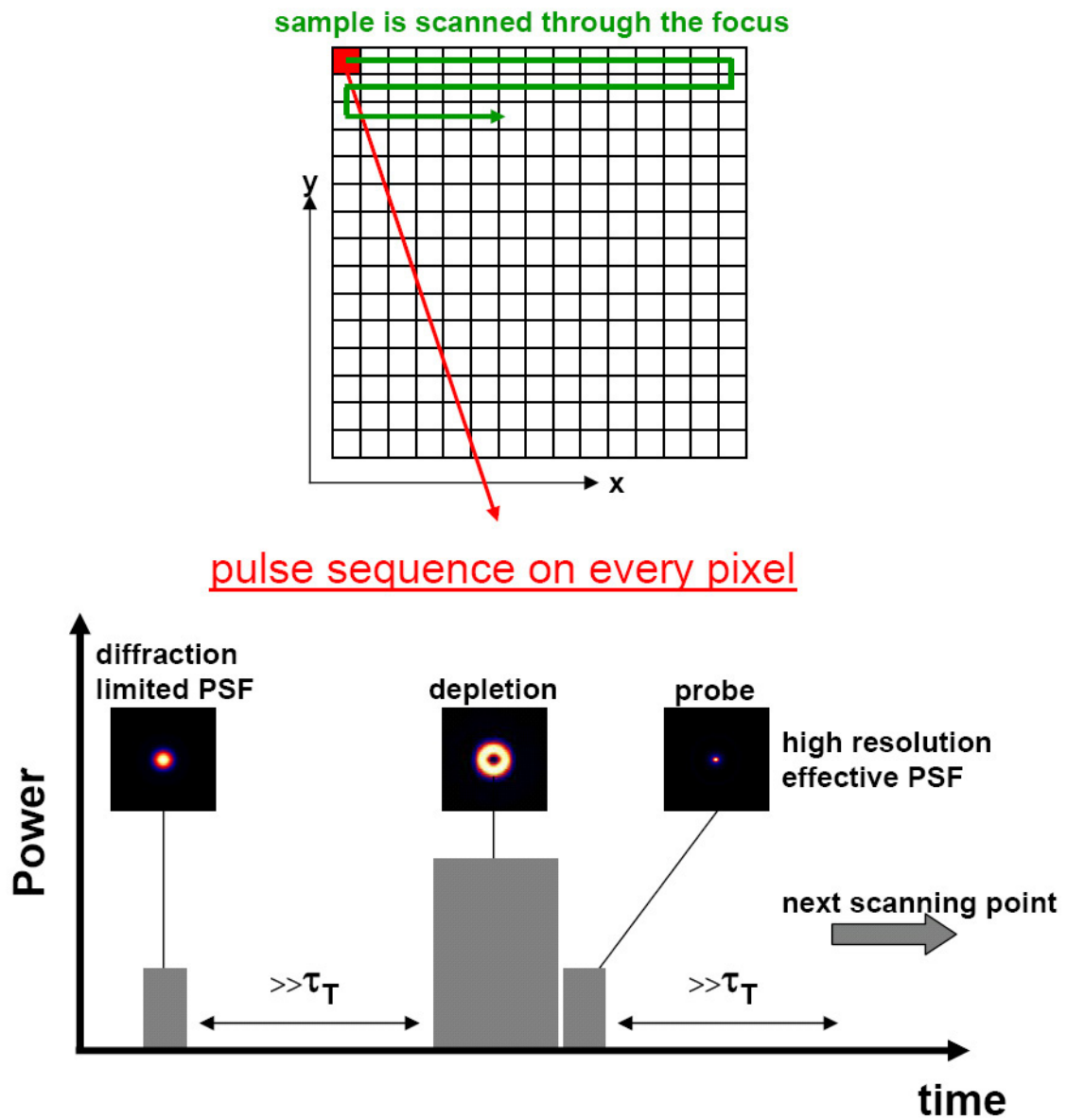


Figure 3.1: Image acquisition in GSD microscopy. The sample is scanned through the focus (green arrow) and the shown pulse sequence on the right is performed on every pixel (marked red). The first pulse without depletion is for obtaining the diffraction-limited image, the third pulse (having the same power as the first one) which follows the donut shaped depletion pulse records the high resolution GSD image.

## Pump-Probe Measurement of Depletion

Since the GSD images are acquired in a pump-probe style, it is necessary to determine the depletion efficiency in the same way. The measurement principle which was a four pulse sequence to obtain the depletion efficiency is shown in figure 3.2a. The sequence of the four diffraction-limited excitation spots is as follows:

- The first low power pulse  $P_1$  serves as a reference signal without the depletion effect.
- After switching off  $P_1$ , the molecules have to relax from the triplet state in time  $t \gg \tau_T$ .
- The strong depletion pulse  $P_2$  shelves the molecules into the triplet state. The power of  $P_2$  is varied to measure the depletion efficiency for different intensities.
- Directly after switching off the depletion pulse  $P_2$ , the residual fluorescence is probed by a second low power pulse  $P_3$  (same power as  $P_1$ ) which excites the molecules left in the singlet state. The residual fluorescence is calculated by comparing the fluorescence signal of  $P_3$  with that of  $P_1$ .
- After switching off  $P_3$ , the molecules have to relax from the triplet state in time  $t \gg \tau_T$ .
- The last pulse  $P_4$  (same power as  $P_1$ ) serves as a control pulse. If the fluorescence signals arising from  $P_4$  and  $P_1$  are the same, all molecules have relaxed from the triplet state showing that the pumping is reversible.

Figure 3.2b shows the fluorescent signal in time for a depletion measurement of EosinY in polyvinylalcohol (PVA). A four pulse sequence (each of them 2ms long) as illustrated in figure 3.2a was used for the experiment. The fluorescence signal of the pump pulse  $P_2$  starts with a strong peak signal and then strongly decreases. Comparing the fluorescence signal of the pulses  $P_1$  and  $P_3$  shows that the peak of initial fluorescence is present for  $P_1$  but is missing for  $P_3$ . The reason for this is that the strong depletion pulse  $P_2$  preceding  $P_3$  shelves the molecules into the triplet state. Therefore pulse  $P_3$  probes the molecules left in the singlet state and by comparing the fluorescence of  $P_3$  with that of  $P_1$  (without a preceding depletion pulse), it is possible to calculate the residual fluorescence. The last pulse  $P_4$  without a foregoing depletion pulse again shows the peak of initial fluorescence like the first pulse  $P_1$ , which verifies that the depletion effect is fully reversible and no fluorescence is lost. The red shaded areas in figure 3.2b mark the integration time of the probe pulses used to calculate the residual fluorescence.

If one repeats the measurement shown in figure 3.2b for different depletion intensities one obtains the depletion curve. Figure 3.3a shows the depletion curve of EosinY in PVA for an integration time of 20 $\mu$ s. The depletion curve shows that the fluorescence for EosinY can be depleted by pumping into the dark triplet state well below 10% saturating at a level of  $\sim 5\%$ .

The fluorescence signal of the probe pulses  $P_1$  and  $P_4$  without a precedent depletion pulse in figure 3.1b also show a strong peak at the start and the fluorescence signal then decreases until an equilibrium is attained. The reason for this is that the probe pulses themselves shelf the molecules into the triplet and this results in two consequences. The first is that one also has to wait for triplet relaxation after the probe pulses like its shown in

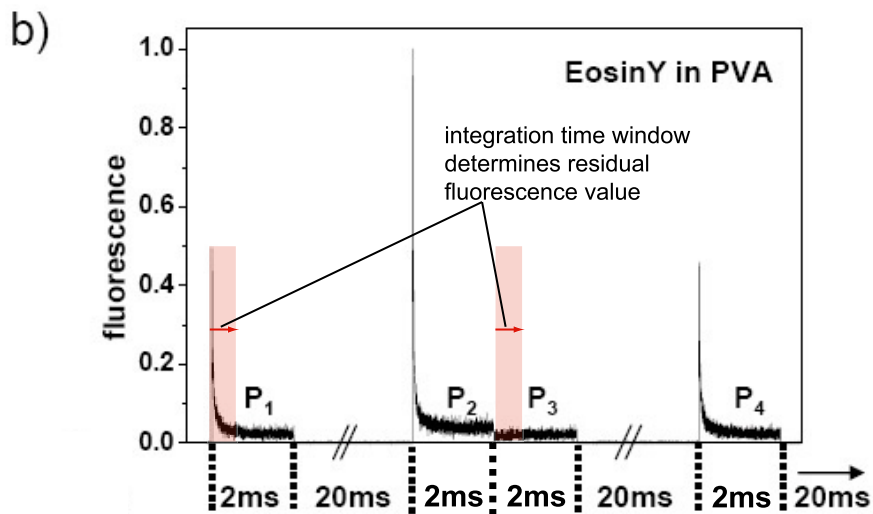
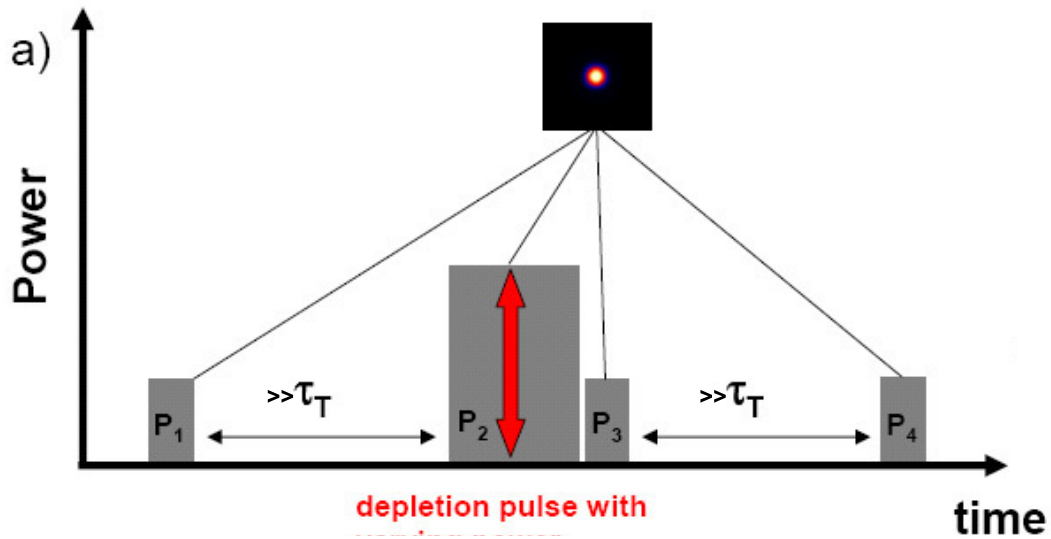


Figure 3.2: Depletion efficiency measurement in GSD microscopy. a) Four pulse sequence of diffraction-limited spots over time,  $P_1$ ,  $P_3$  and  $P_4$  low power probe pulses and  $P_2$  high power pump pulse. Depletion efficiency is measured by comparing the fluorescence from  $P_3$  and  $P_1$ . b) Depletion measurement of EosinY in PVA (probe power  $P_P = 0.5\mu W$  corresponding to a probe intensity of  $I_P = 1.6kW/cm^2$ , depletion power  $P_D = 2.34\mu W$  corresponding to a depletion intensity of  $I_D = 7.45kW/cm^2$ ).

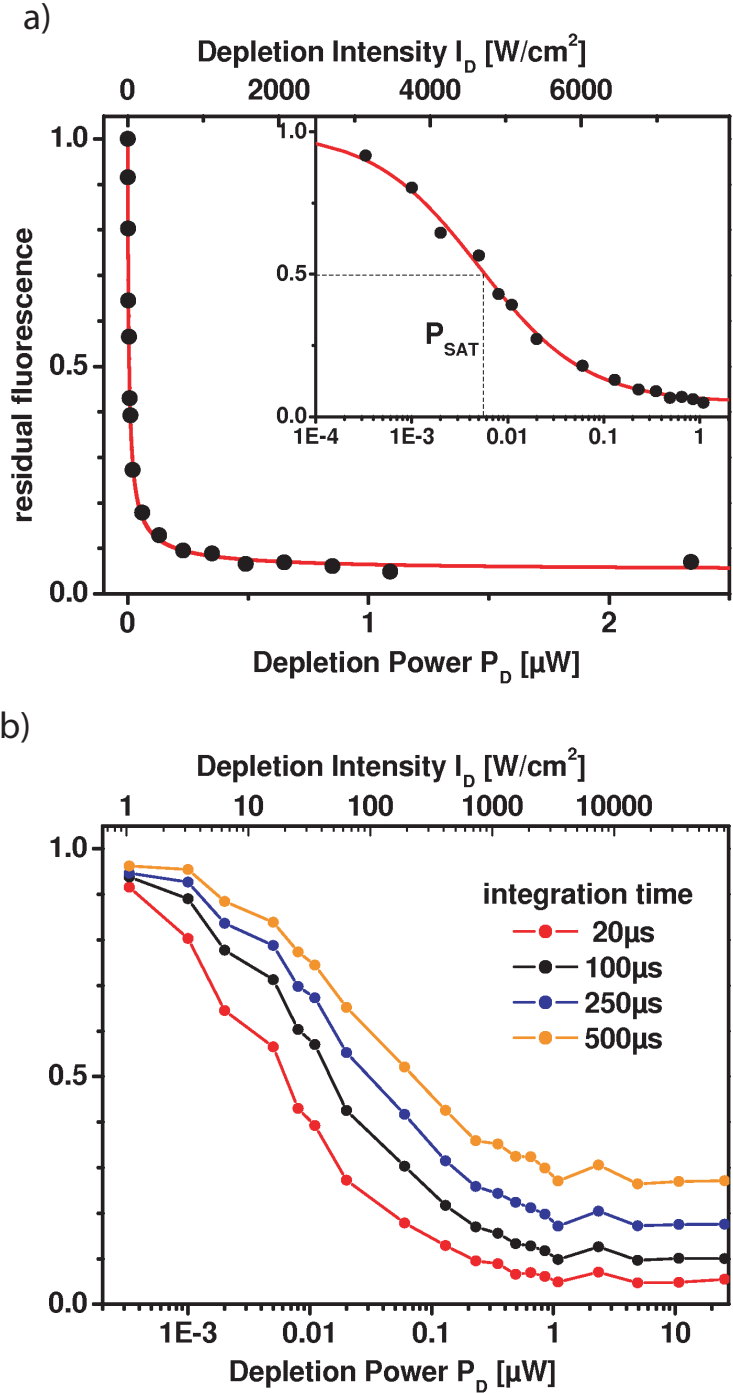


Figure 3.3: a) Fluorescence depletion curve for EosinY in PVA. The logarithmic inset shows the plot for small depletion powers. The saturation power  $P_{sat}$  at which the fluorescence is depleted to half is  $P_{sat} = 6\text{nW}$  which implies a saturation intensity of  $I_{sat} = 20\text{W}/\text{cm}^2$ . The integration time used to determine the residual fluorescence value was  $20\mu\text{s}$ . The red curve is a fit of the fluorescence depletion curve, the probe power was  $P_{probe} = 500\text{nW}$  corresponding to a probe intensity of  $I_{probe} = 1.6\text{kW}/\text{cm}^2$ . b) Fluorescence depletion curves of EosinY in PVA for different probe integration times.

figure 3.2a and 3.2b. The second is that the triplet pumping by the probe pulses influences the integration time used to calculate the residual fluorescence. If the integration time is too long, the probe pulse itself has already pumped a lot of molecules into the triplet which increases the obtained residual fluorescence value. The best residual fluorescence value would therefore be obtained by only using the peak fluorescence signal of the probe pulses, because then nearly no pumping of the probe has occurred yet. But of course, the signal will be very noisy if one only uses the peak fluorescence signal of the probe to calculate the residual fluorescence. Hence the integration time of the probe fluorescence has to be chosen carefully so that one gets enough signal and small enough residual fluorescence values.

The depletion curve for different probe integration times used for the calculation of the residual fluorescence is shown in figure 3.3b. The residual fluorescence saturation level increases with increasing integration times because of probe pumping. For further experiments, an integration time of  $20\mu s$  was chosen because there is still sufficient fluorescence signal at an excellent depletion level.

## Triplet Lifetime Determination

The other parameter determining the effect of GSD depletion by optical shelving is the triplet lifetime. A long triplet lifetime  $\tau_T$  facilitates triplet pumping at low intensities. However this also slows down the image acquisition speed since one has to wait for triplet relaxation between the pulses and each scanning step. Therefore it is important that the triplet lifetime is as long as possible so that optical shelving at small intensities is still possible but at the same time as short as possible so that the image acquisition speed is not too slow.

To measure the triplet lifetime, a sequence of two pulses with equal power was used (see figure 3.4a). The first pulse pumps the molecules into the triplet and the second one probes the fluorescence after the pump pulse with a variable time delay. With increasing time delay, the fluorescence is rising within the triplet lifetime  $\tau_T$  until all molecules have relaxed from the triplet state. An experimental measurement of the triplet lifetime for EosinY in PVA is shown in figure 3.4b. It shows the pump pulse and the triplet recovery curve fitted with a single exponential function with an offset which is given by the residual fluorescence plateau of the pump pulse. The values were calculated using the first  $30\mu s$  of the probe beams peak normalized on the first  $30\mu s$  of the pump peak. Four exemplary probe beams<sup>1</sup> show the increase of the fluorescence over time due to the relaxation from the triplet. The plot in figure 3.4b shows that the fluorescence fully recovers from the triplet state within a triplet lifetime  $\tau_T = 3.9ms$ , which is in good agreement with values from the literature [50].

---

<sup>1</sup>The fluorescence peaks detected during probing sometimes do not exactly fit to the points of the recovery curve. This is because for better statistics, a time window of  $30\mu s$  and not only the peak fluorescence was used for the calculation of the recovery.

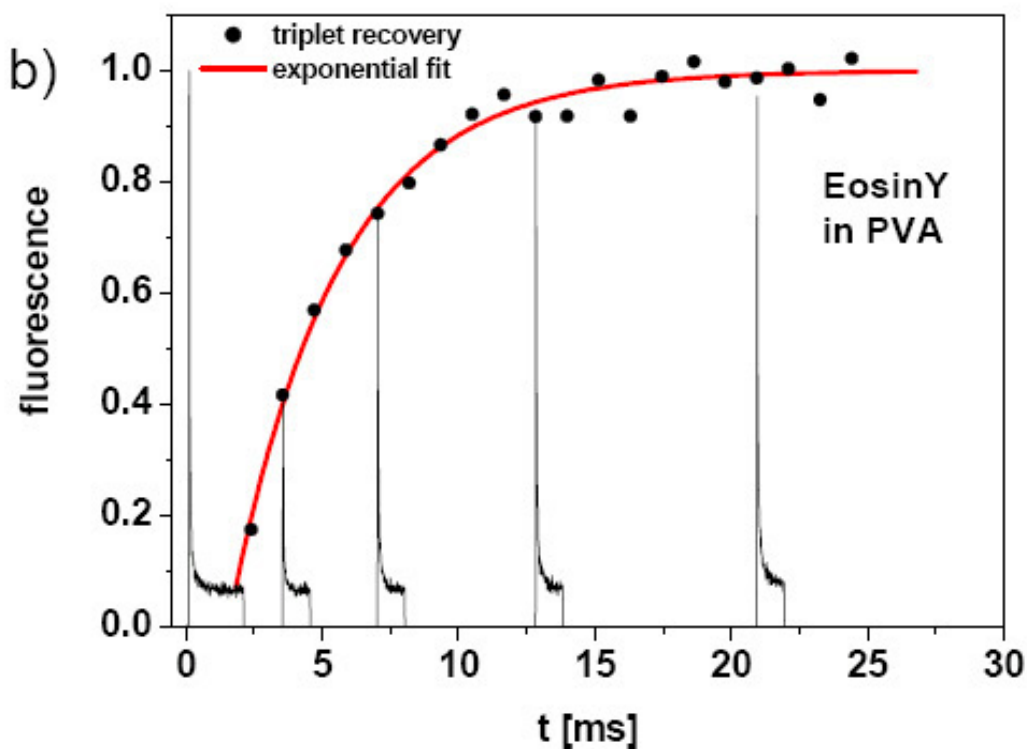
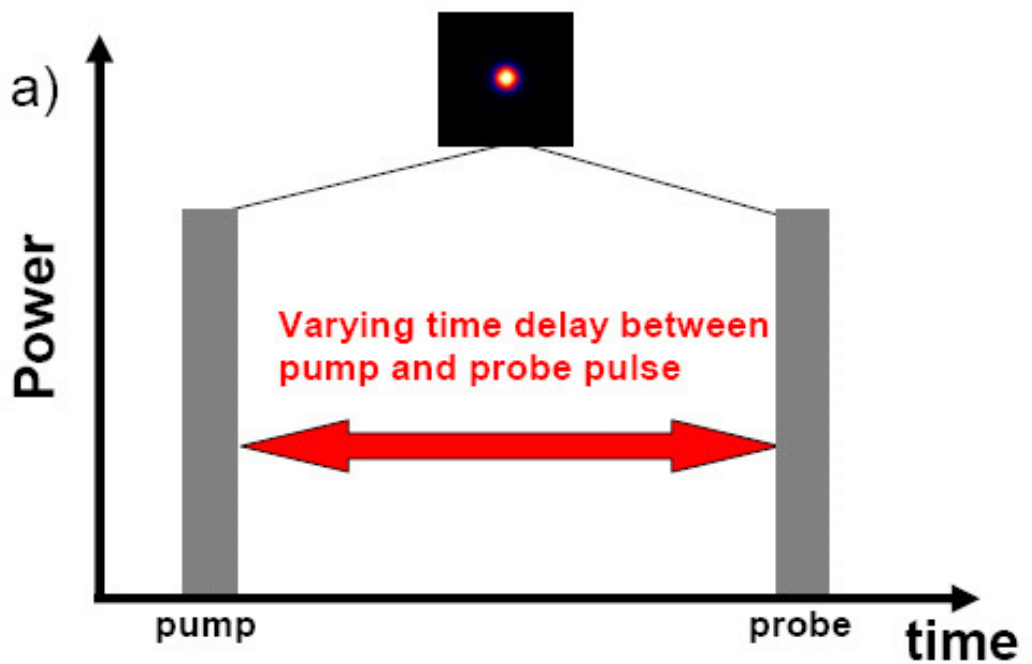


Figure 3.4: a) Pulse sequence for triplet lifetime determination using a diffraction-limited focal spot. The first pulse pumps the molecules into the triplet state and the second pulse with the same power probes the recovery of the fluorescence with a variable time delay. b) Measured triplet lifetime of EosinY in PVA. In addition to the pump pulse, four exemplary probe pulses are shown to demonstrate the recovery of the fluorescence. The triplet lifetime was determined by a single exponential fit to be  $\tau_T = 3.9\text{ms}$ ,  $P = 1\mu\text{W}$  with corresponding intensity  $I = 3200\text{W}/\text{cm}^2$ .

## Photobleaching Measurements

The photobleaching of the dye is critical because the bleaching often stems from the triplet state. Hence if the optical shelving into the triplet state leads to highly increased bleaching rates, GSD microscopy could become impractical.

A simple bleaching measurement is to continuously illuminate the sample with a certain power and record the decrease of the fluorescence signal over time. Such an experiment for EosinY in PVA is depicted in figure 3.5 where the sample was illuminated with intensities of  $I = 3.2kW/cm^2$ ,  $32kW/cm^2$  and  $320kW/cm^2$  for 30s. Figure 3.5 shows that the fluorescence decreases due to photobleaching, over the illumination time of 30s. To

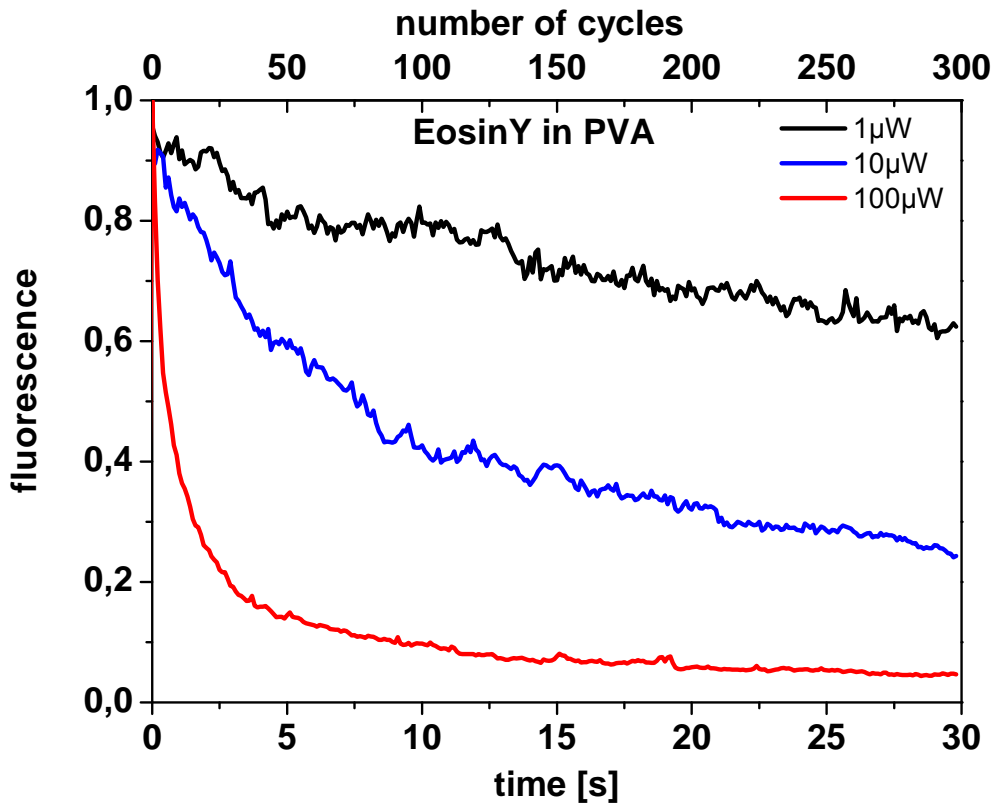


Figure 3.5: Normalized bleaching curve for EosinY in PVA for  $1\mu W$ ,  $10\mu W$  and  $100\mu W$  illumination power, corresponding to intensities of  $3.2kW/cm^2$ ,  $32kW/cm^2$ ,  $320kW/cm^2$ , the upper axis indicates the corresponding number of acquisition cycles in GSD microscopy

connect this bleaching measurement with the pump-probe measurements used in GSD microscopy one has to compare the illumination time of the bleaching measurement with the total illumination time of the pump-probe cycles on a pixel, which is termed the number of cycles in figure 3.5. For a depletion intensity of  $I = 3.2kW/cm^2$ , which is 160 times the saturation intensity  $I_{sat}$  and therefore a feasible depletion intensity for GSD microscopy, after 30s  $\sim 35\%$  of the molecules are bleached away. A constant illumination

time of 30s corresponds to 300 repetitions (number of cycles) of the illumination process usually performed only one time on a pixel in GSD microscopy. Taking into account that, of course, the focus has to be moved to record the GSD image this shows that bleaching for EosinY in PVA should not prevent the realization of GSD microscopy at an depletion intensity of  $3.2kW/cm^2$ . At higher intensities of  $32kW/cm^2$  or  $320kW/cm^2$  already 65% and 95% respectively of the molecules have bleached after 300 cycles as shown in figure 3.5. In this case the bleaching is already so large that it is a problem in imaging and prevents the use of higher depletion intensities and therefore better resolution.

## 3.2 Experimental Setup

The setup used for the experiments is a confocal microscope as shown in figure 3.6. A 5W laser excitation source at a wavelength of 500nm was used (Verdi V5, Coherent). The laser radiation was coupled into a polarization maintaining fiber and the output was collimated by lens L1 resulting in a beam of a diameter about 2mm. For reducing the power fluctuations a laser power controller (LPC, BEOC) was used. The beam leaving the LPC is split into two equal parts by a beam splitting cube (BC) (non-polarizing, 50:50), one of them is the ground state depletion beam and the other one is the probe beam. In both

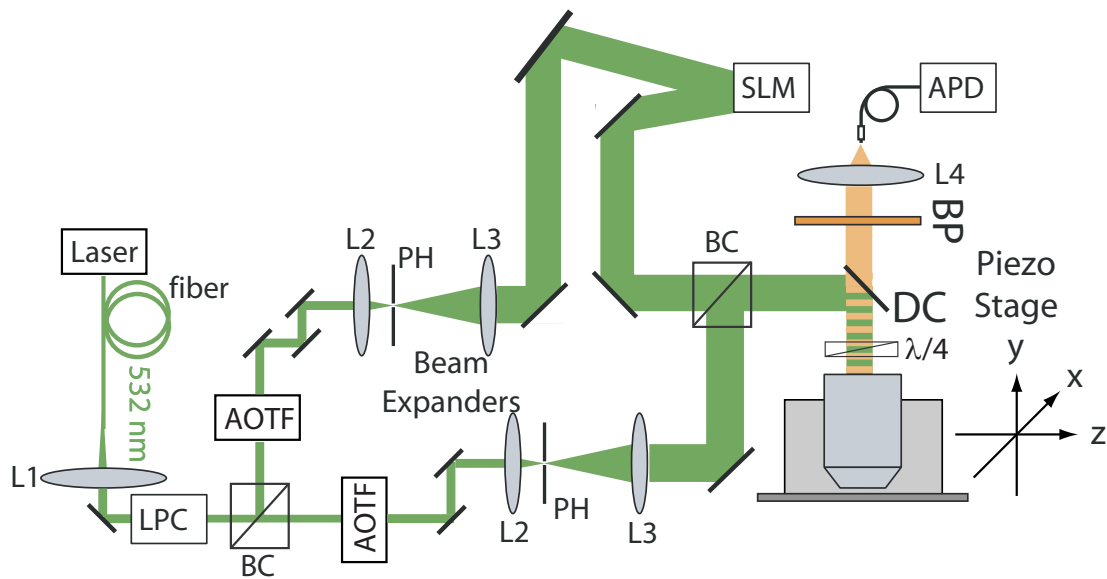


Figure 3.6: GSD microscopy setup

beams acousto-optical tuneable filters (AOTF) (AOTFnC-VIS, AA optoelectronics) are used to switch the beams independent from each other either on and off. The switching speed of the AOTFs was limited to about  $2\mu s$  and for experiments in aqueous solution, they had to be replaced with acousto optical modulators (AOM) whose switching speed is up to  $8ns$  (MT200-A0.5-VIS, AA optoelectronics). In order to get a Gaussian beam shape, a spatial filter comprising of two lenses (L2, L3) and a pinhole (PH) was introduced in both beams. The ground state depletion beam also contained a spatial light modulator (SLM, Hamamatsu) to generate arbitrary phase patterns in the beam profile for creating the depletion PSF. Both the depletion and the detection beam are combined with a second beamsplitting cube (BC). Both beams are then directed onto a dichroic mirror (DC) which reflects the excitation light into the objective (Plan APO 100x, NA=1.4, Leica) focussing the light onto the sample. A  $\lambda/4$  plate can be inserted in front of the objective for generating circularly polarized light when using the helical phase ramp on the SLM to generate a donut shaped depletion PSF. The formed diffraction-limited excitation beam excites the dye molecules and the emitted fluorescence is collected by the same objective and sent through the dichroic mirror into the detection pathway. Here, the fluorescence light passes through a bandpass filter (BP) (for reducing the background and removing

the excitation laser line) on the lens L4 which focusses the light onto the detector fibre. A single photon counting avalanche photodiode (APD) (SPCM-AQR-13-FC, Perkin Elmer) is used as the detector. The inner core diameter of the detector fibre is equivalent to the confocal pinhole with a diameter of  $62,5\mu\text{m}$  which is about 0.7 times the airy disc of the imaged focus. The sample is mounted on a three-dimensional stage (NanoMax, Melles Griot) which can be moved mechanically for coarse adjustment but also has closed-loop 3 axis piezos to scan the sample for imaging.

The excitation PSF and the depletion PSF are measured by scanning a sample with  $80\text{nm}$  gold beads (BB International, Cardiff, UK) on a coverslip and detection of the scattered laser light on a nonconfocal detector. The reflected signal from the gold bead is directed by an extra flip mirror in the detection pathway onto the nonconfocal detector (photomultiplier tube, Perkin Elmer). In that way it is possible to determine the shapes of the PSFs, align them, and overlap the excitation and the depletion beams.

The incident power is measured in front of the objective. In order to measure only that light which arrives in the focus, an aperture is placed in front of the power meter (Field Master, Coherent) that matches the entrance aperture of the objective. The transmission of the objective is  $\sim 80\%$  and therefore all measured power values have to be scaled with this factor.

For the fluorescence correlation spectroscopy (FCS) measurements the APD signal was sent to a hardware correlator (model ALV 6000, ALV GmbH, Langen, Germany).

The electrical setup is shown in figure 3.7. A multichannel scaler card (MCD, Fast-Comtech) counts the fluorescence signal from the APD and also generates a synchronisation signal for the timing of the whole experiment. The synchronisation signal of the MCD card triggers a pulse generator (Model 9514, Quantum Composers) which sends the pump-probe pulse sequence to a custom-made switchable voltage supply in order to transfer the adjusted voltages to the two AOTFs in the depletion and the detection beams. The pulse generator itself is programmed via the measurement software over the RS-232 interface of the computer. The scanning of the piezo stage is controlled by the voltage levels from the National Instruments DAC (NiDAC) card which generates the control voltages for the x, y and z position of the controller and thereby enables the scanning of the sample.

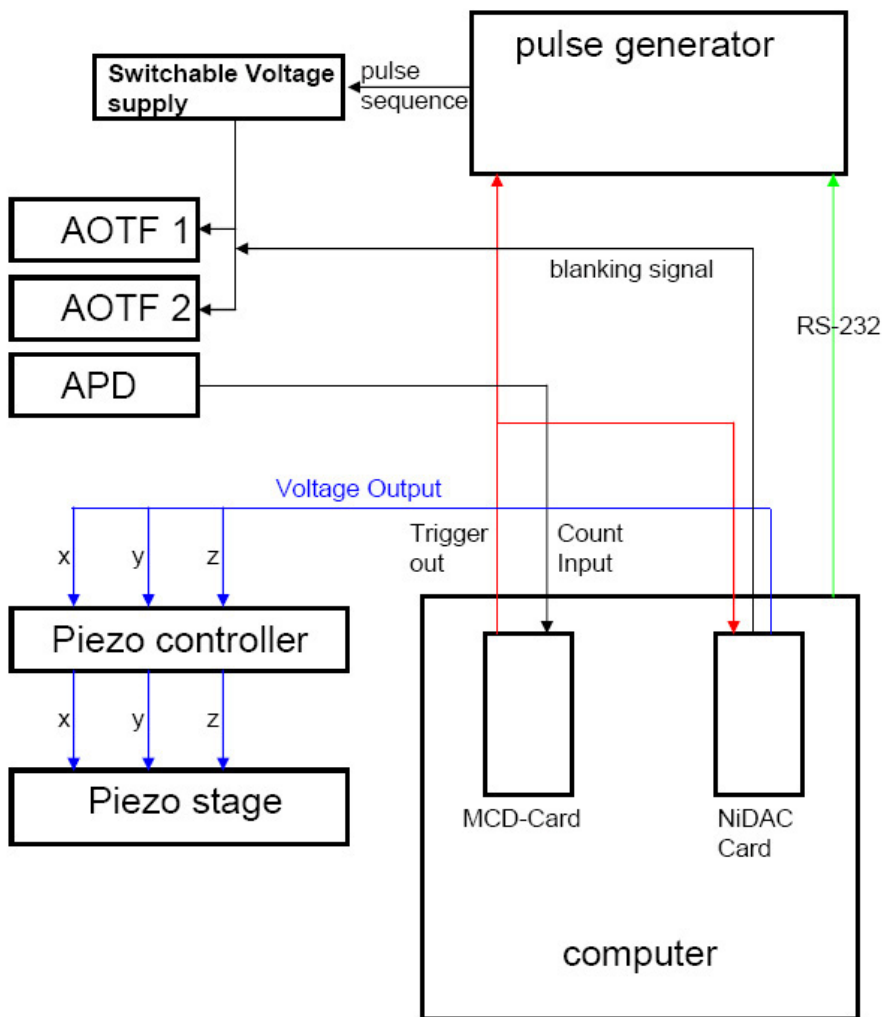


Figure 3.7: Electrical setup

## 3.3 Generality of the Depletion Concept

Further, usually every dye molecule has a triplet state or another dark state, still it is important to prove this generality and test different dyes whether their fluorescence can sufficiently be depleted by pumping into the triplet or another dark state<sup>1</sup>. In this case GSD would not be limited to a few special dyes.

### 3.3.1 Ground State Depletion in Polymer Matrices

The use of rigid matrices as mounting media for the dyes results in less mobility of triplet quenchers like oxygen. Thus the lifetime  $\tau_T$  of the triplet state is often prolonged in rigid media. This increase of the triplet lifetime leads to a decrease of the intensities needed to realize a strong degree of saturated fluorescence depletion. Hence the use of rigid environments is favourable for GSD microscopy.

The reduction of the triplet lifetime is, for example, well known for fluorescent dyes in polymer matrices like polyvinylalcohol (PVA). In solution, the triplet lifetime is in the range of several microseconds while in PVA it is usually in the range of milliseconds, i.e. three orders of magnitude longer than in solution due to the reduced triplet quenching or often also because of involvement of other dark states [45].

The polymer matrices used in the experiments were PVA and polymethylmetacrylate (PMMA). For sample preparation the polymer with the dye was spin-coated onto the coverslip. The result is a thin film of the polymer of  $\sim 200\text{nm}$  thickness containing the dye (see appendix A.3 for sample preparation protocol).

The effect of oxygen permeability of rigid environments on the triplet lifetime can be demonstrated for EosinY in PVA and PMMA. Figure 3.8 shows a plot of two measurements of the triplet lifetime of EosinY in PMMA. The first measurement was performed under air conditions (oxygen present) while the second measurement was performed under nitrogen flow to remove the oxygen from the sample. Under air conditions, the triplet lifetime was  $\tau_T = 1\text{ms}$ , which is three orders of magnitude larger than the  $\sim \mu\text{s}$  lifetime in aqueous solution. Hence this measurement demonstrates the decreased triplet quenching rate in PMMA. For the same sample flushed with nitrogen, the triplet quenching was reduced even more so that the triplet lifetime increased to  $\tau_T = 3.6\text{ms}$ . The reason for that is that PMMA is not fully impermeable to oxygen and therefore the residual oxygen can be removed from the sample by nitrogen flushing.

The results of this experiment are summarized in table 3.1 together with the triplet lifetime of EosinY in PVA and a typical triplet lifetime in aqueous solution. The triplet lifetime measurement performed for EosinY in PVA under air conditions was already shown in figure 3.4b where a triplet lifetime of  $\tau_T = 3.9\text{ms}$  was determined. Performing the same measurement with EosinY under nitrogen flow does not have any effect on the triplet

---

<sup>1</sup>In the following text only the triplet state is referred to as the dark state for simplicity. But, in principle, any other dark state can be used for optical shelving. One can assume without loss of generality that the observed dark state is the  $T_1$  or another dark state that is populated through the  $T_1$ . The important issue is that one can shelve the molecules into the dark state and that the dark state is metastable (so that the molecules return to the ground state).

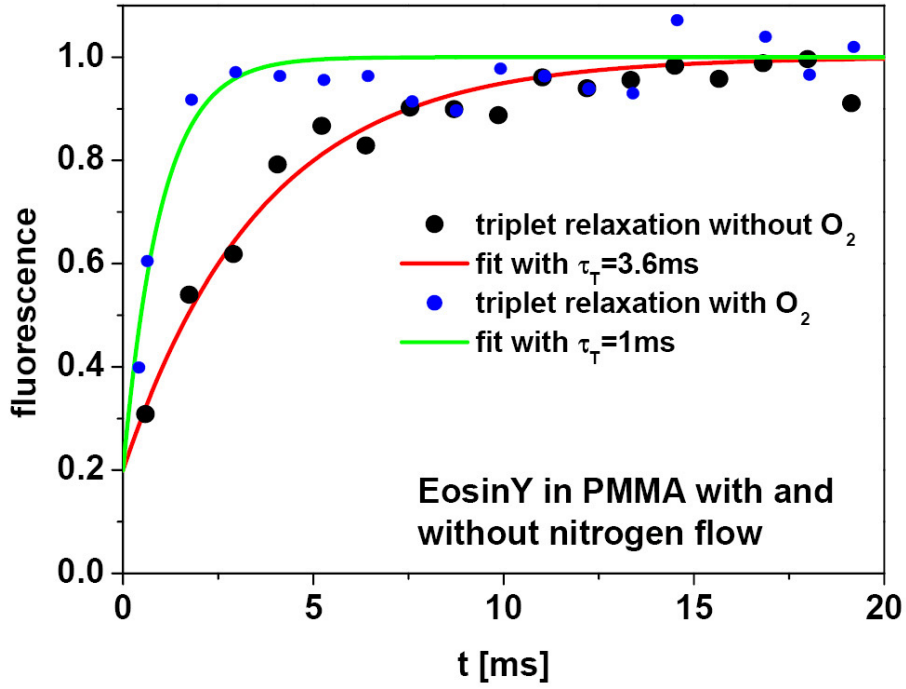


Figure 3.8: Measured triplet lifetime for EosinY in PMMA with and without nitrogen flow ( $P = 5\mu W$  equals  $I = 16kW/cm^2$ )

lifetime. Thus PVA is nearly impermeable to oxygen. However, both PMMA and PVA show a strong decrease of the triplet lifetime compared to the  $\sim \mu s$  lifetime in aqueous solution. For that reason these experiments demonstrate the possibility of increasing the triplet lifetime  $\tau_T$  and decreasing the saturation intensity for GSD.

	EosinY/PVA	EosinY/PMMA	aqueous solution
$\tau_T$ [ms] with oxygen	3.9	1.0	$\sim 0.001$
$\tau_T$ [ms] without oxygen	no effect	3.6	

Table 3.1: Triplet lifetime of EosinY in different environments with and without oxygen in comparison with a typical triplet lifetime in aqueous solution

### 3.3.2 Ground State Depletion in Vectashield

Another mounting medium which showed adequate properties for GSD microscopy was Vectashield (Vector Laboratories, Burlingame, CA). Vectashield is a commercially available mounting medium containing a pH 8.5 buffered water-glycerol solution and para-Phenylenediamine (PPD) as an anti bleaching reagent [51]. First, the water-glycerol solution makes this liquid extremely viscous compared to pure water which results in a strong decrease of the collision frequency between the molecules [52]. Second, the antibleaching reagent PPD acts as an oxygen and radical scavenger which decreases the molecular oxygen and radical concentration. Therefore the triplet lifetime in Vectashield is increased and also the bleaching is reduced at the same time. This makes it possible to pump the molecules into the triplet state with rather small intensities and to apply relatively large saturation degrees of depletion without significant photobleaching.

As an example, the fluorescence depletion curve of single Atto532 labeled antibodies is is

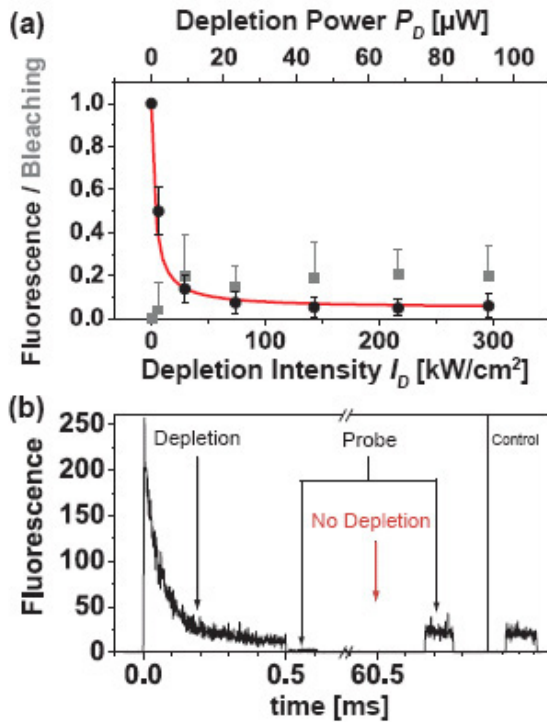


Figure 3.9: Fluorescence depletion of single Atto532 labeled antibodies by triplet state ( $T_1$ ) buildup. (a) Fluorescence (black) and fraction of bleached molecules after 25 depletion-probe cycles (gray) as a function of the depletion intensity  $I_D$  or power  $P_D$ ; error bars as relative standard deviation from 5 consecutive measurements. (b) Depletion-probe cycle with strong depletion illumination ( $500\mu s$ ,  $I_D = 85kW/cm^2$ ), depleting the fluorescence due to  $T_1$  buildup; subsequent low-power illumination ( $100\mu s$ ,  $I_P = 7kW/cm^2$ ) probing the residual fluorescence signal. After depletion and complete relaxation of the  $T_1$  ( $\sim 60ms$ ), fluorescence emission is completely recovered, as observed by comparison with the signal gained just with the probe beam (Control).

shown in figure 3.9a. The Atto532 dye molecules were bound to antibodies (antimouse IgG, Jackson ImmunoResearch Laboratories) and mounted in Vectashield in order to have the same chemical environment as in immunofluorescence imaging. Figure 3.9a shows that for depletion intensities as low as  $I_D = 10kW/cm^2$ , the fluorescence is depleted by half, and rather modest values of  $I_D > 50kW/cm^2$  deplete the ground state to  $<10\%$  without exacerbating bleaching. The bleaching curve in figure 3.9a shows that one can repeat the depletion probe cycle 25 times with only 20% photobleaching.

The depletion probe cycle is illustrated in figure 3.9b. It shows the fluorescence depletion directly after the pump pulse and that the fluorescence completely recovers after 60ms ( $\tau_T \approx 10ms$ ).

In summary, Vectashield proved to be an appropriate mounting medium for GSD microscopy. One can deplete the fluorescence down to  $<10\%$  without exacerbating bleaching at reasonable dwell times of  $60ms$  ( $\tau_T \approx 10ms$ ). Furthermore the depletion was measured on dye labeled antibodies showing the applicability of GSD microscopy in Vectashield on biological samples.

### 3.3.3 Ground State Depletion in Aqueous Solution

Testing the possibility of GSD in aqueous solutions is of particular importance because it would offer the chance to perform sub-diffraction imaging in living cells.

One problem in GSD microscopy in aqueous solution is the usually short triplet lifetime  $\tau_T$  of several microseconds which makes optical shelving into the triplet state complicated. This is illustrated in figure 3.10a. It shows a plot of the steady state singlet population ( $1 - T_1$ , see equation (2.12)) calculated for increasing intensity for three different intersystem crossing rates  $k_{isc}$  (typical dye parameters for solution,  $\lambda = 532nm$ ,  $k_{fl} + k_Q = 3.33 \cdot 10^8 s^{-1}$ ,  $k_T = 0.5 \cdot 10^6 s^{-1}$ ,  $\sigma = 2 \cdot 10^{-16} cm^2$ ,  $k_{isc}$  see figure 3.10a). The plot shows that the maximum depletion strongly differs for the different intersystem crossing rates  $k_{isc}$ . For  $k_{isc} = 10^6/s$  the maximum depletion is only  $\sim 35\%$  while for larger  $k_{isc}$  a total depletion of  $\sim 10\%$  ( $k_{isc} = 5 \cdot 10^6/s$ ) or  $\sim 1\%$  ( $k_{isc} = 5 \cdot 10^7/s$ ) can be reached.

Figure 3.10a also shows that the saturation intensity is decreased by increasing  $k_{isc}$ . This decrease of the saturation intensity also decreases the bleaching probability at the applied intensities in GSD microscopy. This behaviour is illustrated in figure 3.10b where the triplet bleaching probability  $p_b$  is calculated for increasing intensity ( $p_b$  was calculated with equation (2.16), same bleaching parameters as in section 2.4.2). The lines mark the saturation intensities for the same  $k_{isc}$  values as used in figure 3.10a. The plot shows that the decreased saturation intensities following larger  $k_{isc}$  result in a decreased bleaching probability.

The results of this simulation are summarized in table 3.2. The bleaching probability

	$k_{isc} [1/s]$		
	$10^6$	$5 \cdot 10^6$	$5 \cdot 10^7$
$p_b$ at $I = I_{sat}$	0.014	0.0018	$3.6 \cdot 10^{-4}$
$p_b$ at $I = 100 \cdot I_{sat}$	0.59	0.14	0.016
maximum depletion	$\sim 0.34$	$\sim 0.1$	$\sim 0.01$

Table 3.2: Simulation results for different intersystem crossing rates  $k_{isc}$

reaches a value of  $p_b = 0.34$  for  $k_{isc} = 10^6/s$  at a feasible intensity for GSD microscopy of  $I = 100 \cdot I_{sat}$ . This high bleaching probability and the maximum depletion value of only  $34\%$  makes GSD microscopy impracticable for such dye parameters. But with an increased  $k_{isc} = 5 \cdot 10^7/s$ , the bleaching probability is only  $p_b = 0.01$  at  $I = 100 \cdot I_{sat}$  and the maximum depletion is  $\sim 0.01$ . Therefore GSD microscopy in aqueous solution is possible by using dyes with an increased intersystem crossing rate  $k_{isc}$ . Of course the intersystem crossing rate should not be too large because a too large intersystem crossing rate also decreases the fluorescence quantum yield of the dye (the fluorescence quantum yield

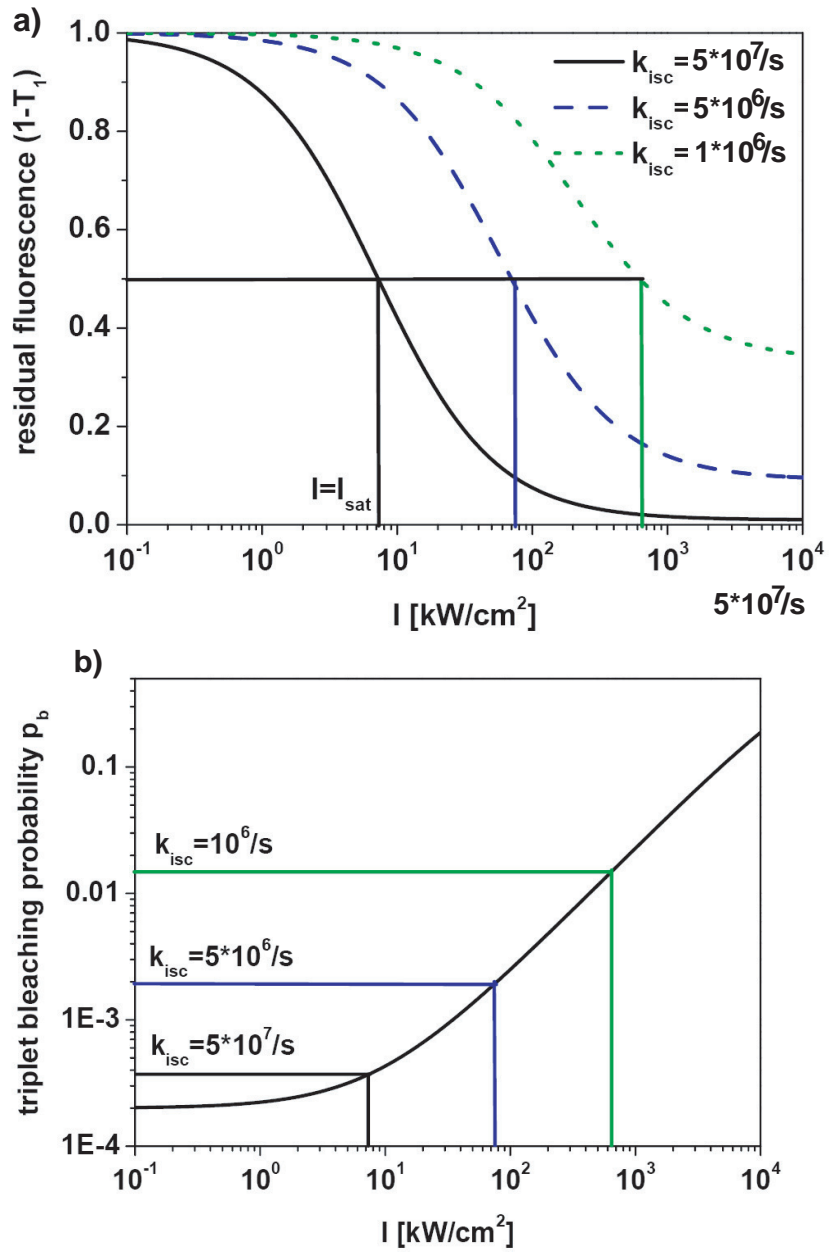


Figure 3.10: a) Simulated depletion curves for different  $k_{isc}$ . b) Simulated bleaching probability from the triplet. The lines mark the different saturation intensities for different  $k_{isc}$  values and the corresponding bleaching probabilities  $p_b$ .

gives the probability of fluorescence emission after excitation). But for the intersystem crossing rates used in the simulations it should be possible to find dyes with these parameters which still have a sufficient fluorescence quantum yield. For example, the dye with the highest  $k_{isc} = 5 \cdot 10^7 / s$  still has a fluorescence quantum yield of  $\Phi_{fl} = 0.87$  (with the assumption that  $\Phi_{fl} = 1$  without intersystem crossing).

One possible candidate for GSD microscopy in solution is the dye AZ174 (Thiorhodamine, Attotec, Siegen). Since fluorescence correlation spectroscopy (FCS) is a powerful method to determine the kinetic parameters of dyes in solution, such measurements were performed for AZ174 [53, 54, 55]. FCS makes use of temporal fluorescence fluctuations of the dye molecules in the focus, for example due to diffusion or transitions to dark states like the triplet. The measured signal is analyzed using the temporal autocorrelation function from which one obtains the kinetic rates of the dye molecules like  $k_{isc}$ ,  $k_T$  and the fraction of molecules in the triplet state according to procedures outlined in [56]. A correlation curve of AZ174 in phosphate-buffered-saline (PBS) with pH 7.5 measured by FCS is depicted in figure 3.11 showing a triplet fraction of  $\sim 60\%$  at an intensity of  $I = 12 kW/cm^2$  ( $\lambda = 568 nm$ ).

The determined parameters of the dye AZ174 are summarized in table 3.3 and show that

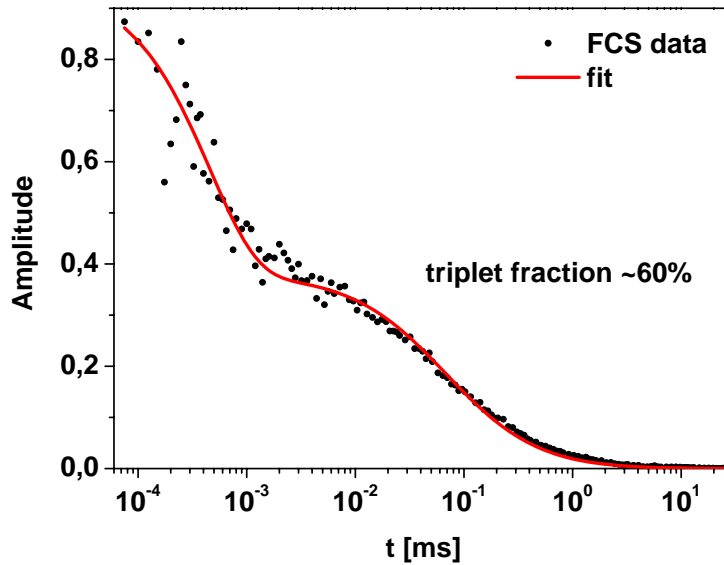


Figure 3.11: FCS measurement of AZ174 in PBS,  $I = 12 kW/cm^2$ ,  $\lambda = 568 nm$

Az174 is a good candidate for GSD microscopy in aqueous solution if one compares the parameters with the simulation results in table 3.2.

$k_{isc} [1/s]$	$k_T [1/s]$	$k_{fl} [1/s]$	$\sigma [cm^2]$
$5 \cdot 10^7$	$1 \cdot 10^6$	$5.3 \cdot 10^8$	$3.8 \cdot 10^{-16}$

Table 3.3: Determined parameters for the dye AZ174

Figure 3.12 shows the depletion curve determined by pump-probe measurements together with the fraction of molecules in the singlet state obtained from the FCS measurements. The singlet fraction was determined by analyzing the FCS curves following the analysis in [56]. Figure 3.12 also shows one simulation of the pump-probe depletion (see appendix A.1) and one of the FCS data (which is the steady state case from equation (2.12)). The pump-probe measurements were performed following the scheme in figure 3.2a with a  $3\mu s$  pump pulse and a probe length of  $100ns$  ( $100ns$  is the minimum bin size of the MCD card). The delay between the pump and the probe pulse was between  $100ns$  and  $200ns$  and could not be determined with a higher accuracy because the smallest bin size of the MCD card was limited to  $100ns$ .

Figure 3.12 shows that there is a difference in the depletion curves between the FCS and

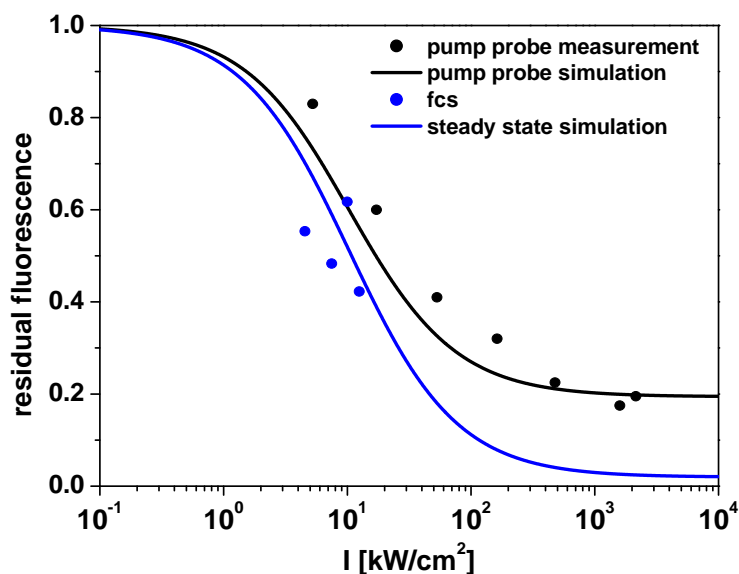


Figure 3.12: Pump-probe fluorescence depletion curve measured for AZ174 in PBS compared with simulations of steady state pumping and the used pump-probe cycle. The values from the FCS measurements points are comparable with those calculated for steady state case, probe power  $P_p = 10\mu W$  corresponding to a probe intensity  $I_p = 20kW/cm^2$ ,  $\lambda = 568nm$ .

the pump-probe measurements. The reason for this is that the FCS measurements directly reflect the steady state populations while there is a time delay between the depletion and the probe in the pump-probe measurements. The dye AZ174 has a short triplet lifetime of  $1\mu s$  and therefore some of the molecules in the triplet already relax to the ground state during the delay of  $\sim 100ns - 200ns$  between the pump and the probe. The steady state case for AZ174 was simulated for the dye parameters in table 3.3 using equation (2.12) and is in good agreement with the FCS data regarding the precision of the FCS data (see figure 3.12). The pump-probe measurements were also simulated assuming a delay of  $150ns$  between pump and probe, a probe length of  $100ns$  and a pump time of  $3\mu s$ . The simulation of the pump-probe measurements is also in good agreement with the pump-probe measurements in figure 3.12. The pump-probe simulation was performed by application of a numerical matrix algorithm in a Matlab program (see appendix A.1).

Figure 3.12 shows that for the steady state case, a maximum depletion of  $< 5\%$  is achieved

while in the pump-probe measurements only a depletion of  $\sim 20\%$  is obtained. The reason for this is that the molecules in the triplet relax back to the ground state during the delay of  $\sim 100\text{ns} - 200\text{ns}$  due to the short triplet lifetime of only  $1\mu\text{s}$ . Another problem is the short probe time of  $100\text{ns}$  which necessitates a repetition of the pump-probe cycle of  $\sim 20000$  times to collect enough signal.

In any case, the depletion measurements prove the possibility of depleting the ground state in solution with short triplet lifetimes.

### 3.3.4 Ground State Depletion Using the Heavy Atom Effect

The use of heavy atoms like bromine as substituents for the hydrogen atoms in the dye molecule can introduce a higher spin orbit coupling which results in an increased triplet yield. This heavy atom effect was investigated for several dyes with heavy atom dopants. The dyes tested are shown in figure 3.13 together with their structures, intersystem crossing rates and their maximum depletion level. The intersystem crossing rates were determined by FCS measurements or taken from the literature [50] and the depletion measurements were performed in PVA. Comparing the structures and the  $k_{isc}$  rates in figure 3.13, it turns out that doping at the side group of the fluorophore does not have a strong effect on the intersystem crossing rate (if one compares the undoped dye DR25 with the doped dyes MR71, JA4 and JA98). In contrast, the main group-doped fluorophores (EosinY and 2Br-Fluoresceine) show a strong increase of the intersystem crossing rate  $k_{isc}$  of up to two orders of magnitude. This also influences the maximum depletion levels: for EosinY, the fluorescence can be depleted as low as 5% but for the dyes doped at the side group, the maximum depletion is only 20% (JA98). Also, the number of dopants has an effect on the depletion level and the intersystem crossing rate as is shown for EosinY and 2Br-Fluoresceine. EosinY with four bromine atoms has a depletion level of 5% but 2Br-Fluoresceine with only two bromine atoms reaches a depletion level of only 10%.

The results in figure 3.13 show that the heavy atom effect can be used to engineer the intersystem crossing rate of a dye molecule. Doping at the side group has nearly no effect on the intersystem crossing rate while doping at the main group results in a strong increase of  $k_{isc}$ .

The higher spin orbit coupling also increases the triplet decay rate of the dye, but this rate is mainly determined by interactions with the environment like collisions and the presence of oxygen. Taking into account the already reduced triplet relaxation rate of the dyes in polymer films like PVA, one can consequently increase the intersystem crossing rate by using heavy atom ligands and simultaneously decrease the triplet decay rate by embedding the dye molecules in an adequate rigid matrix. Altogether, we can achieve a much higher triplet population by using these two effects and strongly reduce the saturation intensity. This was, for example, shown for EosinY in PVA.

For GSD microscopy in solution, it was demonstrated that the intersystem crossing rate is a crucial parameter. Heavy atom doping could be an interesting method for the creation of better dyes for GSD microscopy in aqueous solution because it would offer the possibility to adjust the intersystem crossing rate by the number, position and the type of the heavy atom dopant.

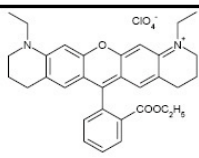
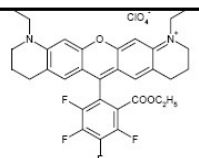
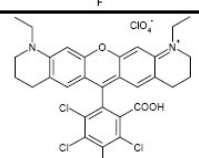
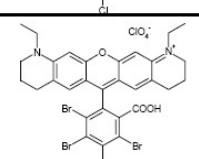
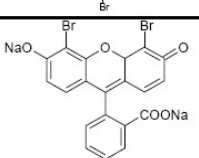
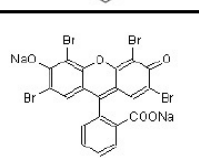
Dye	Structural formula	Depletion	$k_{isc}$ [1/s]
DR25		~30%	$1.6 \cdot 10^6$
MR71 (F)		~40%	$1.6 \cdot 10^6$
JA4 (Cl)		~23%	$1.3 \cdot 10^6$
JA98 (Br)		~20%	$3.5 \cdot 10^6$
2Br-Fluoresceine		~10%	$0.6 \cdot 10^8$
EosinY		~5%	$1.15 \cdot 10^8$

Figure 3.13: Heavy atom effect on dyes with different heavy atom dopants at different positions in the molecule. Depletion measurements were performed in PVA,  $k_{isc}$  rates for EosinY and 2Br-Fluoresceine from [50].

### 3.3.5 Summarization of All Tested Dyes

In the previous three sections, only some of the tested dyes in different environments were considered. A list of all the tested dyes with their important parameters for GSD microscopy is shown in figure 3.14. It shows that there are several dye families whose

Fluorophore	Exc. <sup>[a]</sup>	Media	Depletion <sup>[b]</sup>	Bleaching <sup>[c]</sup>	$I_{sat}$ <sup>[d]</sup>
<b>Atto-Dyes</b>					
Atto532	532	VectaShield	10 %	20 %	10
Atto565	568	VectaShield	20 %	30 %	35
		PVA	35 %	20 %	15
<b>Rhodamine-Dyes</b>					
Rhodamine 6G	532	PVA	10 %	n.d.	3
Sulfo-rhodamine 101	568	PVA	40 %	20 %	50
Thio-rhodamine (AZ174)	568	Water	<20%	n.d.	30
<b>Cyanine-Dyes</b>					
Cya-nine 3	568	VectaShield	25 %	50 %	35
<b>Alexa-Dyes</b>					
Alexa594	568	VectaShield	15 %	30 %	15
		PVA	20 %	20 %	15
<b>Fluorescein-Dyes</b>					
Carboxy-naphto-	568	VectaShield	25 %	35 %	15
Phloxin B	532	PVA	10 %	n.d.	0.15
2-Bromo-Fluorescein	532	PVA	10 %	n.d.	0.3
Eosin Y (4-Bromo-)	532	PVA	5 %	n.d.	0.02
<b>Bodipy-Dyes</b>					
BODIPY 577 / 618	568	VectaShield	60 %	40 %	65
<b>Perylene-Dyes</b>					
KP-168	532	VectaShield	10 %	n.d.	10
<b>Other Dyes</b>					
DR25	568	PVA	30%	n.d.	23
MR71(F-doped)	568	PVA	40%	n.d.	51
JA4(Cl-doped)	568	PVA	23%	n.d.	6.1
JA98(Br-doped)	568	PVA	20%	n.d.	6.6

Figure 3.14: [a] Excitation wavelength in nm. [b] Depletion of fluorescence due to optical shelving: Maximum residual fluorescence after depletion. [c] Fraction of molecules bleached after 25 depletion-probe cycles at a depletion intensity  $I_D > 5 I_{sat}$  (saturation depletion intensity). [d] Saturation intensity in  $kW/cm^2$ , depletes 50% of the fluorescence, n.d.: Not determined, structural formulae of the dyes in appendix (see figure A.5).

fluorescence can be depleted by pumping into the triplet state.

The most effective pumping parameters were found for PVA and Vectashield as the embedding media. The reason for this is the small triplet relaxation rate and the reduction of oxygen presence which also results in reduced bleaching. Reducing the depletion intensities and bleaching rates makes these environmental conditions favourable for GSD imaging.

The results for AZ174 demonstrate that it is possible to deplete the fluorescence in aqueous solutions with short triplet lifetimes.

Also the effect of doping the dye molecules with heavy atoms was tested. It was demonstrated that by employing the heavy atom effect, it is possible to engineer the intersystem crossing rate by the number, position and the type of the heavy atom dopant introduced into the dye molecule.

In PVA, commonly used dyes for immunolabelling like Rhodamine 6G (Rh6G), Alexa594, Fluoresceine dyes and Attotec dyes were tested and showed a strong depletion effect.

It is important to note that some dyes in PVA form long-lived reversible radical states which are usually populated via the triplet state [57]. The existence of two dark states

with two different decay times leads to an overall fluorescence relaxation after dark state population of sometimes several hundred milliseconds. An example for this behaviour is Rh6G in PVA where such an additional dark state has been described in the literature [57]. The fluorescence depletion curve of Rh6G in PVA is shown in figure 3.15.

Several commonly used dyes in immunolabelling like Cyanine, Fluoresceine, Attotec

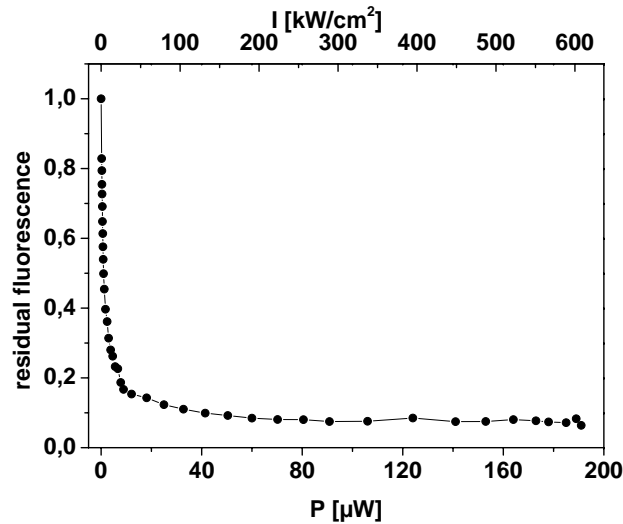


Figure 3.15: GSD Depletion curve of Rh6G in PVA

and Alexa dyes were tested in Vectashield and showed a strong depletion effect. As an example, the fluorescence depletion curve of Alexa594 in Vectashield is shown in figure 3.16.

Alltogether, the depletion experiments demonstrate that there are several common dyes

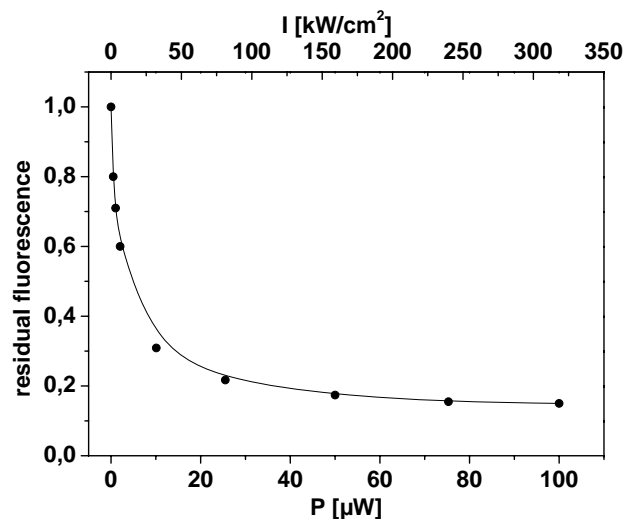


Figure 3.16: GSD Depletion curve of Alexa594 in Vectashield

whose fluorescence can sufficiently be depleted by pumping into the triplet state or another dark state and thereby show the generality of the GSD concept. It was also shown that the ground state can be depleted in different environments like PVA, Vectashield and aqueous solution.

## 3.4 GSD Imaging

### 3.4.1 GSD Imaging in PVA

#### GSD Imaging of EosinY Stained Structures

The performance of sub-diffraction GSD imaging was first tested on Eosin Y stained structures. These structures featured parallel grooves in glass slides produced by focused ion beam milling (Fraunhofer Institute IISB, Erlangen, Germany) that were  $10\ \mu\text{m}$  long,  $0.5 - 1\ \mu\text{m}$  deep,  $100 - 150\text{nm}$  wide and  $200 - 300\text{nm}$  in distance (see figure 3.17c). The

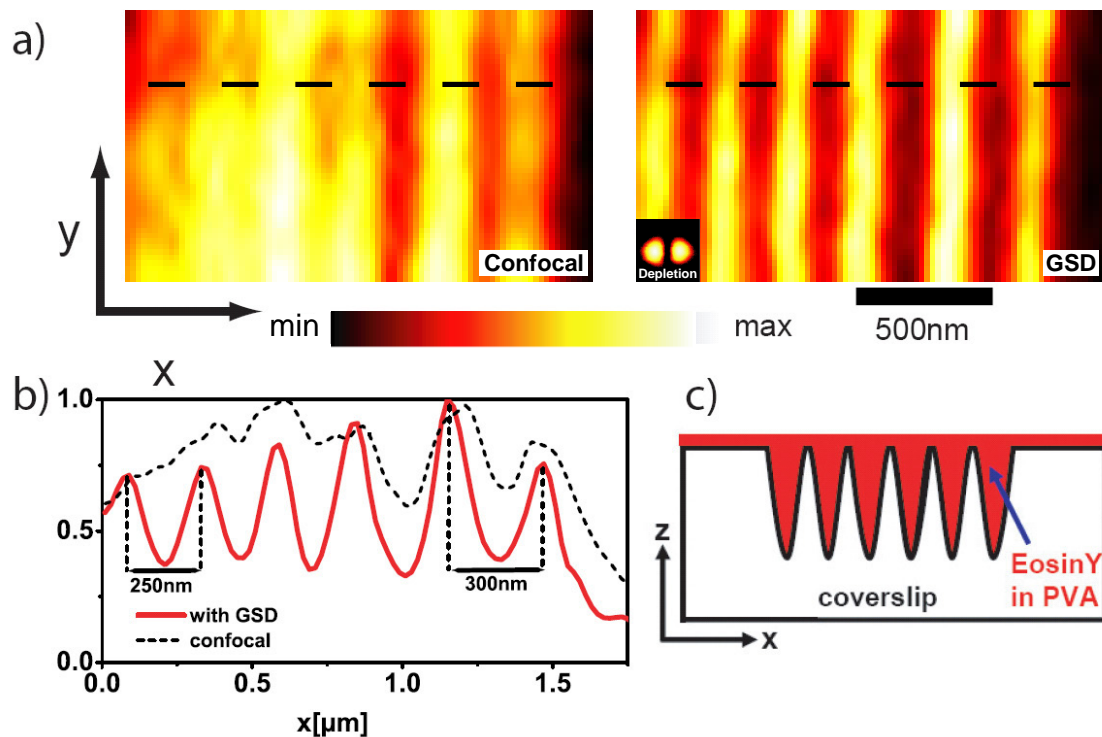


Figure 3.17: a) Confocal and GSD image of EosinY/PVA stained glass structures (maximum depletion intensity  $I_D = 1.4\text{kW}/\text{cm}^2$ , probe intensity  $I_p = 1.6\text{kW}/\text{cm}^2$ ). The depletion PSF is shown in the bottom left of the GSD image and was generated by the halfmoon phase mask. b) The linescan along the dashed line in a) reveals the improvement by GSD microscopy. c) Principle drawing of the structures.

distance of the grooves were chosen to be close the diffraction limit. Staining of the glass structures was performed by spin-coating  $1\ \mu\text{M}$  EosinY in PVA, making up a layer of  $200\text{nm}$ . As a consequence, in fluorescence microscopy the staining makes the grooves visible as bright lines. The structures were imaged with conventionally diffraction-limited confocal microscopy and with GSD microscopy featuring a depletion beam generated by the halfmoon phase mask, hence the effect of resolution enhancement was along the x-direction only. Figure 3.17a displays an image of the same region of the sample that was consecutively recorded with common confocal (left panel) and with GSD microscopy

(right panel). The images were recorded with a pixel size of  $40\text{nm}$  along  $x$  and  $100\text{nm}$  along  $y$  and were smoothed using a Lagrangian interpolation of third order. Comparison of the images confirms a significantly improved resolution along the  $x$ -axis for the GSD image. The improvement becomes even more visible in the line profiles of figure 3.17b. The application of GSD clearly reveals grooves at  $250\text{nm}$  center-to-center distance (solid line) not resolvable with conventional diffraction-limited confocal microscopy (dotted line). With a groove-widths of  $100 - 150\text{nm}$  such center-to-center distance verifies resolution capabilities of structures  $\sim 100\text{nm}$  apart for GSD microscopy which could not be resolved in the diffraction-limited confocal image.

The applied maximum depletion intensity was  $I_D = 1.4\text{kW}/\text{cm}^2$  and the probe intensity  $I_p = 1.6\text{kW}/\text{cm}^2$  was the same as in the depletion curve measurements (see figure 3.3). The integration time used for the confocal and the GSD image was  $20\mu\text{s}$  as found best from the depletion measurements of EosinY in PVA (see figure 3.3). However, the fluorescence signal gathered during  $20\mu\text{s}$  of the probe pulse is rather low and sufficient signal-to-noise levels necessitate integration over 50-fold iteration of the pump-probe cycle, resulting in rather long acquisition times of  $500\text{ms}$  per pixel.

### **GSD Imaging of $80\text{nm}$ EosinY Stained Fluorescent Beads**

Samples commonly used for high resolution microscopy are sub-diffraction sized beads stained with fluorescent markers. For this purpose, silica beads of  $80\text{nm}$  in diameter were stained with Eosin Y (Eosin-5-isothiocyanate, Molecular Probes, Eugene, OR) following a two-step protocol [58, 59, 60, 61] (see appendix A.3 for preparation). An about  $1\mu\text{m}$  thick PVA layer was spin-coated on top of the beads dried on the microscope cover glass to protect the beads from oxygen.

Sub-diffraction GSD images of the Eosin Y stained silica beads were performed and are shown in figure 3.18a. The depletion PSF was generated by the halfmoon phase mask, hence the resolution enhancement is along the  $x$ -direction only. The images were recorded with a pixel size of  $40\text{nm}$  along  $x$  and  $100\text{nm}$  along  $y$  and were smoothed using a Lagrangian interpolation of third order. The linescan in 3.18b) points out the resolution enhancement of GSD were beads in a distance of  $200\text{nm}$  can be resolved. Taking into account the bead size of  $80\text{nm}$  this is clearly below the diffraction-limited resolution capabilities.

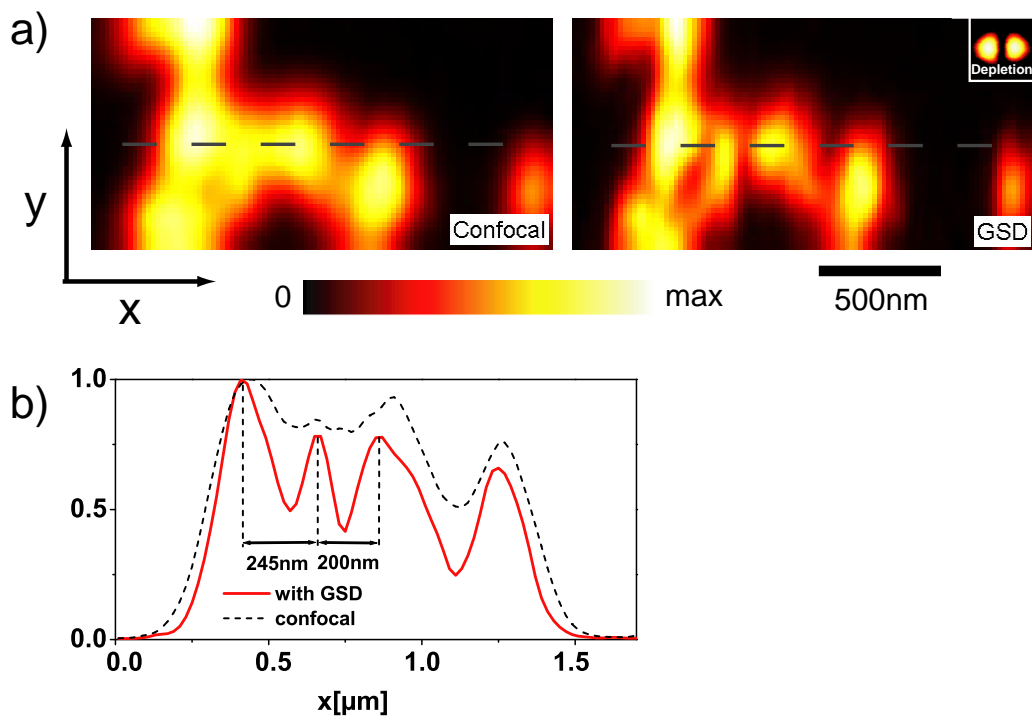


Figure 3.18: a) Confocal and GSD image of 80nm EosinY silica beads in PVA (maximum depletion intensity  $I_D = 1.4\text{kW}/\text{cm}^2$ , probe intensity  $I_p = 1.6\text{kW}/\text{cm}^2$ ). The depletion PSF is shown in the top right of the GSD image and was generated by the halfmoon phase mask b) The linescan shows a clear improvement for GSD.

## Resolution Determination by GSD Imaging of 80nm EosinY Stained Fluorescent Beads

Since the diameter of the 80nm EosinY stained silica beads is much smaller than the confocal resolution of  $\sim 200nm$  they can be used to determine the resolution of the GSD microscope. The measured fluorescence depletion curve of the EosinY stained beads is shown in figure 3.19. The saturated depletion level of 10% and the saturation intensity of  $I_{sat} = 30W/cm^2$  are slightly higher than for EosinY in PVA (see figure 3.3). The reason for that could be the changed environment of the dye molecules which are embedded in the silica instead of PVA as before.

To determine the resolution sub-diffraction scanning fluorescence images of single

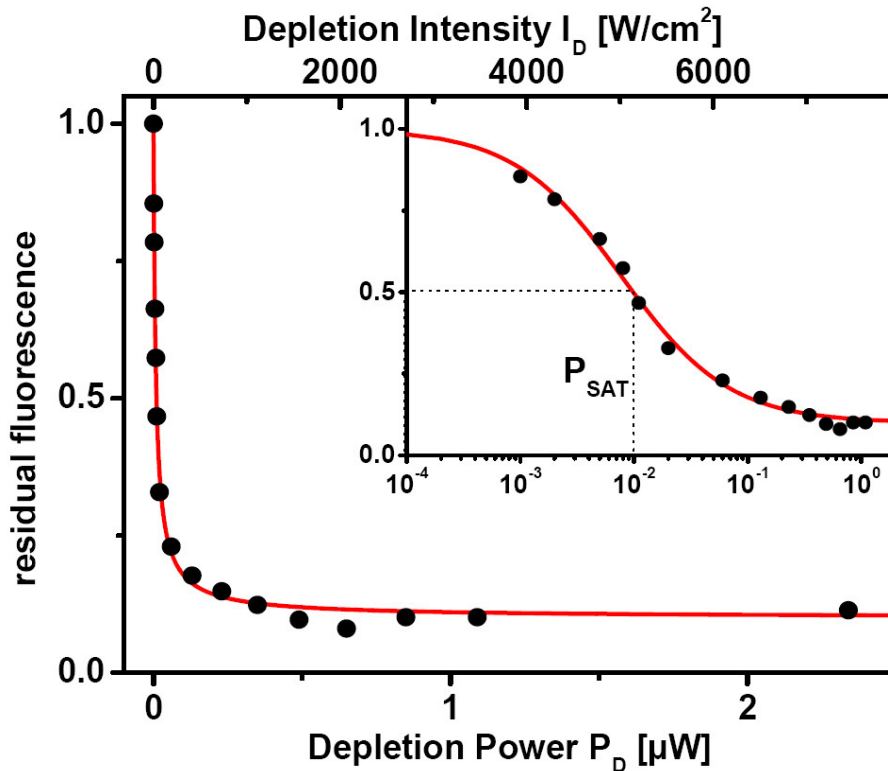


Figure 3.19: Fluorescence depletion curve of EosinY beads in PVA. The logarithmic inset shows the plot for small depletion powers. Saturation power  $P_{sat} = 10nW$  corresponding to a saturation intensity of  $I_{sat} = 30W/cm^2$ , probe power  $P_p = 500nW$  corresponding to a probe intensity of  $I_p = 1.6kW/cm^2$ ,  $\lambda = 532nm$ .

EosinY-stained silica beads were accomplished, as shown by the corresponding linescans along the lateral x-axis (see figure 3.20a). The pump pulse intensity maximum was  $I_D = 1.3kW/cm^2$  and the probe intensity was  $I_p = 1.6kW/cm^2$ . The GSD line scan in figure 3.20a shows a reduction of the FWHM down to 97nm from 220nm for the confocal linescan. The effective PSF (FWHM=60nm) was calculated using the fluorescence depletion curve from figure 3.19 and convolved with the 80nm sized bead to simulate the GSD linescan. The resulting simulated GSD linescan is shown in figure 3.20a and is in good agreement with the GSD measurement. The resolution is given by the FWHM of  $\sim 60nm$  of the effective PSF and smaller than the measured FWHM of 98nm in the GSD linescan.

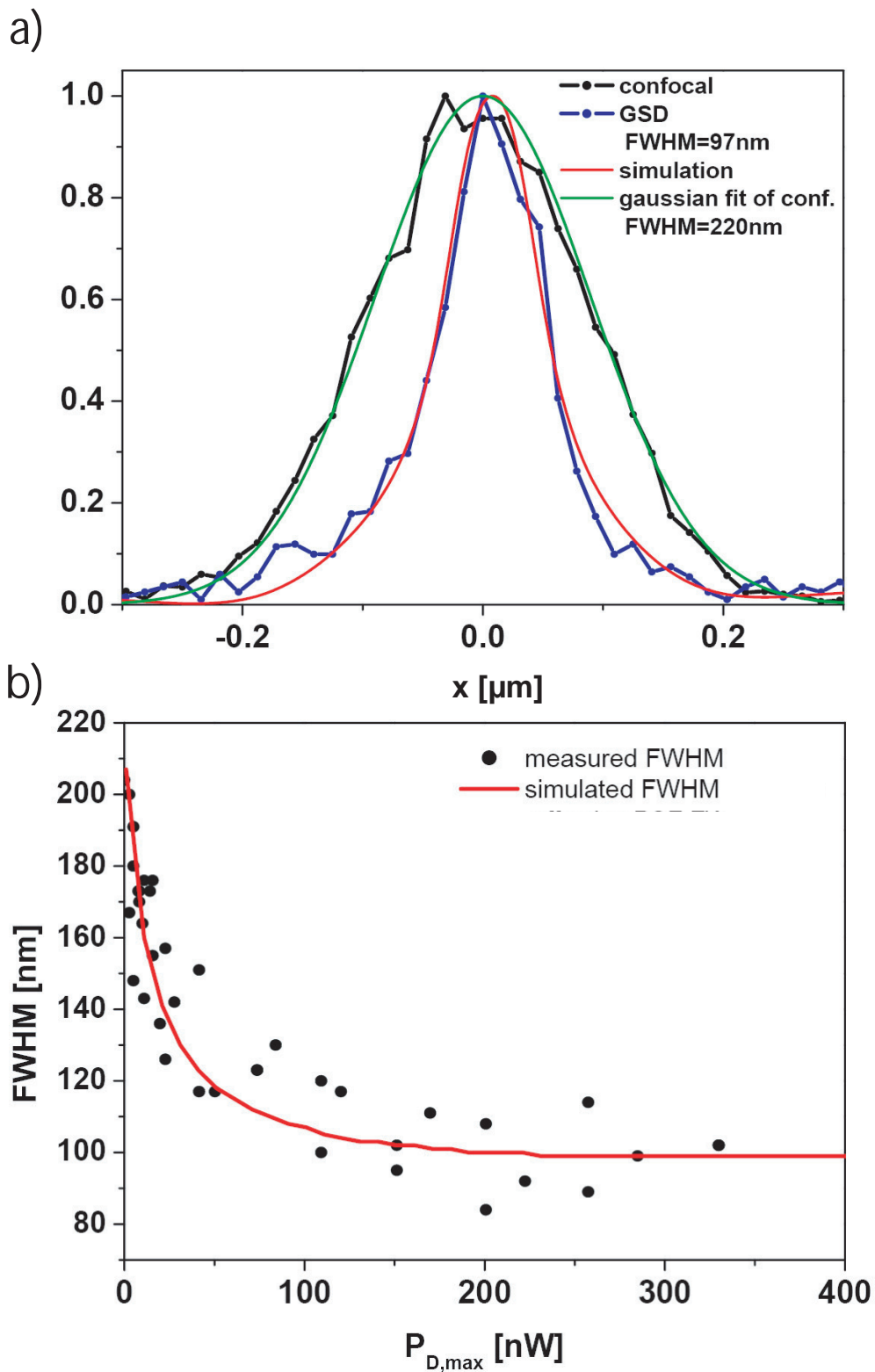


Figure 3.20: a) Linescan of  $80\text{nm}$  beads performed by GSD (FWHM of  $97\text{nm}$ ) and confocal microscopy (FWHM= $220\text{nm}$ ). The simulation of the GSD linescan was calculated from the fluorescence depletion curve in figure 3.19 by convolving the calculated effective PSF with the  $80\text{nm}$  bead. Scanning step size along  $x$ :  $15\text{nm}$ . b) Measured GSD FWHM values for different depletion powers.

The reason for that is that the effective PSF has to be convolved with the  $80\text{nm}$  sized bead. Figure 3.20b shows the measured FWHM of single bead linescans against the depletion power. Increasing the depletion power reduces the FWHM in the GSD linescans and saturates at an average FWHM of  $100\text{nm}$ . In comparison with the depletion curve of the EosinY beads in figure 3.19 this plot shows that the effect of resolution enhancement really stems from the fluorescent depletion by the depletion PSF. By increasing the depletion intensity the fluorescence is more and more confined to the intensity zero of the donut and thereby the resolution is enhanced. The red curve in Figure 3.20b was calculated<sup>1</sup> with the fluorescence depletion curve of figure 3.19 and describes the experimental measured FWHM values.

---

<sup>1</sup>A correction factor of two had to be applied to the power of the measured FWHM data to achieve a good agreement with the theory. The reason for that is that the depletion curve was the basis for the calculation of the effective fluorescence spot and the depletion curve was not measured on the same day like the FWHM values. An imprecise power measurement could therefore explain this correction factor due to the fact that the power measurements in the range of 1 to 50nW are not very precise.

### 3.4.2 GSD Imaging in Vectashield

#### GSD Imaging of 40 nm beads

For demonstration of sub-diffraction resolution in Vectashield a sample with 40nm diameter beads (40nm orange beads (540/560)), Molecular Probes, Eugene, OR) was imaged with the donut shaped depletion PSF in order to obtain resolution enhancement in all lateral directions. The beads were attached to a microscope cover slip using poly-L-lysine and covered with Vectashield (see appendix A.3). Figure 3.21 shows images comparing confocal and GSD microscopy. Both images were subject to a single-step linear deconvolution for fair comparison. The scanning step size was 25nm along the x and the y directions with a pixel dwell time of 60ms. While being blurred in the diffraction-limited confocal image, GSD microscopy separates the beads in all directions. The intensity maximum of the depletion PSF was  $I_D^{max} = 80kW/cm^2$ , the excitation wavelength was 532nm.

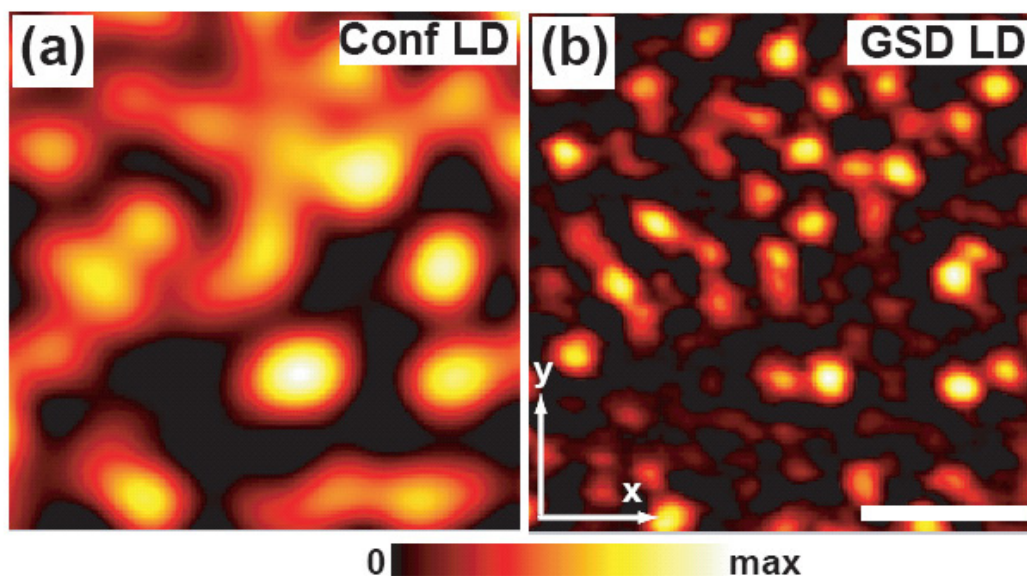


Figure 3.21: GSD microscopy provides super-resolution in the focal plane. 40nm orange fluorescent beads recorded confocally (a) and with GSD (b). Both images after linear deconvolution (LD) with the theoretical calculated PSF (see next section), scale bar=500 nm.

#### Resolution determination by imaging of 40 nm beads

As a simple probe of the resolution the 40nm beads were used in a very low concentration so that it was possible to image completely isolated beads. Since the 40nm diameter of the beads is well below the diffraction limit the size of the beads in the GSD images can be used to determine the resolution. The single beads images were recorded using the donut shaped depletion beam with a power of 80μW (corresponding to  $I_D^{max} = 80kW/cm^2$ ) and a scanning step size of 25nm.

The resolution was first calculated from the fluorescence depletion curve of the 40nm orange beads. Figure 3.22 shows the fluorescence depletion curve measured on single beads using the same power and pulse sequence as for the Atto532 antibodies in Vectashield (see figure 3.9). The depletion intensity  $I_D = 10kW/cm^2$ , where half the fluorescence is depleted, is nearly the same as for the Atto532 antibodies (see figure 3.9), but the saturation depletion level is only around 17% compared to <10% in the antibody case. By using

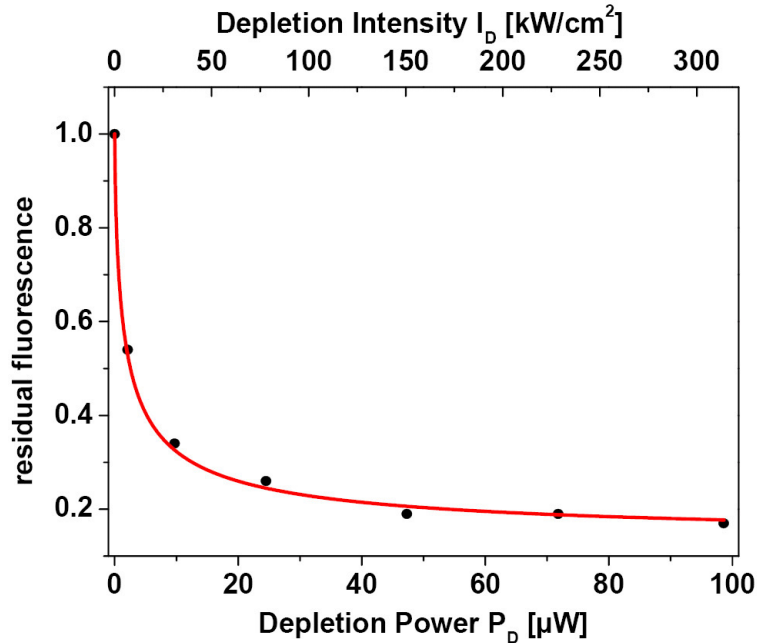


Figure 3.22: Fluorescence depletion curve measurement of 40nm orange beads in Vectashield. The depletion was measured on single beads in the center of the PSF, pump length was  $500\mu s$ , probe length  $100\mu s$ , probe intensity  $I_P = 7kW/cm^2$ .

the experimentally determined depletion together with the depletion curve from figure 3.22 donut one can calculate the effective PSF. The resulting effective PSF with a FWHM of  $100nm$  is shown in figure 3.23a and has to be convoluted with the xy-projection of the 40nm fluorescent bead to calculate its GSD image with a slightly increased FWHM of  $112nm$ . For comparison of the calculated with the experimental single bead image, images of about 20 beads have been centered and added up to obtain an average experimental single bead image (see 3.23a). Figure 3.23b shows the linescans for the calculated single bead image and the average measured single bead image. The calculated FWHM of the bead image of  $112nm$  agrees well with the measured FWHM of  $107nm$  and also the shape of the linescans looks quite similar. Therefore these results prove that it is possible to calculate the theoretical effective PSF from the experimental depletion curve and that the results agree quite well with the experimental determined images. The theoretical calculated PSFs can therefore be used to deconvolve the measured GSD images as it was already done for the 40nm bead images in figure 3.21.

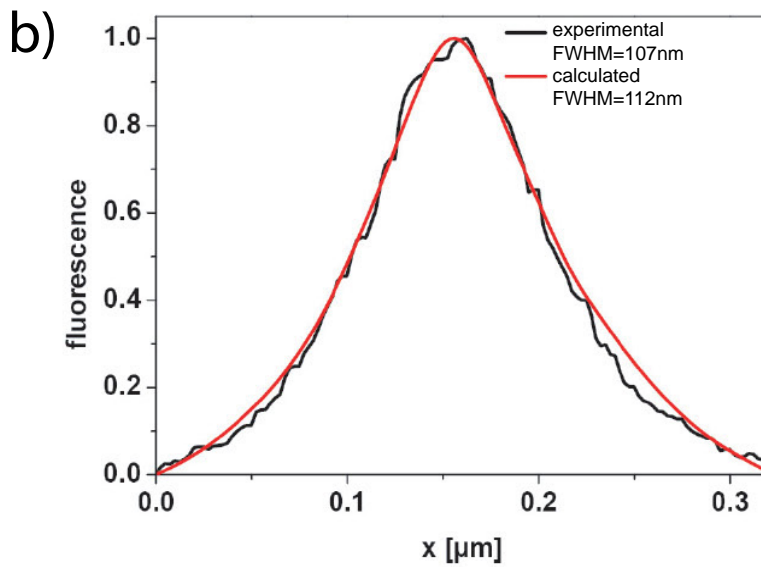
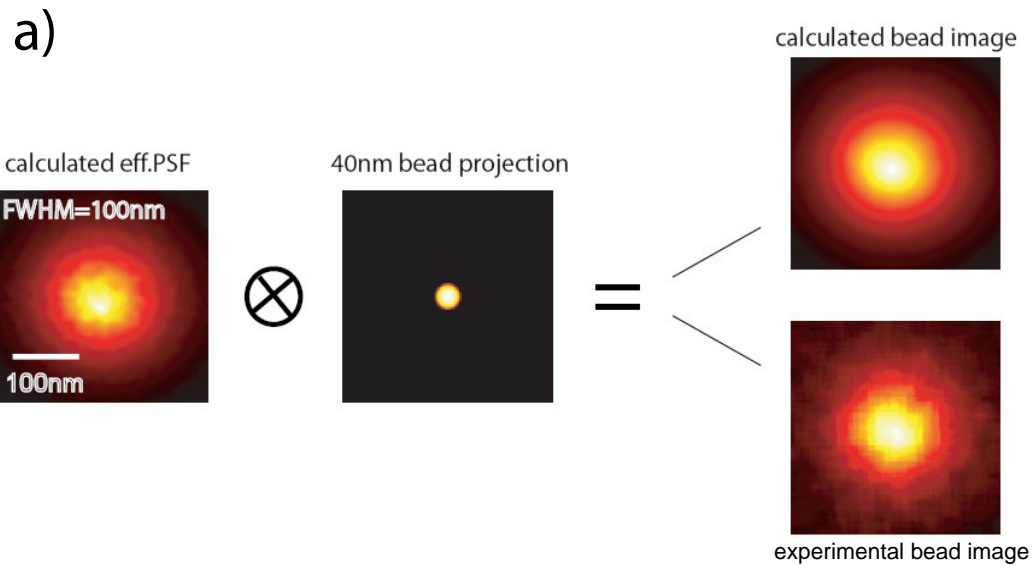


Figure 3.23: a) Calculated effective PSF convoluted with the xy-projection of the 40nm bead results in the calculated GSD single bead image which is compared with the experimental GSD image averaged over 20 single beads. b) The shape and the FWHM of the simulated and measured linescan agree quite well which confirms the correctness of the calculated data.

## Imaging of biological samples

Since it was shown for the 40nm fluorescent beads the calculated PSFs can well simulate the experimental measurements, such calculation can also be done for applications in biological samples. Therefore the effective PSFs were calculated from the fluorescence depletion curve of single Atto532 antibodies in figure 3.9 once for the helical phase ramp (depleting the fluorescence in all lateral directions) and once for the halfmoon phase mask (depleting the fluorescence only in the x-direction). The in this way calculated effective PSFs are presented in figure 3.24. The powers used in the simulations were the same as in the measurements. While providing an improved resolution along all lateral directions,

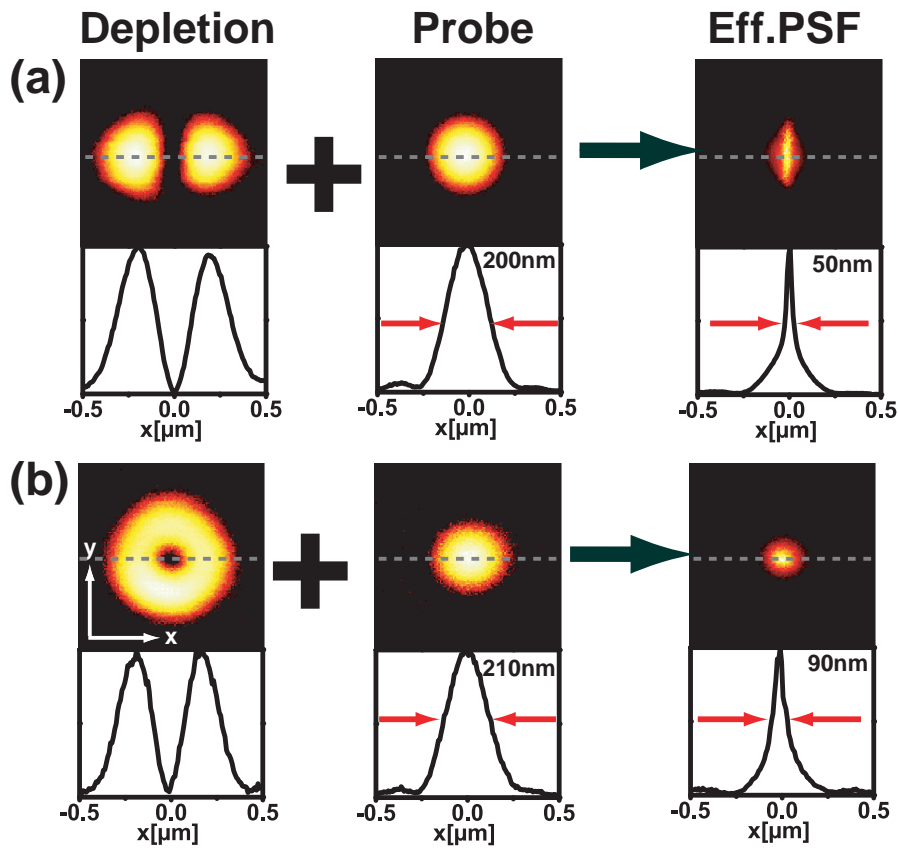


Figure 3.24: Creating effective PSFs of sub-diffraction extent in a GSD microscope. (a) Squeezing the spot just along the x axis and (b) along all directions in the focal plane. The depletion spot (Depletion) overlaid with the regularly focused probe spot (Probe) produces the effective PSF (Eff. PSF). The probe spot probes the fluorescence right after the depletion spot has pumped the dye into the  $T_1$ . Focal plane cross section of the PSF (upper panel) and profiles along the x axis [dashed line in upper panels] showing FWHM values (lower panels), wavelengths for depletion and probing: 532nm; fluorescence wavelength: 560nm.

the donut necessitates more scanning steps and therefore causes more bleaching than the depletion PSF generated by the halfmoon phase pattern. Consequently, to avoid increased photobleaching, only  $I_D^{max} = 80 \text{ kW/cm}^2$  were applied in the donut case as compared to  $I_D^{max} = 350 \text{ kW/cm}^2$  for the halfmoon. The  $I_D^{max}/I_S = 35$  for the halfmoon and  $I_D^{max}/I_S = 8$

for the donut rendered 50 and 90nm FWHM, respectively. These FWHM values are slightly larger than those expected from Eq. 2.9, which is due to adverse effects such as imperfections of the zero. In any case, the effective PSF is up to 4 times smaller than that of the confocal PSF resulting from the probe spot.

Figure 3.25 shows confocal and GSD images of the microtubular network of a human embryonic kidney cell, in the case of GSD recorded with the halfmoon depletion PSF of figure 3.24a. The microtubules were labeled with Atto532-stained antibodies and the cell

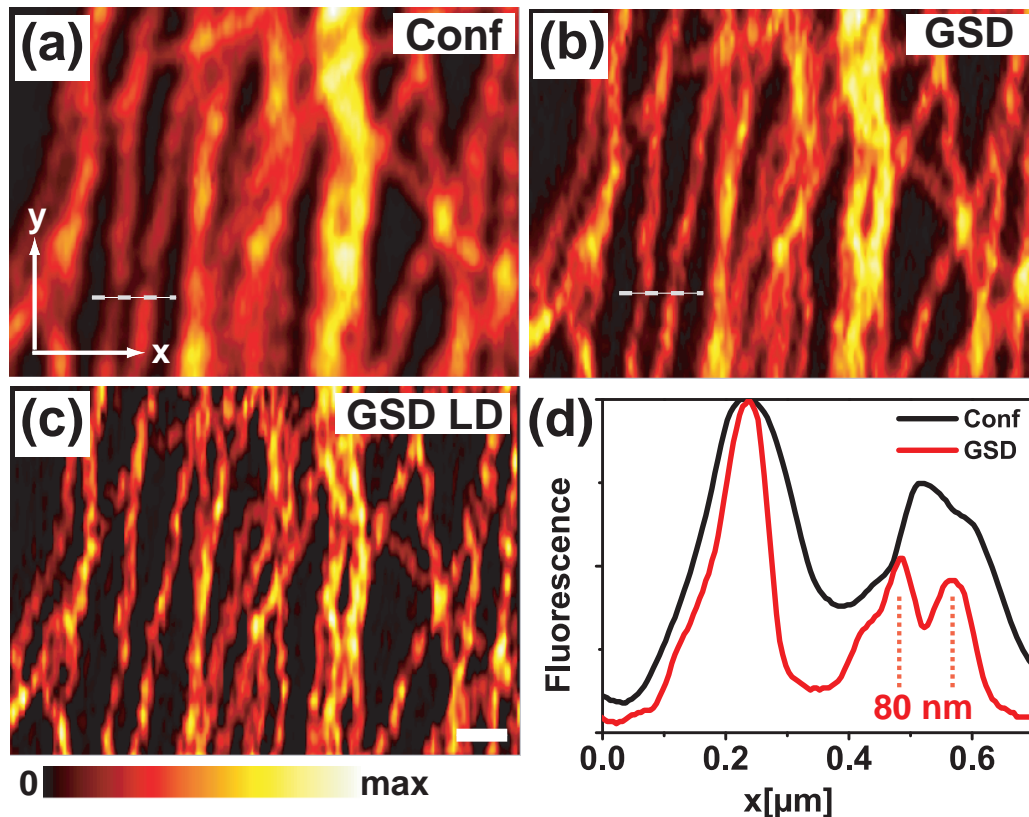


Figure 3.25: GSD microscopy provides focal plane resolution of 80 nm in biological imaging, demonstrated with Atto532-stained microtubules: (a) confocal, (b) GSD, and (c) GSD plus linear deconvolution (LD). (d) Normalized line profiles through the data of (a) and (b) where indicated by the dashed line; images were smoothed using a Lagrangian interpolation of third order. Scale bar= 500nm.

was mounted with Vectashield. The images were recorded with a pixel size of 33nm along x and 100nm along y and a pixel dwell time of 60ms. The raw data of the GSD recording (3.25b) resolves features of the network along the x axis that are hidden in the confocal reference image. This is further highlighted in the line profiles of figure 3.25d, where microtubular strands at distances of 80nm can be resolved by GSD but not by confocal microscopy. The dynamics of triplet state saturation, in particular the incomplete  $S_0$  depletion (figure 3.9a, lead to PSFs with a sharp tip and a broader baseline (3.24) implying that in addition to the super-resolution spatial frequencies, the raw GSD data contains a substantial amount of low frequencies. Applying a single-step linear deconvolution (e.g., a Wiener filter) enhances the high frequency content in the image and hence the structural

details (figure 3.25c).

The image pair of figure 3.26a and 3.26b) demonstrates that the sub-diffraction resolution in both lateral directions can also be obtained in biological imaging. Figures 3.26a

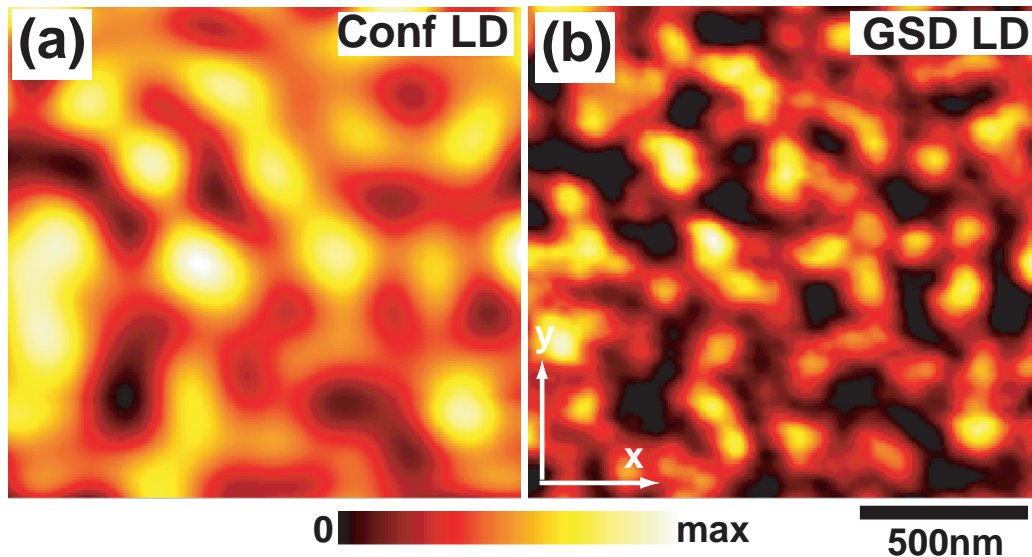


Figure 3.26: GSD microscopy provides super-resolution in the focal plane. SNAP-25 protein agglomerations stained with Atto532 on a cell membrane: confocal (a) and GSD (b), all images after linear deconvolution (LD).

and 3.26b) visualize the spatial distribution of Atto532-labeled SNAP-25 proteins on the plasma membrane of a fixed neuronal cell mounted in Vectashield. As a part of the SNARE family, the protein SNAP-25 codetermines the plasma membrane site at which a vesicle may dock or fuse. Again, the GSD image exhibits a much more detailed view of the protein spatial order than in confocal microscopy. The scanning step size was 25 nm along the x and the y directions and a pixel dwell time of 60ms was used.

### 3.4.3 GSD Imaging in Aqueous Solution

Expansion of GSD imaging in solution could pave the way to sub-diffraction live-cell imaging. Therefore GSD imaging was also performed in solution. One problem that arises for imaging biological samples in solution is photobleaching due to the strong necessary depletion powers (see section 3.3.3). Another approach was chosen to demonstrate the capability of GSD imaging in aqueous solvents. The already used glass structures were mounted with a  $1\mu\text{M}$  PBS (pH 7.5) solution of AZ174 dye. The structures could then be imaged with GSD. The pulse sequence was the same as used in the depletion measurements in figure 3.12, a  $3\mu\text{s}$  depletion pulse (employing the halfmoon donut) was followed by a  $100\text{ns}$  confocal probe pulse (the total length of the pulse sequence was  $25.5\mu\text{s}$  due to the smallest number of bins of 255 of the MCD Card).

Of course, bleaching also plays a role in this case of GSD imaging, but due to the diffusion of new dye molecules into the imaging volume photodestruction of dye molecules becomes a negligible effect. Also, bleaching is not as strong that a notable photodestruction occurs during the  $3\mu\text{s}$  pump pulse so that the depletion effect mainly stems from pumping into the dark triplet. This can be proven by the FCS data shown in section 3.3.3. One parameter determined in FCS is the diffusion time of the dye molecules through the focus, which is usually  $\sim 50\mu\text{s}$ . If there was a strong bleaching, the diffusion time in FCS would be reduced because the dye molecules would bleach away during their detention time in the focus (the time constant one obtains in that case from FCS is the observation time before photodestruction). Such a reduction of the measured diffusion time in FCS was not observed, thus, photodestruction during one pump pulse ( $\sim 3\mu\text{s}$ ) is negligible.

For signal reasons the pump-probe pulse sequence had to be repeated 20000 times on one pixel. The reason for that is the short probe pulse of only  $100\text{ns}$ , which is required because of the short triplet lifetime and results in a very small signal obtained during one pump-probe-cycle. The in this way formed scanning images of the structures are shown in figure 3.27. The enhancement in resolution is highlighted in the linescan where one can resolve the single grooves in the GSD image better than in the confocal one. Altogether, this is the first proof that GSD imaging works in principal also in solution.

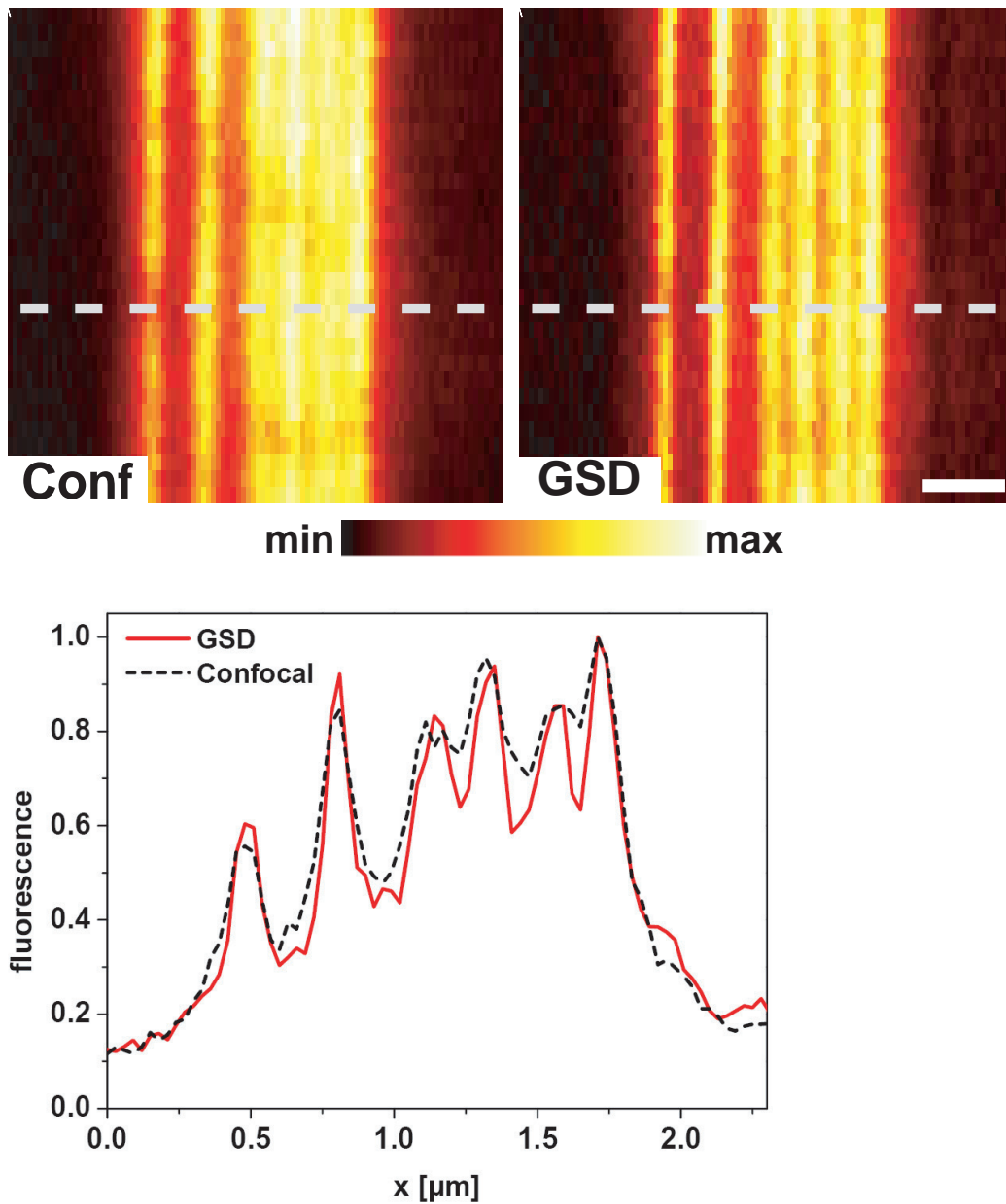


Figure 3.27: GSD and confocal image of glass structures (see 3.17d for image) with AZ174 in solution (employing the halfmoon donut). The linescan highlights the resolution enhancement in the GSD image,  $\lambda = 561nm$ , pixel step size:  $x=30nm$ ,  $y=100nm$ ,  $I_D^{max} = 300kW/cm^2$ ,  $I_p = 20kW/cm^2$ , scalebar= $500nm$ .

## 3.5 Problems and Improvements

The obtained results of GSD microscopy were limited for several reasons which will be discussed in more detail along with proposals for improvements.

### Incomplete Fluorescence Depletion and Imperfect Zero of the Depletion Focus

Two limiting factors are the incomplete depletion of the fluorescence by optical shelving and the imperfect zero intensity in the center of the depletion focus (for a more detailed discussion see for example [16]).

Three cases have to be considered:

- In the first case, a complete depletion and an imperfect zero of the depletion PSF is assumed. Here, the imperfect zero of the depletion PSF also reduces the fluorescence in the center. Hence the maximum of the sub-diffraction PSF is decreased leading to a bad signal to noise ratio and potentially deteriorating the resolution.
- In the second case, an incomplete depletion with a perfect zero of the depletion PSF is assumed. For a minimum residual fluorescence of for example 10% the resolution is not reduced in this case. The incomplete depletion just leaves a small contribution of the diffraction-limited PSF, which could for example be removed by deconvolution. But a problem arises for minimum residual fluorescence values of for example  $\sim 30\%$ , because in that case the effective sub-diffraction PSF would still contain a large fraction of the diffraction-limited PSF. In the case of a bad signal to noise ratio it may be difficult to deconvolute the image and obtain the full possible resolution.
- In the third case, both an incomplete depletion and an imperfect zero of the depletion PSF is assumed, which corresponds best to the experimental situation. Here, the sub-diffraction PSF contains a part of the diffraction-limited PSF, due to the incomplete depletion, but also the peak of the sub-diffraction PSF is reduced by the incomplete zero of the depletion PSF. Taking both effects into account leads to an even more deteriorated resolution than in the first two cases.

The effect of an imperfect zero and incomplete depletion of the fluorescence is demonstrated for GSD imaging of Atto532 labeled samples in figure 3.28a and 3.28b. The plot shows the calculated FWHM values (black curves) of the effective PSFs for the donut and the halfmoon depletion PSFs. The PSFs were calculated using the measured depletion and probe spots and the measured fluorescence depletion curve (see figure 3.9 and figure 3.24). The grey curves show the calculated effective PSFs according to the RESOLFT theory using equation (2.9).

In figure 3.28 the FWHM values calculated from equation (2.9) are smaller than the FWHM values determined from the measured PSFs and fluorescence depletion curve. The reason for that is that the curve calculated with equation (2.9) assumes a perfect depletion and a perfect zero of the depletion focus. In the experiments performed with the Atto532 antibodies neither of the two assumptions is true. The fluorescence depletion curve in figure 3.9 shows a minimum of 10% and the zero of the experimental depletion PSFs was  $\sim 1\%$  for the halfmoon and  $\sim 2\%$  for the donut. Therefore, the achievable res-

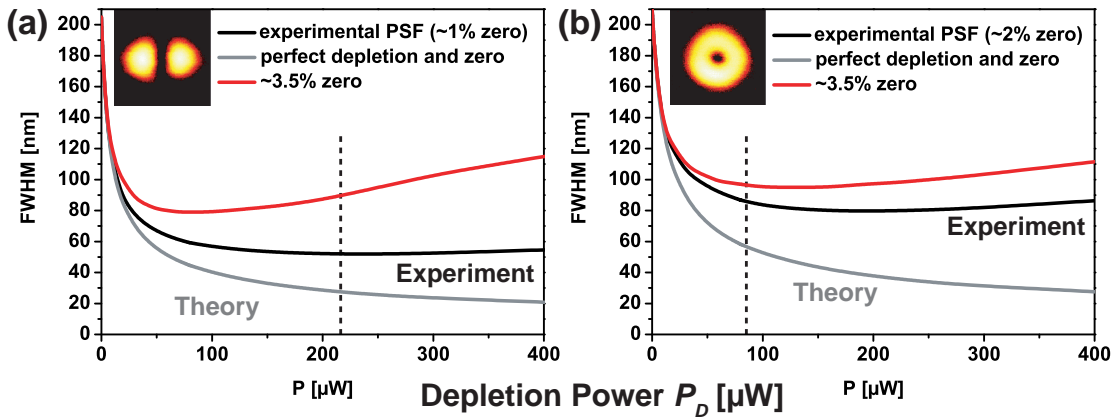


Figure 3.28: Dependence of the FWHM of the sub-diffraction effective PSF on the depletion intensity for (a) the halfmoon and (b) the doughnut-shaped depletion PSF. The PSFs were calculated (black line, Experiment) using the measured depletion and probe spots (see figure 3.9 and figure 3.24) or calculated (grey line, Theory) using equation (2.9). The experimental data displays a maximum resolution of  $50\text{nm}$  in (a) and  $80\text{nm}$  in (b). The FWHM derived from the experimental data is larger than the pure calculation according to equation (2.9). This stems from the imperfect zero of the depletion PSF and the noncomplete fluorescence depletion. The resolution is even more reduced for high depletion powers, if a zero of  $\sim 3.5\%$  (red curve) with the incomplete depletion is assumed.

olution is not as good as in theory, since the imperfect zero also depletes the fluorescence in the center of the focus while the incomplete fluorescence depletion leaves a still sub-diffraction part in the effective PSF. In the case of the halfmoon the minimum resolution rises from  $20\text{nm}$  minimum to  $50\text{nm}$  for the experimental depletion PSF (see figure 3.28a). Calculating the resolution for an incomplete depletion and an even worse zero of  $3.5\%$  leads to a minimum resolution of only  $80\text{nm}$  (red curve). In this case, the zero strongly depletes fluorescence in the center. Thus, the FWHM is rising again for high depletion powers. In the case of the donut (see figure 3.28b), the minimum resolution rises from  $30\text{nm}$  for the perfect depletion and zero to  $80\text{nm}$  for the experimental measured depletion PSF, up to  $90\text{nm}$  for the depletion PSF with a  $3.5\%$  zero and incomplete depletion. Again, the zero of  $3.5\%$  leads to an increase of the FWHM values for higher depletion powers. The vertical dashed lines in figure 3.28 represent the optimal experimental conditions implemented in the actual GSD imaging examples. For the halfmoon depletion donut in figure 3.28a the experimental depletion power was  $220\mu\text{W}$  ( $I_D^{\text{max}} = 350\text{kW}/\text{cm}^2$ ) where a experimentally optimal resolution of  $50\text{nm}$  was achieved. For the donut shaped depletion beam (figure 3.28b) the maximum achievable resolution was  $80\text{nm}$ , but the experimental conditions only allowed to apply a depletion power of  $80\mu\text{W}$  ( $I_D^{\text{max}} = 80\text{kW}/\text{cm}^2$ ) and therefore to achieve a resolution of only  $90\text{nm}$ . The reason for that is that the donut brings resolution enhancement along all lateral directions and therefore necessitates more scanning steps than the halfmoon. Hence, bleaching is increased. The experimental optimal resolution was therefore  $90\text{nm}$  and established a good compromise between applied power, photobleaching and resolution gain. This example clearly shows the strong effect of an imperfect zero of the depletion beam and the incomplete fluorescence depletion on the achievable resolution and offers therefore a good starting point to improve GSD microscopy.

One could use adaptive optics to correct aberrations in the depletion beam but also aberrations arising from the sample itself (for example refractive index variations) and therefore generate a nearly perfect zero [62, 63, 64, 65, 66]. Unfortunately, the spatial light modulator (SLM) applied showed a wide deviation of the intended phase retardation for some pixels which resulted in an imperfect phase pattern and therefore zero. A solution for this problem could be the correction of the SLM or perfectly fabricated phase masks.

The incomplete depletion of the fluorescence can be solved by using better dyes or environments allowing a stronger depletion of the fluorescence. Incomplete depletion can be caused by light driven reverse intersystem crossing [67, 68, 69, 70, 71]. In reverse intersystem crossing, molecules in the triplet state are excited to higher excited triplet states from where some of them change back to the (fluorescent) singlet state. Reverse intersystem crossing thus prevents a complete triplet population.

### **Photobleaching**

Another limiting factor for GSD microscopy is bleaching of the fluorescent dyes. As already discussed, due to photobleaching issues the donut shaped depletion PSF impeded the application of intensities  $> 80kW/cm^2$  and thus resolutions below  $90nm$  for Atto532 in Vectashield as illustrated in figure 3.28b. Thus, bleaching is one problem that must be addressed for further improvements of GSD microscopy.

Possible improvements could be achieved by using more stable fluorophores, environments featuring less bleaching or also more effective antibleaching reagents. Another approach could be to cool down the sample and thereby to reduce the bleaching of the fluorophores [72].

### **Problems Arising from the Pump-Probe Measurement Mode**

Yet another problem in GSD microscopy is the use of the pump-probe mode. To obtain enough signal the pump-probe cycles usually have to be repeated many times, which can result in strong photobleaching and an elongation of the acquisition time. The probe pulse itself also pumps into the triplet and to minimize this effect one has to minimize the probe integration time for fluorescence acquisition. Especially in solution this is a problem because the short triplet lifetime of several  $\mu s$  makes it necessary to repeat the pump-probe cycle very often on one pixel to obtain enough fluorescence signal.

One could try to circumvent this problem by using a modulated probe beam. In that case the depletion beam is switched on until equilibrium is obtained. Then the probe beam is switched on in addition, its intensity modulated in time for example with a sine wave function. As a consequence the fluorescence excited by the probe beam is also modulated, whereby most of the signal arises from the small sub-diffraction area around the zero of the depletion focus. This modulated signal can be detected with a lock-in amplifier and contains the sub-diffraction information. In this way the image acquisition time could be dramatically reduced because the probe beam would be switched on until enough signal has been obtained. The problem with this method is that the effective signal will be very poor because one has to detect a small modulation of the fluorescence signal on a large constant background signal arising from the unmodulated depletion beam. This will become more and more difficult for effective focal spots of molecular size with only a few or even single molecules left in the detected area.

## Image Acquisition Time

The long pixel dwelltimes of a minimum of  $60\text{ms}$  to several hundred milliseconds slow down the acquisition process. These long pixel dwell times result either from long triplet lifetimes, as in the case of PVA or Vectashield environments, or from a high number of repetitions of the pump-probe cycles required to achieve enough signal as in the case of AZ174 in aqueous solution. One possible way to overcome this problem is to use multiple intensity zeros at a distance larger than the diffraction limit. The image can then be obtained in a widefield setup and a camera by scanning the intensity zeros over the sample. Due to the parallelized scanning the image acquisition will be significantly enhanced [73].

## Negative Imaging

Another possibility to reduce the image acquisition time would be the use of alternative imaging methods also applying optical shelving into a dark state. In the implemented pump-probe approach much signal from the pump pulse is wasted and also the waiting times for triplet relaxation between several pulse sequences on a pixel is not used.

A possible way to overcome this problem is to do so-called "negative" imaging [74], in which one uses additional sub-diffraction information contained in the fluorescence signal generated by the depletion beam. Negative imaging makes use of the nonlinearity between the applied excitation intensity and the emitted fluorescence signal, since the fluorescence signal saturates for high intensities and does not increase anymore for higher intensities due to the depletion of the ground state. This characteristic is shown in figure 3.29 where the excitation intensity dependence of the fluorescence signal (the  $S_1$  population according to equation (2.12)) is calculated for typical dye parameters (same parameters as in section 2.4). If it is possible to pump the dye molecules into the triplet state so that the fluorescence signal saturates, GSD could be applied for negative imaging as well. Also, the fluorescence signal of the depletion, which is not used in positive imaging in GSD microscopy, could be used to extract a negative image as additional information.

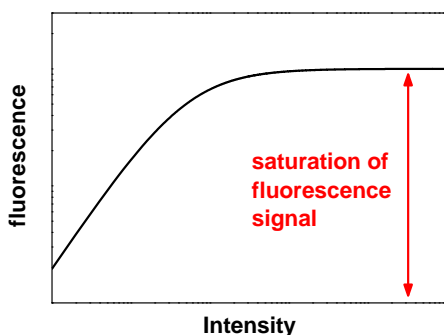


Figure 3.29: Saturation of fluorescence signal ( $S_1$ -population, double logarithmic plot) for typical dye parameters as in section 2.4 according to equation (2.12).

Negative images can be obtained by using a donut shaped beam with an intensity zero in the center which saturates the fluorescence signal everywhere but not in the center of the focus. The non-saturated area in the center (at the zero intensity of the depletion beam) can be decreased to arbitrarily small spots in the same way as it is done with the donut shaped beam in GSD imaging. The only difference is, that in positive imaging one

detects the fluorescence signal from the center of the donut and directly obtains the image. In negative imaging, the signal arises from dye molecules outside the intensity zero. That is why bright areas in positive imaging will be dark in negative imaging. Hence, the recorded scanning image in negative imaging is not the real image and needs to be deconvolved with an exact knowledge of the saturated fluorescence pattern.

As stated before, the necessary precondition for negative imaging is that the fluorescence signal can be saturated. However, such saturation could not be detected for the dyes and experimental conditions used here for GSD microscopy. In all cases, the fluorescence increased further for large excitation intensities as shown in figure 3.30 for EosinY in PVA. A possible reason for this behaviour maybe the previously discussed reverse intersystem crossing [67, 68, 69, 70, 71]. In reverse intersystem crossing molecules in the triplet state are excited to higher excited triplet states from where some of them change back to the (fluorescent) singlet state. The reverse intersystem crossing therefore prohibits the fluorescence signal from saturation, because with rising intensity molecules are transferred back to the (fluorescent) singlet system resulting in a continuous increase of the fluorescence signal with rising power. For intensities up to  $\sim 100 \text{ kW/cm}^2$  the fluorescence signal still increases in figure 3.30 and does not saturate, although the triplet state is already saturated at an intensity of  $\sim I_{sat} = 1 \text{ kW/cm}^2$  (see figure 3.3 for fluorescence depletion curve of EosinY in PVA). That is why negative imaging by optical shelving into the triplet state is not possible, at least for the dyes and experimental conditions tested in this work.

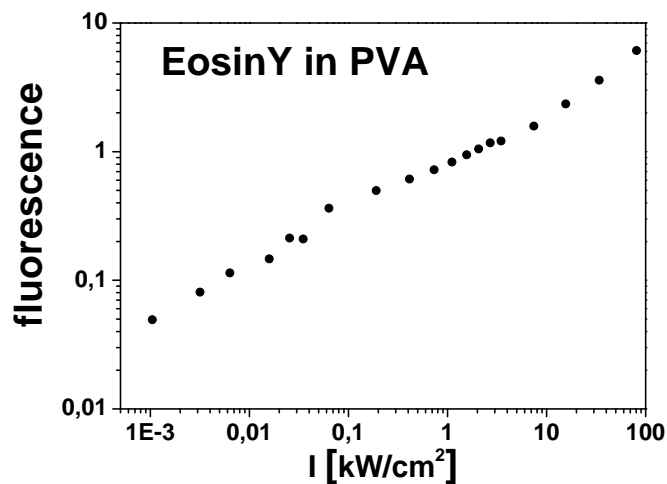


Figure 3.30: Equilibrium fluorescence signal of EosinY in PVA for increasing excitation intensities  $I$

### Sub-diffraction Imaging Exploiting the Temporal Development of the Fluorescence Signal

An alternative theoretically proposed sub-diffraction imaging method makes use of the temporal development of the fluorescence signal in the focus during optical shelving

[75]. Following excitation, the fluorescence signal decreases due to population of the dyes dark (triplet) state as shown for example in figure 3.2b for EosinY in PVA. The effective rate  $k_{eff}^T$  into the triplet state is dependent on the excitation rate  $k_{exc}$  and is given by  $k_{eff}^T = k_{exc} \Phi_{isc}$ , with  $\Phi_{isc}$  the transition probability into the triplet state after excitation. If one pumps the dye molecules with a diffraction-limited focal spot into the triplet state the effective rate  $k_{eff}^T$  into the triplet state spatially differs due to the local intensity distribution of the focal spot (see for example figure 2.8). The fastest reduction of the fluorescence signal due to optical shelving will be in the center of the focal spot with the highest excitation rate  $k_{exc}$  and thus highest effective rate  $k_{eff}^T$ . In contrast, the molecules at the rim are excited by a much smaller excitation rate  $k_{exc}$  and therefore the effective rate into the triplet  $k_{eff}^T$  will be smaller than in the center of the focal spot.

The temporal decay of the fluorescence signal due to optical shelving can be well described by exponential decays. The fastest decay occurs in the center of the focus with the highest intensity and the slowest at the rim of the focus with the smallest intensity. The fluorescence decay is recorded on every scanning step and fitted with a multiexponential decay with the rates fixed to known values from the center and the rim of the focus and values in-between. For example, the amplitude of the shortest decay time should only take values  $> 0$  from a small sub-diffraction region in the center of the focus. By plotting this amplitude one obtains the sub-diffraction image. The advantage of this method is that focal engineering of the focus is obsolete. However, it is very challenging to obtain stable fits to the fluorescence decay signal, since the decay times of the center and the rim of the focus usually do not differ a lot. Also, the intensity distribution of the excitation PSF is continuous and therefore one has to choose several reasonable decay times for the fits. Choosing these decay times carefully necessitates exact knowledge of the decay times in a specific sample. One problem could be that the decay times even differ in the sample at different positions due to small variations of the environment. As well, the fluorescence decay curves need to have a very good signal to noise ratio in order to obtain stable fits.

Summarized, in comparison to the other introduced sub-diffraction approaches using optical shelving into a dark state, GSD based on the RESOLFT concept is still the most favourable one. Following the proposals made for improving the resolution in GSD microscopy promises to enhance the resolution well below the already obtained 50nm.

## 4 Summary and Outlook

The resolution in fluorescence far-field microscopy is limited by diffraction. Although several methods exist for breaking the diffraction barrier, each of them has its own limitations. While STED-microscopy is applicable to nearly every dye it demands for high depletion intensities which could lead to photostress or even photodestruction of the sample. Subdiffraction microscopy techniques employing switchable dyes or proteins make use of low intensities but only have a limiting number of dyes/proteins. Therefore, the GSD concept is introduced, which aims to shelve the fluorescent dyes into a metastable dark state to deplete the fluorescence. Since nearly every dye molecule has a triplet or another dark state, GSD is a general concept. It allows the use of low depletion intensities compared to STED, because of the relative long lifetime of the dark states compared to the fluorescence lifetime. Hence, GSD combines the advantage of low depletion intensities and generality.

In this thesis, the first experimental realization of a GSD microscope was accomplished. Effective optical shelving was found in different fluorophore classes, such as Atto, Rhodamine, Cyanine, Fluoresceine, Bodipy and Alexa dyes, and also in different media, such as Vectashield, PVA, and even aqueous solution. Since the triplet or another dark state is almost inherent to any dye molecule, this generality allows the use of a broad range of dyes, representing a clear advantage of GSD against other sub-diffraction far-field microscopy concepts such as RESOLFT approaches or the recently developed PALM concept [13, 14, 17, 76, 15]. PALM as well needs switchable dyes or proteins whose number is limited.

The relatively long lifetimes of the dark states of several  $\mu s$  to  $ms$  allowed depletion intensities as small as several  $W/cm^2$  to  $kW/cm^2$  compared to  $GW/cm^2$  in STED microscopy. This smaller intensities are favourable because they reduce photostress on the sample and allow the use of less sophisticated laser systems. In principle, a GSD setup only needs a low power cw-laser and fast shutters as a light source.

It was also demonstrated that environmental conditions can be generated to simplify GSD microscopy, for example, by using mounting media increasing the triplet lifetime. Also, the effect of heavy atom doping was examined, giving the opportunity to engineer the intersystem crossing rate and thereby enhance the optical shelving into the dark state.

Sub-diffraction imaging on stained structures, beads and even biological samples was demonstrated with a resolution down to  $50nm$ . It was also proved that GSD imaging in aqueous solution is possible, which is very important for biological applications like live-cell imaging. The main problems in GSD imaging are the imperfect zero of the depletion focus, the incomplete fluorescence depletion, photobleaching and the long image recording times, where probable solutions have been proposed. Possible improvements are, for example, the use of adaptive optics for generating perfect depletion patterns, optimizing

environmental conditions and fluorescent markers for GSD microscopy resulting in a better fluorescence depletion with less bleaching. Further, parallelized imaging can be used for faster image acquisition.

In summary, the possibility of GSD microscopy was proven in this thesis, showing its potential but also its limitations. Intriguingly, the GSD concept implies that optimizing the operational parameters enables a spatial resolution, in principle, down to the molecular scale. Combined with the general presence of the triplet state in all fluorophores, the results underscore the potential to break the diffraction barrier by GSD and promise new exciting insights in biological research.

# A Appendix

## A.1 Pump Probe Simulations

For the simulation of the pump probe experiments, the rate equations of equation (2.10) were applied with the  $S_1 - S_0$  relaxation  $k_{10} = k_Q + k_{fl}$ .

$$\begin{aligned}\dot{S}_0(t) &= -k_{exc}S_0(t) + k_{10}S_1(t) + k_T T_1(t) \\ \dot{S}_1(t) &= k_{exc}S_0(t) - k_{10}S_1(t) - k_{isc}S_1(t) \\ \dot{T}_1(t) &= k_{isc}S_1(t) - k_T T_1(t)\end{aligned}\tag{A.1}$$

This set of differential equations (A.1) can be rewritten with the occupation vector  $\vec{n}$  and a matrix  $\mathbf{A}$ .

$$\dot{\vec{n}}(t) = \mathbf{A} \cdot \vec{n}(t) \quad \text{with } n(t) = \begin{pmatrix} S_0(t) \\ S_1(t) \\ T_1(t) \end{pmatrix} \quad \text{and } A = \begin{pmatrix} -k_{exc} & +k_{10} & +k_T \\ +k_{exc} & -k_{10} - k_{isc} & 0 \\ 0 & k_{isc} & -k_T \end{pmatrix}\tag{A.2}$$

The solution of this set of first order differential equations is given by

$$\dot{\vec{n}}(t) = \vec{n}_0 \cdot e^{\mathbf{A}t} \quad \text{with } \vec{n}_0 = \text{population vector at } t = 0\tag{A.3}$$

Now one can calculate the population numbers on every time point with equation (A.3) when the start vector  $\vec{n}_0$  is known. For numerical calculations of the time development of  $\vec{n}(t)$  after  $k$  ( $k \in \mathbb{N}$ ) constant time steps  $\Delta t$  the population vector  $\vec{n}(k \cdot \Delta t)$  can be calculated iteratively by

$$\vec{n}(k \cdot \Delta t) = \vec{n}((k-1) \cdot \Delta t) \cdot e^{\mathbf{A} \cdot \Delta t}\tag{A.4}$$

The exponential function of the matrix can be simply calculated numerically by using the Matlab built-in *expm* function. To simulate for example the residual fluorescence for the pump probe measurements the first step would be to calculate the population vector at the end of the pump pulse. This population vector, giving the population numbers at the end of the depletion pulse, is the start vector for the calculation of the time development of

the population numbers during the delay time between pump and probe. The resulting population vector is passed as starting condition to the calculation of the time development during the probe pulse. Also, like in the real measurements, the probe development is once calculated with a starting vector  $\vec{n}_0 = (1, 0, 0)$  (that means without pump pulse) to get the reference of the probe fluorescence without preceding pump pulse. For calculation of the residual fluorescence one just has to add up the fluorescence of the two probes pulses (one with and one without preceding pump pulse) for the integration time and calculate their ratio. The residual fluorescence curve was in this way calculated for the pump probe cycle of AZ174 in PBS as shown in figure 3.12.

## A.2 Dye Spectra and Structures

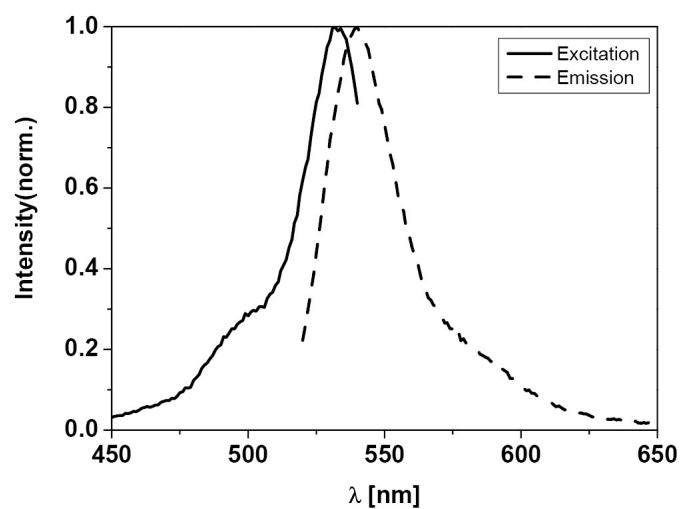


Figure A.1: Excitation and emission spectrum of Eosin Y in a PVA matrix, the excitation maximum is at  $\lambda=532\text{nm}$  and the emission maximum is at  $\lambda=540\text{nm}$

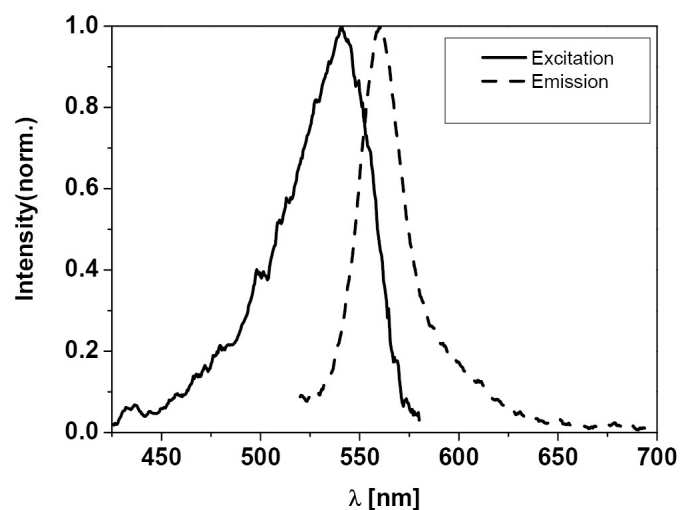


Figure A.2: Excitation and emission spectrum of Orange Beads (540/560) (Molecular Probes, Eugene,OR) in Vectashield, the excitation maximum is at  $\lambda=540\text{nm}$  and the emission maximum is at  $\lambda=560\text{nm}$

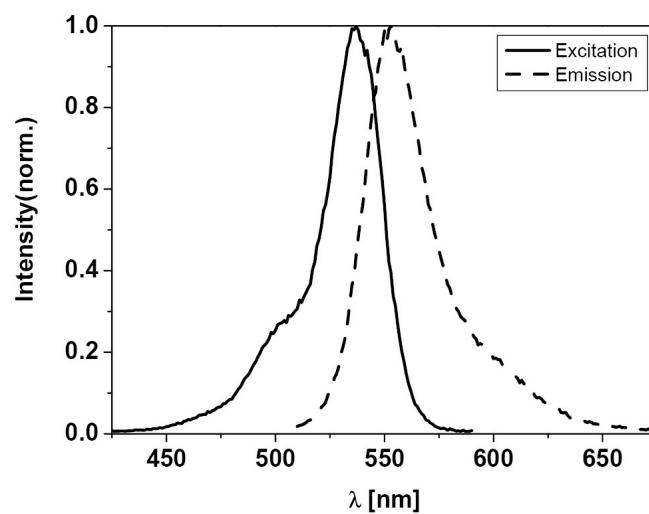


Figure A.3: Excitation and emission spectrum of Atto532 in Vectashield, the excitation maximum is at  $\lambda=535\text{nm}$  and the emission maximum is at  $\lambda=555\text{nm}$

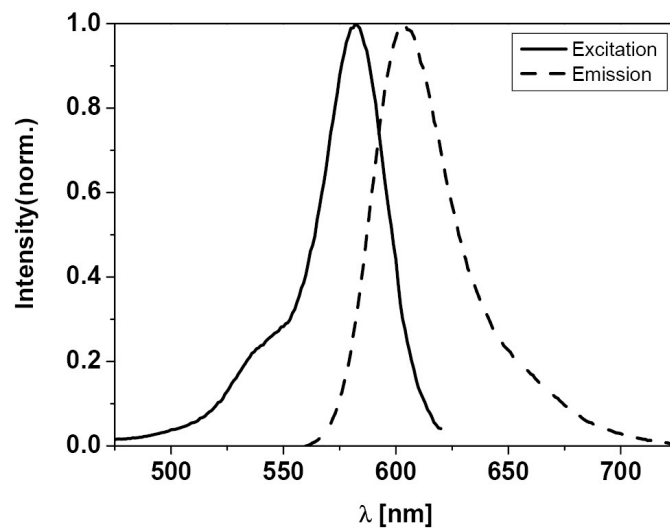


Figure A.4: Excitation and emission spectrum of AZ174 (Thiorhodamine) in PBS (ph=7.5), the excitation maximum is at  $\lambda=580\text{nm}$  and the emission maximum is at  $\lambda=605\text{nm}$

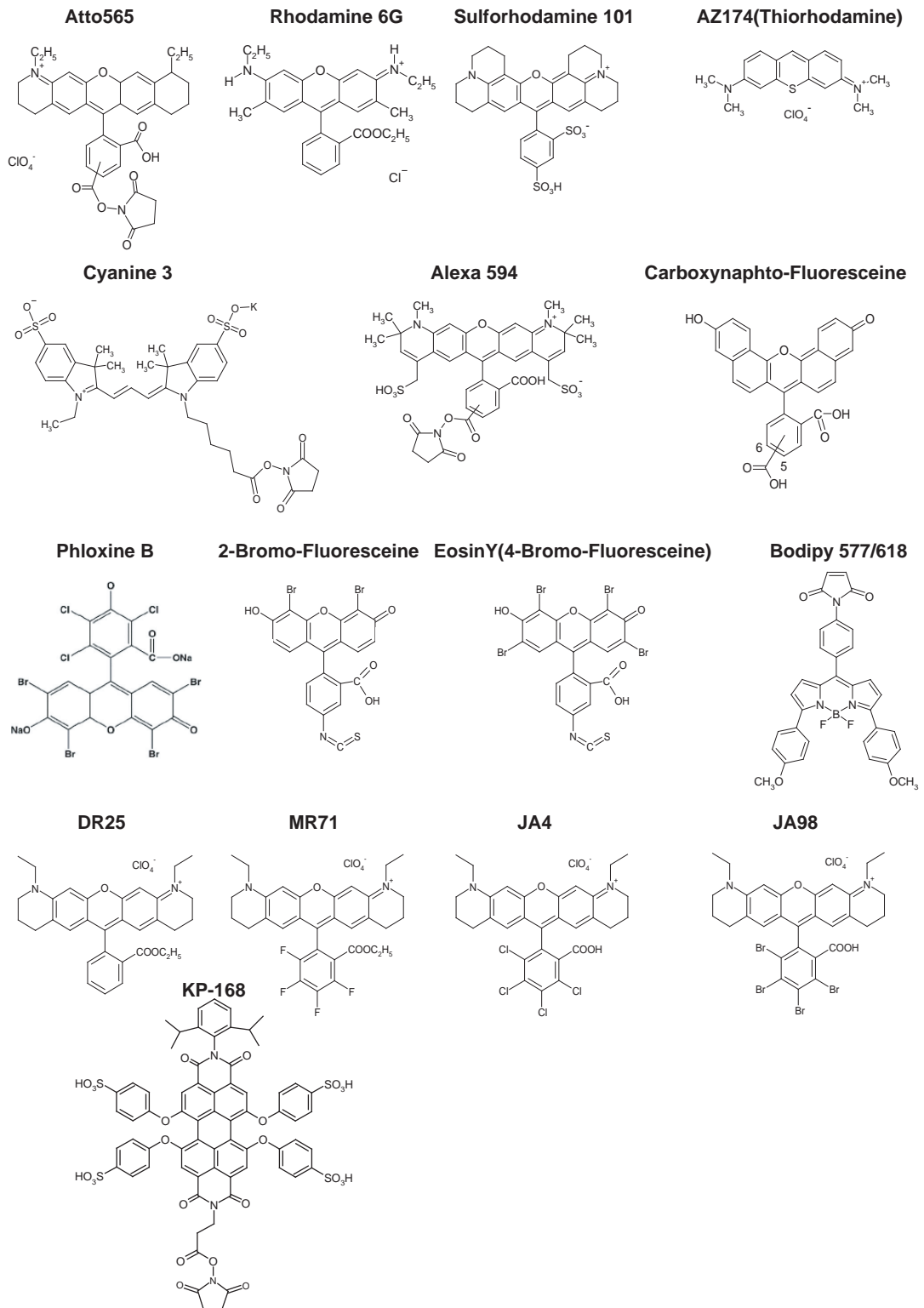


Figure A.5: Structures of dyes applied in GSD

## A.3 Sample Preparation

### Preparation of dye doped polymer films

- Dissolve 4.5 g PVA 4-88 in 30 ml water, stirring and heating to around 50C speeds up dissolution significantly
- dilute PVA-solution with deionized water 1:1
- dissolve as much dye solution in the PVA, so that the concentration is about  $1\mu\text{M}$ , use about 10:1 PVA:dye solution
- spincoat about  $20\mu\text{l}$  of dye doped PVA solution with 5000rpm on a coverslip and mount it on the object slide (seal sample with glue)

The resulting film thickness should be around 200nm which is smaller than the z-dimension of the focal spot so that one can neglect the z extension of the PSF. The film thickness was measured by putting a tesa strip onto the coverslip before spincoating. In that way only half of the coverslip was covered with the PVA film. After this procedure the thickness was measured with a profilometer.

### Preparation of 80nm EosinY beads sample

A pure silica core of size 50 nm was prepared by hydrolysis of tetraethoxysilane in a water-in-oil micro-emulsion [58, 59], and a silica shell of 15 nm thickness grown onto the core (see figure A.6). The dopant Eosin Y was incorporated during this last step, covalently linked to a silica precursor (3-aminopropyl)triethoxysilane), thus leaving the outer rim of Eosin Y staining and an unstained core of 50 nm [60, 61]. The particle sizes of 80nm were confirmed by transmission electron microscopy.

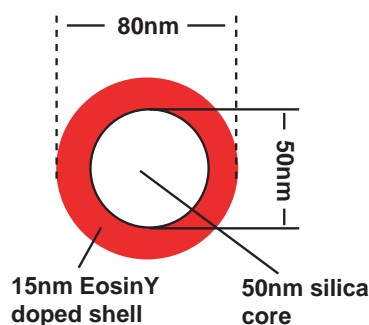


Figure A.6: 80nm EosinY beads. The 50nm diameter silica core is surrounded by a 15nm dye doped EosinY shell.

Preparation of single beads sample:

- dissolve bead solution with ethanol  $\sim$ 1:100 and dry around  $20\mu\text{l}$  on coverslip for 10 minutes

- to prevent oxygen quenching of triplet cover the beads with a PVA layer (spincoat at 5000rpm, same PVA-solution as above)
- mount coverslip on objectslide and seal the sample with glue

If the density of the beads on the coverslip is too low or too high simply vary the concentration of the beads solution.

### **Preparation of 40nm orange beads sample in Vectashield**

- put drop of 100 $\mu$ l Poly-L-Lysine on coverslip for ten minutes, then rinse with deionized water and dry with nitrogen
- dissolve Orange Beads (540/560, Molecular Probes, Eugene,OR) solution with deionized water  $\sim$ 1:500 and dry around 20 $\mu$ l on coverslip for ten minutes, rinse again with deionized water and dry with nitrogen
- mount coverslip on objectslide with a drop of Vectashield and seal the sample with glue

### **Preparation of Biological Samples in VectaShield**

- take coverslips with cells on them out of PBS-solution and dry them for around 5 minutes
- mount coverslip carefully on objectslide (if too much shear force is applied the sample will be damaged!) with a drop of Vectashield and seal the sample with glue

## A.4 List of Scientific Contributions

Parts of this thesis have been published as follows:

S. Bretschneider, C. Eggeling, S. W. Hell. *Breaking the Diffraction Barrier in Fluorescence Microscopy by Optical Shelving*. *Physical Review Letters* **98** (21), 218103.

Talks on national and international conferences:

Focus on Microscopy 2007, Valencia

*Ground-State-Depletion fluorescence microscopy provides subdiffraction resolution through triplet state pumping*

DGAO-Tagung 2006, Weingarten

*Ground-State-Depletion fluorescence microscopy provides subdiffraction resolution through triplet state pumping*

# Bibliography

- [1] A.I. Kirkland and L. Hutchinsons. *Atomic resolution transmission electron microscopy*. In P. W. Hawkes and J. C. H. Spence, editors. Springer, 2007.
- [2] G. Binnig and H. Rohrer. Scanning tunneling microscopy. *Helv. Phys. Acta*, 55:726–735, 1982.
- [3] E. Abbe. Beiträge zur Theorie des Mikroskops and der mikroskopischen Wahrnehmung. *Schultzes Archiv Mikr Anat*, pages 413–468, 1873.
- [4] D.W. Pohl and D. Courjon. Near field optics. *Kluwer Academic*, 1993.
- [5] G. Binnig, CF Quate, and C. Gerber. Atomic Force Microscope. *Physical Review Letters*, 56(9):930–933, 1986.
- [6] W. Baumeister. Electron tomography: towards visualizing the molecular organization of the cytoplasm. *Curr. Opin. Struct. Biol.*, 12:679–684, 2002.
- [7] SW Hell, KI Willig, M. Dyba, S. Jakobs, L. Kastrup, and V. Westphal. Nanoscale Resolution with Focused Light: STED and Other RESOLFT Microscopy Concepts. *Handbook of Biological Confocal Microscopy*, edited by James B. Pawley, pages 571–579, 2006.
- [8] SW Hell, S. Jakobs, and L. Kastrup. Imaging and writing at the nanoscale with focused visible light through saturable optical transitions. *Applied Physics A: Materials Science & Processing*, 77(7):859–860, 2003.
- [9] S.W. Hell. Toward fluorescence nanoscopy. *Nature Biotechnology*, 21(11):1347–1355, 2003.
- [10] S.W. Hell and J. Wichmann. Breaking the diffraction resolution limit by stimulated emission: stimulated-emission-depletion fluorescence microscopy. *Opt. Lett.*, 19(11):780–782, 1994.
- [11] T.A. Klar, S. Jakobs, M. Dyba, A. Egner, and S.W. Hell. Fluorescence microscopy with diffraction resolution barrier broken by stimulated emission. *Proceedings of the National Academy of Sciences*, 97(15):8206–8210, 2000.
- [12] V. Westphal, L. Kastrup, and SW Hell. Lateral resolution of 28 nm ( $\lambda/25$ ) in far-field fluorescence microscopy. *Applied Physics B: Lasers and Optics*, 77(4):377–380, 2003.
- [13] E. Betzig, G.H. Patterson, R. Sougrat, O.W. Lindwasser, S. Olenych, J.S. Bonifacino, M.W. Davidson, J. Lippincott-Schwartz, and H.F. Hess. Imaging Intracellular Fluorescent Proteins at Nanometer Resolution. *Science*, 313(5793):1642, 2006.

- [14] Michael J. Rust, Mark Bates, and Xiaowei Zhuang. Sub-diffraction-limit imaging by stochastic optical reconstruction microscopy (STORM). *Nature Methods*, 3:793–796, 2006.
- [15] J. Fölling, V. Belov, R. Kunetsky, R. Medda, A. Schönle, Bossi. M., and S.W. Hell. Photochromic Rhodamines provide Nanoscopy with Optical Sectioning. *Angew. Chemie*, 119:1–6, 2007.
- [16] M. Hofmann, C. Eggeling, S. Jakobs, and S.W. Hell. Breaking the diffraction barrier in fluorescence microscopy at low light intensities by using reversibly photoswitchable proteins. *Proceedings of the National Academy of Sciences*, 102(49):17565–17569, 2005.
- [17] C. Geisler, A. Schönle, C. Middendorf, H. Bock, C. Eggeling, A. Egner, and S.W. Hell. Resolution of  $\lambda/10$  in fluorescence microscopy using fast single molecule photo-switching. *Appl. Phys. A*, 88:223–226, 2007.
- [18] SW Hell and M. Kroug. Ground-state-depletion fluorescence microscopy: A concept for breaking the diffraction resolution limit. *Applied Physics B: Lasers and Optics*, 60(5):495–497, 1995.
- [19] H. Haken and H.C. Wolf. *Atom- und Quantenphysik*. Springer-Verlag, Berlin, 2003.
- [20] Jiang-Yong Liu, Wen-Hui Fan, Ke-Li Han, Wei-Qiao Deng, Da-Li Xu, and Nan-Quan Lou. Ultrafast vibrational and thermal relaxation of dye molecules in solution. *J. Phys. Chem. A*, 107:10857–10861, 2003.
- [21] M. KASHA. Paths of molecular excitation. *Radiat Res*, 2:243–75, 1960.
- [22] B. Röder. *Einführung in die molekulare Photobiophysik*. B.G. Teubner, Stuttgart, 1999.
- [23] S.P. McGlynn, T. Azumi, and M. Kinoshita. *Molecular Spectroscopy of the Triplet State*. Prentice-Hall, Englewood Cliffs, 1969.
- [24] F.P. Schäfer. *Dye Lasers*. Springer-Verlag, Berlin, 1990.
- [25] M. Born and E. Wolf. *Principles of optics*. Pergamon Press New York, 1980.
- [26] M. Minsky. Microscopy apparatus. *US Patent 3,013,467*, 1961.
- [27] S. Inoue. Foundations of confocal scanned imaging in light microscopy. *Handbook Biological Confocal Microscopy*, pages 1–18, 1995.
- [28] J.H. Denk, J.H. Strickler, and W.W. Webb. Two-photon laser scanning fluorescence microscopy. *Science*, 248:73–76, 1990.
- [29] A. Egner and S.W. Hell. Time multiplexing and parallelization in multifocal multiphoton microscopy. *J. Opt. Soc. Am. A.*, 17:1192–1201, 2000.
- [30] S.W. Hell and E.H.K. Stelzer. Fundamental improvement of resolution with a 4pi-confocal fluorescence microscope using two-photon excitation. *Opt. Commun.*, 93:277–282, 1992.
- [31] H. Gugel, J. Bewersdorf, S. Jakobs, J. Engelhardt, R. Storz, and S.W. Hell. Cooperative 4pi excitation and detection yields 7-fold sharper optical sections in live cell microscopy. *Biophys. J.*, 87:4146–4152, 2004.

- [32] K. König, Y. Tadir, P. Patrizio, M.W. Berns, and B.J. Tromberg. Andrology: Effects of ultraviolet exposure and near infrared laser tweezers on human spermatozoa. *Human Reproduction*, 11(10):2162, 1996.
- [33] J.D. Pedarnig, M. Specht, M. Heckl, and T.W. Hänsch. Scanning plasmon near-field microscope. *Proc. NFO1 NATO ASI Series E242*, eds. DW: Pohl and D. Coujon, pages 273–280, 1993.
- [34] V. Westphal and S.W. Hell. Nanoscale Resolution in the Focal Plane of an Optical Microscope. *Physical Review Letters*, 94(14):143903, 2005.
- [35] G. Donnert, J. Keller, R. Medda, M.A. Andrei, S.O. Rizzoli, R. Luhrmann, R. Jahn, C. Eggeling, and S.W. Hell. Macromolecular-scale resolution in biological fluorescence microscopy. *Proceedings of the National Academy of Sciences*, 103(31):11440, 2006.
- [36] M. Dyba and S.W. Hell. Focal spots of size  $1/23$  open up far-field fluorescence microscopy at 33 nm axial resolution. *Physical Review Letters*, 88:163901, 2002.
- [37] KI Willig, J. Keller, M. Bossi, and SW Hell. STED microscopy resolves nanoparticle assemblies. *New Journal of Physics*, 8(6):106, 2006.
- [38] D. Fitzner, A. Schneider, A. Kippert, W. Mbius, K. I. Willig, S. W. Hell, G. Bunt, K. Gaus, and M. Simons. Myelin basic protein-dependent plasma membrane reorganization in the formation of myelin. *EMBO J.*, 25(5037-5048), 2006.
- [39] R. Kellner, J. Baier, K. I. Willig, S. W. Hell, and F. J. Barrantes. Nanoscale organization of nicotinic acetylcholine receptors revealed by STED microscopy. *Neuroscience*, 144(1):135–143, 2007.
- [40] R. J. Kittel, C. Wichmann, T. M. Rasse, W. Fouquet, M. Schmidt, A. Schmid, D. A. Wagh, C. Pawlu, R. Kellner, K. I. Willig, S. W. Hell, E. Buchner, M. Heckmann, and S. J. Sigrist. Bruchpilot Promotes Active Zone Assembly, Ca<sup>2+</sup>-Channel Clustering, and Vesicle Release. *Science*, 312:1051–1054, 2006.
- [41] M. Bossi, J. Filling, M. Dyba, V. Westphal, and S. W. Hell. Breaking the diffraction resolution barrier in far-field microscopy by molecular optical bistability. *New J. Phys.*, 8:275, 2006.
- [42] R. Heintzmann, T.M. Jovin, and C. Cremer. Saturated patterned excitation microscopy—a concept for optical resolution improvement. *Journal of the Optical Society of America A*, 19(8):1599–1609, 2002.
- [43] R. Heintzmann. Saturated patterned excitation microscopy with two-dimensional excitation patterns. *Micron*, 34(6-7):283–91, 2003.
- [44] J. Widengren, A. Chmyrov, C. Eggeling, P.-A. Löfdahl, and C. A. M. Seidel. Strategies to Improve Photostabilities in Ultrasensitive Fluorescence Spectroscopy. *J. Phys. Chem. A*, 111:429–444, 2007.
- [45] R. Zondervan, F. Kulzer, M.A. Kolchenko, and M. Orrit. Photobleaching of Rhodamine 6G in Poly (vinyl alcohol) at the Ensemble and Single-Molecule Levels. *J. Phys. Chem. A*, 108(10):1657–1665, 2004.

- [46] C. Eggeling, A. Volkmer, and C.A.M. Seidel. Molecular Photobleaching kinetics of Rhodamine 6G by one- and two-photon induced confocal fluorescence microscopy. *Chem.Phys.Chem.*, 6(791-804), 2005.
- [47] T.A. Klar, E. Engel, and S.W. Hell. Breaking Abbe's diffraction resolution limit in fluorescence microscopy with stimulated emission depletion beams of various shapes. *Phys. Rev. E*, 64:066613, 1–9, 2001.
- [48] J. Keller, A. Schönle, and S.W. Hell. Efficient fluorescence inhibition patterns for RESOLFT microscopy. *Optics Express*, 15(6):3361–3371, 2007.
- [49] Y. Igasaki, F. Li, N. Yoshida, H. Toyoda, T. Inoue, N. Mukohzaka, Y. Kobayashi, and T. Hara. High efficiency electrically-addressable phase-only spatial light modulator. *Optical Review*, 6(4):339–344, 1999.
- [50] M.P. Lettinga, H. Zuilhof, and A.M.J. Zandvoort. Phosphorescence and fluorescence characterization of fluorescein derivatives immobilized in various polymer matrices. *Phys. Chem. Chem. Phys.*, 2:3697–3707, 2000.
- [51] A. Longin, C. Souchier, M. French, and P. Bryon. Comparison of Anti-fading Agents Used in Fluorescence Microscopy: Image Analysis and Laser Confocal Microscopy Study. *The Journal of Histochemistry and Cytochemistry*, 41:1833–1840, 1993.
- [52] P.W. Atkins. *Physikalische Chemie*. Wiley VCH, Weinheim, 1996.
- [53] E.L. Elson and D. Magde. Fluorescence correlation spectroscopy i. conceptual basis and theory. *Biopolymers*, 13:1–27, 1974.
- [54] D. Magde, E. L. Elson, and W. W. Webb. Thermodynamic fluctuations in a reacting system - measurement by fluorescence correlation spectroscopy. *Physical Review Letters*, 29(11):705–708, 1972.
- [55] D. Magde, E.L. Elson, and W.W. Webb. Fluorescence correlation spectroscopy ii. an experimental realization. *Biopolymers*, 13:29–61, 1974.
- [56] J. Widengren, U. Mets, and R. Rigler. Fluorescence correlation spectroscopy of triplet states in solution: a theoretical and experimental study. *The Journal of Physical Chemistry*, 99(36):13368–13379, 1995.
- [57] R. Zondervan, F. Kulzer, H. van der Meer, J.A.J.M. Disselhorst, and M. Orrit. Laser-Driven Microsecond Temperature Cycles Analyzed by Fluorescence Polarization Microscopy. *Biophysical Journal*, 90(8):2958–2969, 2006.
- [58] K. Osseo-Asare and F. J. Arriagada. Preparation of SiO<sub>2</sub> nanoparticles in a non-ionic reverse micellar system. *Coll. Surf.*, 50:321–339, 1990.
- [59] F. J. Arriagada and K. Osseo-Asare. Synthesis of nanosize silica in a nonionic water-in-oil microemulsion: Effects of the water/surfactant molar ratio and ammonia concentration. *Journal of Colloid and Interface Science*, 211(2):210–220, 1999.
- [60] G. H. Bogush, M. A. Tracy, and C. F. Zukoski. Preparation of Monodisperse Silica Particles - Control of Size and Mass Fraction. *Journal of Non-Crystalline Solids*, 104(1):95–106, 1988. Times Cited: 278 Article English Cited References Count: 18 P6711.

- [61] A. Van Blaaderen and A. Vrij. Synthesis and characterization of colloidal dispersions of fluorescent, monodisperse silica spheres. *Langmuir*, 8(12):2921–2931, 1992.
- [62] M.J. Booth, M.A.A. Neil, and T. Wilson. Aberration correction for confocal imaging in refractive-index-mismatched media. *J. Microsc.*, 192(2):90–98, 1998.
- [63] O. Albert, L. Sherman, G. Mourou, and T.B. Norris. Smart microscope: an adaptive optics learning system for aberration correction in multiphoton confocal microscopy. *Opt. Lett.*, 25(1):52–54, 2000.
- [64] M.J. Booth, M.A.A. Neil, R. Juskaitis, and T. Wilson. Adaptive aberration correction in a confocal microscope. *Proc. Natl. Acad. Sci. USA*, 99(9):5788–5792, 2002.
- [65] M.J. Booth and T. Wilson. Strategies for the compensation of specimen-induced spherical aberration in confocal microscopy of skin. *J. Microsc.*, 200(1):68–74, 2000.
- [66] M.J. Booth and T. Wilson. Refractive-index-mismatch induced aberrations in single-photon and two-photon microscopy and the use of aberration correction. *J. Biomed. Opt.*, 6(3):266–272, 2001.
- [67] S. Reindl and A. Penzkofer. Higher excited-state triplet-singlet intersystem crossing of some organic dyes. *Chemical Physics*, 211(1):431–439, 1996.
- [68] H. Gratz and A. Penzkofer. Saturable absorption dynamics in the triplet system and triplet excitation induced singlet fluorescence of some organic molecules. *Chemical Physics*, 263(2):471–490, 2001.
- [69] J.M. Larkin, W.R. Donaldson, R.S. Knox, and T.H. Foster. Reverse Intersystem Crossing in Rose Bengal. II. Fluence Dependence of Fluorescence Following 532 nm Laser Excitation. *Photochemistry and Photobiology*, 75(3):221–228, 2002.
- [70] C.R. Lambert, I.E. Kochevar, and W. Redmond. Differential Reactivity of Upper Triplet States Produces Wavelength-Dependent Two-Photon Photosensitization Using Rose Bengal. *J. Phys. Chem. B*, 103:094105, 1999.
- [71] R.W. Redmond, I.E. Kochevar, M. Krieg, G. Smith, and W.G. McGimpsey. Excited state relaxation in cyanine dyes: a remarkably efficient reverse intersystem crossing from upper triplet levels. *J. Phys. Chem. A*, 101:2773–2777, 1997.
- [72] M. Schwentker. *Parallelized Ground State Depletion*. PhD Thesis, Heidelberg, 2007.
- [73] M.A. Schwentker, H. Bock, M. Hofmann, S. Jakobs, J. Bewersdorf, C. Eggeling, and S.W. Hell. Wide-field sub-diffraction RESOLFT microscopy using fluorescent protein photoswitching. *Micr. Res. Tech.*, 70(3):269–280, 2007.
- [74] M.G.L. Gustafsson. Nonlinear structured-illumination microscopy: Wide-field fluorescence imaging with theoretically unlimited resolution. *Proceedings of the National Academy of Sciences*, 102(37):13081–13086, 2005.
- [75] J. Enderlein. Breaking the diffraction limit with dynamic saturation optical microscopy. *Appl. Phys. Lett.*, 87:3737–3741, 1999.

- [76] H. Bock, C. Geisler, C. Wurm, S. Jakobs, A. Schönle, A. Egner, and C. Hell, S.W. and Eggeling. Two-color far-field fluorescence nanoscopy based on photo-switching emitters. *Appl. Phys. B*, 88:161–165, 2007.



# Acknowledgements

This thesis was carried out in the department of NanoBiophotonics at the Max-Planck-Institute for Biophysical Chemistry in Göttingen. I would like to thank all people who have contributed to the success of this thesis.

First of all, I would like to thank Prof. Dr. Stefan W. Hell for not only proposing the interesting as well as challenging project of GSD microscopy, but also providing an exceptionally well-equipped work place and a fantastic scientific environment. His continuous input of new ideas and enthusiastic support has significantly contributed to the success of this work.

Prof. Dr. R.G. Ulbrich for being the second referee of this thesis. I would also like to thank him for his continuous interest and support for my work which already started during my diploma thesis.

Dr. Christian Eggeling for his support, fruitful discussions, his expertise and being more than only a supervisor. Without his assistance the results of this thesis would not have been possible.

I also thank the following former and present members of the department of NanoBiophotonics:

Dr. Andreas Schönle for valuable discussions and for help with his sophisticated *Imspector* software.

Jaydev Jethwa and Harald Meyer for great technical assistance. I would also like to thank Jaydev Jethwa for proofreading the manuscript, even on his holidays!

Dr. Stefan Jakobs and Sylvia Löbermann for preparing a numerous samples.

Hannes Bock, Benjamin Harke and Christian Ringemann not only for valuable discussions, but also for providing an enjoyable life outside of science.

Dr. Jan Keller for valuable discussion, proofreading and various calculation tools.

Dr. Scott Irvine for proofreading the manuscript and many fruitful discussions not necessarily related to physics.

Dr. Mariano Bossi for preparing the important and versatile fluorescent beads.

Dr. Juha Toivonen for being an enjoyable partner in the lab for half a year.

Dr. Lars Kastrop, Dr. Volker Westphal, Michael Hofmann, Dr. Alexander Egner, Claas von Middendorff, Dr. Michael Hilbert, Dr. Robert Kellner, Arnold Giske, Dr. Miriam Schwentker and Dr. Katrin Willig for valuable discussions.

I would also like to thank all the other members of the department for the creative and joyful environment.

This work would not have been possible without the great mechanical, electrical and optical workshop.

I would also like to thank all my friends providing an enjoyable life outside of science.

I especially thank my girl friend Katrin for always supporting and encouraging me. Further, I also thank my parents and my whole family for always supporting me. Göttingen, 2007